COMPUTATIONAL INVESTIGATION OF ROTORCRAFT AVIONICS BAY COOLING SYSTEM

A THESIS SUBMITTED TO
THE GRADUATE SCHOOL OF NATURAL AND APPLIED SCIENCES
OF
MIDDLE EAST TECHNICAL UNIVERSITY

BY

ALTUĞ AKIN

IN PARTIAL FULFILLMENT OF THE REQUIREMENTS
FOR
THE DEGREE OF MASTER OF SCIENCE
IN
AEROSPACE ENGINEERING

AUGUST 2019

Approval of the thesis:

COMPUTATIONAL INVESTIGATION OF ROTORCRAFT AVIONICS BAY COOLING SYSTEM

submitted by **ALTUĞ AKIN** in partial fulfillment of the requirements for the degree of **Master of Science in Aerospace Engineering Department, Middle East Technical University** by,

Prof. Dr. Halil Kalıpçılar
Dean, Graduate School of **Natural and Applied Sciences**

Prof. Dr. İsmail Hakkı Tuncer
Head of Department, **Aerospace Engineering**

Assist. Prof. Dr. Harika Senem Kahveci
Supervisor, **Aerospace Engineering, METU**

Examining Committee Members:

Prof. Dr. İsmail Hakkı Tuncer
Aerospace Engineering, METU

Assist. Prof. Dr. Harika Senem Kahveci
Aerospace Engineering, METU

Assoc. Prof. Dr. Nilay Sezer Uzol
Aerospace Engineering, METU

Assoc. Prof. Dr. Mehmet Metin Yavuz
Mechanical Engineering, METU

Assoc. Prof. Dr. Murat Kadri Aktaş
Mechanical Engineering, TOBB ETU

Date: 28.08.2019

I hereby declare that all information in this document has been obtained and presented in accordance with academic rules and ethical conduct. I also declare that, as required by these rules and conduct, I have fully cited and referenced all material and results that are not original to this work.

Name, Surname: Altuğ Akın

Signature:

ABSTRACT

COMPUTATIONAL INVESTIGATION OF ROTORCRAFT AVIONICS BAY COOLING SYSTEM

Akın, Altuğ
Master of Science, Aerospace Engineering
Supervisor: Assist. Prof. Dr. Harika Senem Kahveci

August 2019, 148 pages

Computational investigation of a rotorcraft avionics bay cooling system is performed. Within the introduced system, the ambient air is supplied to the avionics-bay by a fan and exhausted back into the ambient after cooling the equipment inside. Depending on the fan and exhaust locations, hot zones may form around some of the equipment. The fan must provide a sufficiently high mass flow rate to keep the temperatures of the avionics equipment below the limits, while avoiding excessive amount of cooling to reduce power consumption. In this study, the effects of the fan and exhaust locations on the required mass flow rate are investigated. Prediction functions with Gaussian Process Regression and Artificial Neural Network methods are built to predict avionics surface temperatures using the results from a series of Computational Fluid Dynamics (CFD) analyses. The first method is selected over the latter as it yields more accurate results. The selected prediction function is used in conjunction with an optimization algorithm to determine the optimum fan and exhaust locations that minimize the required mass flow rate. It is found out that the required mass flow rate significantly depends on the fan location, while, the exhaust location has a relatively lessened effect. The required mass flow rate could be reduced to around half of its value with an even more significant reduction in power consumption. Additionally, the CFD analysis for the optimum fan and exhaust locations are repeated with different turbulence models to evaluate the effect of the selected model on the results.

Keywords: Avionics Cooling, Design of Experiment, Computational Fluid Dynamics, Optimization, Gaussian Process Regression, Artificial Neural Networks, Turbulence Model

ÖZ

DÖNER KANATLI BİR UÇAĞIN AVİYONİK SOĞUTMA SİSTEMİNİN HESAPLAMALI OLARAK İNCELENMESİ

Akın, Altuğ
Yüksek Lisans, Havacılık ve Uzay Mühendisliği
Tez Danışmanı: Dr. Öğr. Üyesi Harika Senem Kahveci

Ağustos 2019, 148 sayfa

Döner kanatlı bir uçağın aviyonik bölme soğutma sistemi hesaplamalı olarak incelenmiştir. Bahsi geçen sistemde, dış ortam havası fan tarafından aviyonik bölmeye taşınır ve bölmedeki ekipmanlar soğutulduktan sonra hava dış ortama egzoz üzerinden tahliye edilir. Fan ve egzoz yerlerine göre, bölme içerisinde bazı ekipmanların çevresinde sıcak bölgeler oluşabilmektedir. Fanın hava debisi, aviyonik ekipman sıcaklıklarının limitleri geçmemesi için yeterince yüksek olmalı, diğer yandan gerekenden daha yüksek bir hava debisinden, sistemin güç tüketimini arttırmamak için kaçınılmalıdır. Bu çalışmada, fan ve egzoz yerlerinin ihtiyaç duyulan debi miktarına etkisi incelenmiştir. Hesaplamalı Akışkanlar Dinamiği (HAD) analizleri ile elde edilen sonuçlar kullanılarak, aviyonik yüzey sıcaklıklarını tahmin etmek üzere Gauss Süreç Regresyonu ve Yapay Sinir Ağı metotları kullanılarak tahmin fonksiyonları oluşturulmuştur. İlk metot, ikincisine göre daha doğru sonuçlar verdiği için seçilmiştir. Seçilen fonksiyon bir optimizasyon algoritması ile beraber kullanılarak, ihtiyaç duyulan debiyi en aza indiren uygun fan ve egzoz yerleri belirlenmiştir. Çalışma sonucunda, fan yerinin ihtiyaç duyulan debi miktarı üzerinde önemli bir etkiye sahip olduğu, egzoz yerinin etkisinin ise nispeten daha az olduğu bulunmuştur. İhtiyaç duyulan debi miktarı yarı yarıya düşürülebilirken, güç tüketimindeki düşüşün daha da fazla olduğu görülmüştür. Ek olarak, en uygun fan ve egzoz yerleri için yapılan HAD analizleri, seçilen modelin sonuçlara olan etkisini değerlendirmek için farklı türbülans modelleri ile tekrarlanmıştır.

Anahtar Kelimeler: Aviyonik Soğutma, Deney Tasarımı, Hesaplamalı Akışkanlar Dinamiği, Optimizasyon, Gauss Süreç Regresyonu, Yapay Sinir Ağları, Türbülans Modeli

To my family

ACKNOWLEDGEMENTS

I would like to express my appreciation and gratitude to my advisor Assist. Prof. Dr. Harika Senem Kahveci for her supervision during my research.

I would like to thank to the members of dissertation committee for their valuable feedback; Prof. Dr. İsmail Hakkı Tuncer, Assoc. Prof. Dr. Nilay Sezer Uzol, Assoc. Prof. Dr. Mehmet Metin Yavuz, Assoc. Prof. Dr. Murat Kadri Aktaş and Assist. Prof. Dr. Harika Senem Kahveci.

I owe my deepest gratitude to my father Kılıçarslan Akın and my mother Raziye Akın for their endless love, support and guidance throughout my whole life. I am grateful to my sister Tuğçe Akın for encouraging me and keeping me motivated through this research and in my life general, even while living in another country.

I would like to express my appreciation to my friends and colleagues for their support and patience.

TABLE OF CONTENTS

CHAPTER

LIST OF TABLES

LIST OF FIGURES

LIST OF ABBREVIATIONS

ANN	Artificial Neural Network
ARD	Automatic Relevance Determination
CFD	Computational Fluid Dynamics
DOE	Design of Experiment
DP	Design Points
GCI	Grid Convergence Index
GP	Gaussian Process
GPR	Gaussian Process Regression
GR	Grashof Number
MSE	Mean Squared Error
PR	Prandtl Number
RNG	Renormalization Group
RS	Response Surface
SST	Shear-Stress Transport
T.I.	Turbulence Intensity

LIST OF SYMBOLS

$A_{avionics}$	Summation of Side Wall Areas and Top Wall Area of Avionics (m^2)
a	Speed of Sound, (m/s)
a_{exp}	Coefficients of Expansion
α	Absorptivity
α_{ε}	Inverse Effective Prandtl Number for Turbulence Dissipation Rate
A_{floor}	Area of Floor, (m^2)
α_k	Inverse Effective Prandtl Number for Turbulence Kinetic Energy
A_{skin}	Area of Skin, (m^2)
A_{top}	Area of Avionics Top Wall, (m^2)
$A_{vertical}$	Area of Avionics Side Walls, (m^2)
b	Bias
β	Thermal Expansion Coefficient, (K^{-1})
c_p	Specific Heat, (J/kg-K)
d	Diameter, (m)
D	Dimensionality
D_{heated}	Diameter of the Heated Cylinder, (m)
ΔP	Static Pressure Rise across the Fan, (Pa)
D_{ω}	Cross-diffusion term
E	Total Energy, (J/kg)
η	Efficiency of the Fan
e	Base of Expansion
ε	Turbulent Dissipation Rate, (m^2/s^3)
$\varepsilon_{avionics}$	Emissivity of Surface of Avionics
$E_{emission}$	Radiation Emitted by the Inner Surface of Skin & Floor, (W)
$\varepsilon_{inner\ wall}$	Emissivity of Inner Surface of Skin & Floor
$E_{irradiation}$	Radiation Incident on the Inner Surface of Skin & Floor, (W)
Γ_k	Effective Diffusivity of Turbulence Kinetic Energy
Γ_{ω}	Effective Diffusivity of Specific Turbulence Dissipation Rate
f	View Factor

F_S	Factor of Safety
G_b	Generation of Turbulence due to Buoyancy
G_k	Generation of Turbulence due to Mean Velocity Gradients
G_ω	Production of Specific Turbulence Dissipation Rate
$h_{average}$	Average Convective Heat Transfer Coefficient from Side Walls & Top Wall of Equipment (W/m^2-K)
h_{inside}	Convective Heat Transfer Coefficient at Inner Surface of Skin and Floor, (W/m^2-K)
$h_{outside}$	Convective Heat Transfer Coefficient at Outer Surface of Skin and Floor, (W/m^2-K)
h_{top}	Convective Heat Transfer Coefficient from Top Wall (W/m^2-K)
$h_{vertical}$	Convective Heat Transfer Coefficient from Side Walls (W/m^2-K)
$k(\mathbf{x},\mathbf{x}')$	Variance-Covariance Matrix
k	Thermal Conductivity, (W/m-K)
ξ	Relative Error between the Fine and Medium Meshes
k_{eff}	Effective Thermal Conductivity, (W/m-K)
k_{turb}	Turbulence Kinetic Energy, (m^2/s^2)
L	Characteristic Length of Side Walls and Top Wall of Avionics (m)
l	Thickness of Skin and Floor, (m)
$\dot{m}$	Mass Flow Rate, (kg/s)
$m(\mathbf{x})$	Mean Value Of the Random Avionics Average Surface Temperature Variables
μ	Dynamic Viscosity, ($N\text{-}s/m^2$)
μ_t	Turbulence Viscosity, ($N\text{-}s/m^2$)
n	Number of Avionics
Nu	Nusselt Number
P	Order of Accuracy
Pr_t	Turbulence Prandtl Number
$q_{convection}$	Convective Heat Flux, (W/m^2)
$Q_{convection}$	Convective Heat Transfer, (W)
$Q_{heat\ load}$	Heat Load of the Avionics Equipment, (W)
$Q_{outside}$	Heat Transferred to The Outside Air through Skin and Floor, (W)
$Q_{radiation}$	Net Radiative Heat Transfer, (W)

R	Refinement Factor
r	Size of the Data Set
ρ	Density, (kg/m^3)
S	Modulus of the Mean Rate-of-Strain Tensor
δ	Kronecker-Delta Function
σ	Stefan Boltzmann Constant, (W/m^2-K^4)
σ_l, σ_m	Characteristics Length Scales
S_ε	Source Terms for Turbulence Dissipation Rate
σ_ε	Prandtl Number for Turbulence Dissipation Rate
σ_f	Signal Standard Deviation
S_k	Source Terms for Turbulence Kinetic Energy
σ_k	Prandtl Number for Turbulence Kinetic Energy
θ	Non-Dimensional Temperature
t	Index of the Design Point
ϕ	Number Obtained by Halton Sequence Procedure
$T_{av\text{-}ANN}$	Average Avionics Surface Temperature Predicted by the ANN, (K)
$T_{av\text{-}CFD}$	Average Avionics Surface Temperature Calculated by the CFD, (K)
$T_{av\text{-}PRE}$	Average Avionics Surface Temperatures Obtained by Prediction Function, (K)
$T_{avionics}$	Average Surface Temperature of Avionics, (K)
$T_{exhaust}$	Air Temperature at Exhaust, (K)
T_{fan}	Temperature of Air Supplied by Fan, (K)
$T_{inner\ wall}$	Average Temperature of Inner Surfaces of Skin and Floor, (K)
T_{inside}	Average Air Temperature inside the Bay, (K)
T_{nozzle}	Air Temperature at Nozzle Exit, (K)
$T_{outside}$	Outside Air Temperature, (K)
T_{wall}	Local Wall Temperature Along the Heated Cylinder, (K)
$\tilde{u}_i, \tilde{u}_j, \tilde{u}_k$	Mean Velocity Components, (m/s)
u_i'', u_j'', u_k'	Fluctuating Velocity Components
u_i, u_j, u_k	Velocity Components, (m/s)
U	Overall Heat Transfer Coefficient, (W/m^2-K)

V^*	Non-Dimensional Velocity
V_{inside}	Average Air Velocity Magnitude inside the Bay, (m/s)
$\dot{W}$	Power Consumption of Fan, (W)
w	Weights
ω	Specific Turbulence Dissipation Rate, (s^{-1})
$\boldsymbol{x}$	Input Variables Vector
Y_k	Dissipation of Turbulence Kinetic Energy due to Turbulence
Y_M	Contribution of the Fluctuating Dilatation Incompressible Turbulence
Y_ω	Dissipation of Specific Turbulence Dissipation Rate due to Turbulence

CHAPTER 1

INTRODUCTION

1.1. Avionics Cooling

The electronics equipment used in aviation industry, known as avionics, is composed of sub components such as printed circuit boards that generate heat during operation. Maintaining the operational temperature limits of these sub components is a significant factor in achieving a reliable and safe operation of the equipment [1]. As the aircraft become more and more dependent on avionics [2], so does providing appropriate thermal environment to avionics equipment inside the bay. Although the avionics manufacturer provides means for removing heat from sub components inside the avionics equipment, it is the duty of the airframe manufacturer to ensure an appropriate thermal environment around this avionics equipment. Several of them are installed together in a close-packed fashion in the avionics bay, requiring an effective removal method of the total heat load produced from the bay. This task becomes even more challenging as the use of composite structures in the aviation industry increases [3]. Since composites have poor thermal conductivity, they act like thermal insulators, resulting in a significant decrease in the heat transferred from the inside of the bay to the outside.

1.2. Literature Survey

A typical avionics cooling system consists of a fan and an opening. The fan provides air circulation inside the bay. The heat generated by the avionics equipment is transferred to this air. Than the air is exhausted to the ambient. The system weight and the amount of power consumption are proportional to the air mass flow rate supplied by the fan, therefore the use of excessive mass flow rate adversely affects the rotorcraft performance. In order to ensure an efficient cooling of the avionics bay, the designer has the options of strategically-locating the avionic equipment and managing the flow field inside the bay. The flow management can be performed in several ways, such as changing the locations of the fan and the exhaust, using the fan in suction or blowing configurations, adding vane-like structures inside the bay to direct the air flow in the desired way, and adding a ducting system to supply or draw air from specific points of bay.

Butler, et al [3] carried out experimental and computational analyses for a crown compartment of an aircraft including two avionics equipment. The crown compartment is the region of the aircraft between the roof of the cabin and the upper fuselage skin. In the study, there was one air inlet to the crown compartment from the cabin and two outlets on the sides of the compartment. They compared the results from five different configurations of avionics equipment locations. Butler, et al [4] also conducted a research to optimize the locations of avionics equipment in the crown compartment mentioned above. Similarly two avionics equipment were installed inside the compartment. Design of experiment (DOE) method was used to determine the design points and CFD analyses were carried out at these points. Using these results, mathematical models were built to calculate the temperatures around the equipment by a regression method, and the best locations for the equipment were determined through a visual observation of the contour plots.

There have been other studies focusing on aircraft thermal analysis with the goal of modeling complex systems with higher accuracy yet reducing computational requirements while doing so. Stafford, et al [5] used compact thermal fluid models to build a reduced order model of avionics equipment. CFD analyses were utilized to determine unknown coefficients of the compact thermal fluid model. Results could be obtained much faster with this reduced order model compared to CFD analyses. It was stated that such compact thermal fluid models could be utilized for electronics cooling problems with different length scales. Domains with lower length scales, like the internal region of equipment located at an avionics bay, could be represented by compact thermal fluid models. These models could be solved in conjunction with CFD analyses that are used to obtain flow parameters at the domains with higher length scales, like the avionics bay. They also performed such an integration of the developed model into their CFD analysis. Throughout the solution process, the boundary conditions were transferred between the CFD analysis and the compact thermal fluid model. Baalbergen, et al [6] used artificial neural networks to develop a transient thermal model for avionics equipment and a wing spar. Since developing a transient model increased the amount of input and output data significantly, the proper orthogonal decomposition technique was utilized to decrease the dimensionality of the data. Following this, an artificial neural network was trained to predict twenty-one nodal temperature values inside the avionics equipment and another artificial neural network was trained to predict temperature values at 2700 nodes along the wing spar.

Jackson, et al [7] used an optimization method rather than a visual inspection to determine the optimum installation locations of the equipment on four side-panels of a satellite. Annealing method was used as an optimization algorithm. The constraints used for the optimization distributed the total heat load of the equipment uniformly among the four side-panels, minimizing the required length of the electrical cable and providing a balanced center of gravity. Hengeveld, et al [8] also worked on a method for the placement of electronics equipment on a satellite panel. Radiative heat transfer was neglected in their case. Therefore, the only mean for equipment cooling was the conduction to the satellite panel. Due to this simpler heat transfer mechanism, a mathematical model was built on an idea that the equipment with high heat loads required a greater distance from the nearby equipment, compared to the equipment with lower heat loads. Another optimization method known as Genetic Algorithm was used with this model to find the best locations for the avionics equipment installation.

Dancer, et al [9] investigated a problem where a certain number of heat generating equipment was installed in one single row. This time, the equipment was cooled by forced convection. The aim of the study was to find the best order of the equipment along the row such that the summation of the failure rates of the equipment was the smallest. The failure rate was defined as a function of the equipment junction temperature, which was the temperature value at the location between the bottom of the equipment and the structure that the equipment was installed on.

The mentioned research above focused on the avionics equipment locations in order to increase the efficiency of the avionics cooling system. Another method to increase the efficiency is to manage the flow field. Grimes, et al [10] conducted both a computational and an experimental research on the effect of the fan flow on the printed circuit board with heated metal elements. Both suction and blowing configurations of the fan were investigated. The electronic devices were installed on a plane parallel to the axis of the fan. The effect of these configurations on the flow field and temperature distribution was analyzed. Grimes, et al [11] conducted another research on the fan configuration. This time the effect of the mass flow rate was investigated. They used the same fan and printed circuit-board installation configurations. The results yielded that as the mass flow rate increased, the temperature values around the electronic devices decreased for the suction fan configuration. However, for the blowing fan configuration, it was found that the temperature distribution did not differ significantly with varying mass flow rate.

Muralidharan, et al [12] investigated the effect of fan location on cooling of a telecommunication cabinet. The outer wall of the cabinet was a double wall and an air channel was formed between these two layers of outer wall. Two different fan locations, at the top of the cabinet and at the bottom of the cabinet, were investigated. In addition, the thickness of the air channel was varied. The two criteria that were used were the temperature of the electronics devices installed in the cabinet enclosure and the power consumption of the fans. Romadhon, et al [13] analyzed the flow field and temperature field inside a data center. The electronic equipment were located on racks. Two different rack configurations based on the air inlet and the air outlet locations of the electronics equipment were investigated. Zhang et al [14] conducted a research about aircraft cabin ventilation. The purpose was to optimize the thermal comfort of the passengers and the air age around the passengers. Artificial Neural Network was used to build a mathematical model that predicted the parameter affecting the thermal comfort and air age, and genetic algorithm was used for optimization. Zhang et al [15] performed an experimental investigation on the ventilation strategies for aircraft cabin, where they changed the location of the air inlets. Different inlet and outlet configurations were determined and compared in terms of age of air, velocity and temperature non-uniformities inside the cabin.

Above studies demonstrate the application of an optimization method for heat transfer and cooling of the systems, but the methods mentioned above are also used in the other disciplines. An example is the study of Mallela et al [16] who used the ANN to predict buckling loads of laminated composite stiffened panels. It was stated that designing such panels requires the use of an optimization approach. Therefore, a fast way to determine the buckling load was required. An ANN was trained by the data that was obtained by the Finite Element Analyses to overcome this problem.

Some researchers have used the regression techniques in their investigations without applying an optimization process. Among these techniques, the ANNs have recently pulled the interest of researchers. Ye et al [17] used an ANN to model the convective heat transfer of supercritical carbon dioxide flowing upward in tubes under heating conditions. They stated that the supercritical carbon dioxide is an ideal working fluid for energy conversion systems. The ANN was trained with several experimental data and the results of the trained network were compared with other correlations from the literature. It was stated that the artificial neural network performs better than the correlations. Mitra et al [18] used the ANNs to predict the thermal resistance of cotton fabrics as a function of the ends per inch, picks per inch, and the warp and the weft counts. The experiments were conducted to build the training data set, and the network was trained with this data set.

In another example, Nicola et al [19] trained an ANN to predict the thermal conductivity of organic liquids. The correlations in the literature were reviewed and the same input parameters to these correlations were used as the inputs to the network. They observed that the ANN could predict the thermal conductivity with a small deviation. Similarly, Esfe et al [20] utilized an ANN to predict the thermal conductivity of a nano fluid as a function of the temperature and the ingredient concentrations. The experimental data was used for the training. It was stated that the artificial neural network could predict the thermal conductivity with high accuracy.

1.3. Avionics Bay Geometry

Current study is limited to the avionics bay located at the nose of a rotorcraft. Through an examination of nose geometries of several commercial rotorcraft, a model was generated that is representative of the actual nose geometry in a class of rotorcraft with two engines, a retractable-wheel type landing gear, and a maximum take-off weight varying between 1669 kg and 6400 kg. The definitions of length, height and width are shown in Figure 1.1 and the rotorcrafts within the selected class and the corresponding nose avionics bay dimensions are shown in Figure 1.2. The length, height, and width of the avionics bay used in the current study are obtained by arithmetically averaging the nose avionic bay dimensions of the rotorcrafts within the selected class and shown in Table 1.1.

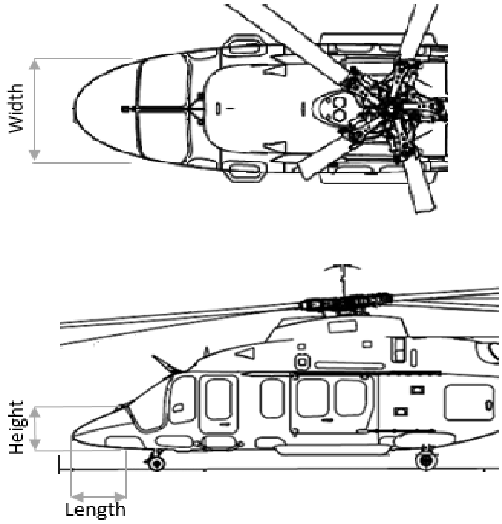

Figure 1.1. Definitions of Length, Height and Width [21]

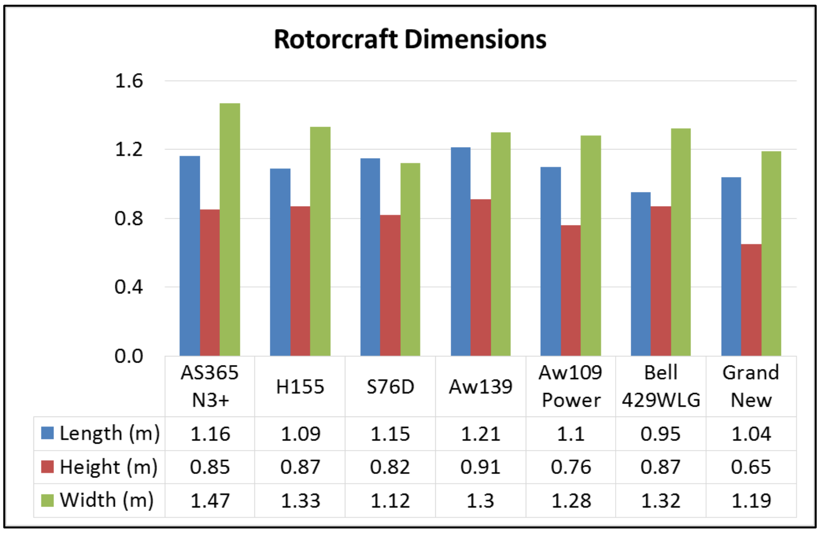

	AS365 N3+	H155	S76D	Aw139	Aw109 Power	Bell 429WLG	Grand New
🟦 Length (m)	1.16	1.09	1.15	1.21	1.1	0.95	1.04
🟥 Height (m)	0.85	0.87	0.82	0.91	0.76	0.87	0.65
🟩 Width (m)	1.47	1.33	1.12	1.3	1.28	1.32	1.19

Figure 1.2. Rotorcrafts Within Selected Class and Corresponding Nose Avionics Bay Dimensions [22], [23], [24], [25], [26], [27], [28], [29], [30], [31] & [32]

Table 1.1. *Dimension of the Nose Avionics Bay*

Length	*Height*	*Width*
1.1 m	0.8 m	1.3 m

In addition, there are eleven avionics equipment in the bay, five of which is installed on the floor and six of which is installed on a rack. Geometry of the avionics bay and avionics equipment numbering are given in Figure 1.3. The skin and floor have 1 mm of thickness each, and the rack is 2 mm thick. The avionics cooling system used in this study utilizes the fan in blowing configuration. i.e. the fan draws air from outside to the interior of the nose avionics bay. Then the supplied air leaves the bay through exhaust opening. Geometries of fan and exhaust can be also seen in Figure 1.3. Fan and exhaust are located at the skin of the nose avionics bay. The diameter of the exhaust is 80 mm and is flush with the skin. The diameter and the length of the fan are 100 mm and 29.5 mm, respectively.

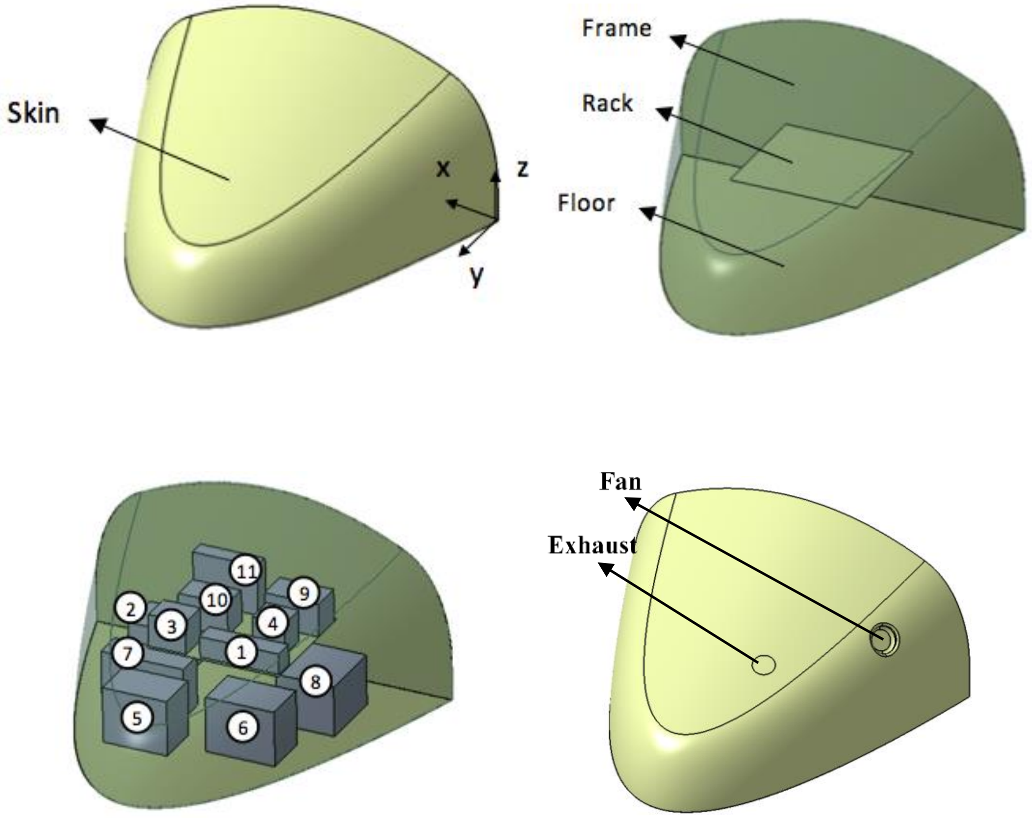

Figure 1.3. Nose Avionics Bay Geometry

1.4. Problem Description and Methodology

In this study, the effect of fan and exhaust locations is investigated. The variation of the required mass flow rate is determined as a function of the fan and the exhaust locations. Placement of fan and exhaust is optimized to find the smallest possible mass flow rate. As it is stated above, the smaller the mass flow rate gets, the lower the system weight and the power consumption become.

An optimization algorithm is utilized to find the best fan and exhaust locations. Optimization is an iterative process, where the mass flow rate is defined as a function of fan and exhaust locations at each iteration. Coupling CFD directly with the optimization algorithm would be an extremely time-consuming process. For this reason, a prediction function is constructed to predict the avionics average surface temperatures as a function of the fan and exhaust locations and the mass flow rate.

A design-of-experiments study is conducted over the pre-determined parameter ranges to establish a set of design points (DPs). Then, the CFD analyses are performed at these DPs and the prediction function is built using the CFD results. In order to determine the accuracy of the prediction function, the average surface temperature predictions are compared with those from CFD using new test points. If found necessary, the prediction function is updated by adding new DPs. The final step is to couple this prediction function with the optimization algorithm to find the optimum fan and exhaust locations that minimize the required mass flow rate. If the mass flow rate obtained via the optimization algorithm is out of pre-defined range, the limits of the range is updated and the new design points are generated until the input range is satisfied. It is important that the ranges for parameters cover the optimum point. The prediction function is formed by the utilization of the CFD results from the DPs and it performs a sort of an interpolation among these CFD results to obtain the avionics average surface temperatures for a point within the parameter ranges. If the point is out of the parameter ranges, an extrapolation is performed. However, the accuracy of the prediction worsens in the case of extrapolation, making it desirable to keep the optimum point within the ranges. The optimization process is shown as a flow chart in Figure 1.4. With the process summarized here, it is aimed to determine the fan and exhaust locations with a precision level that is normally achieved in the detailed design phase of a project in industry.

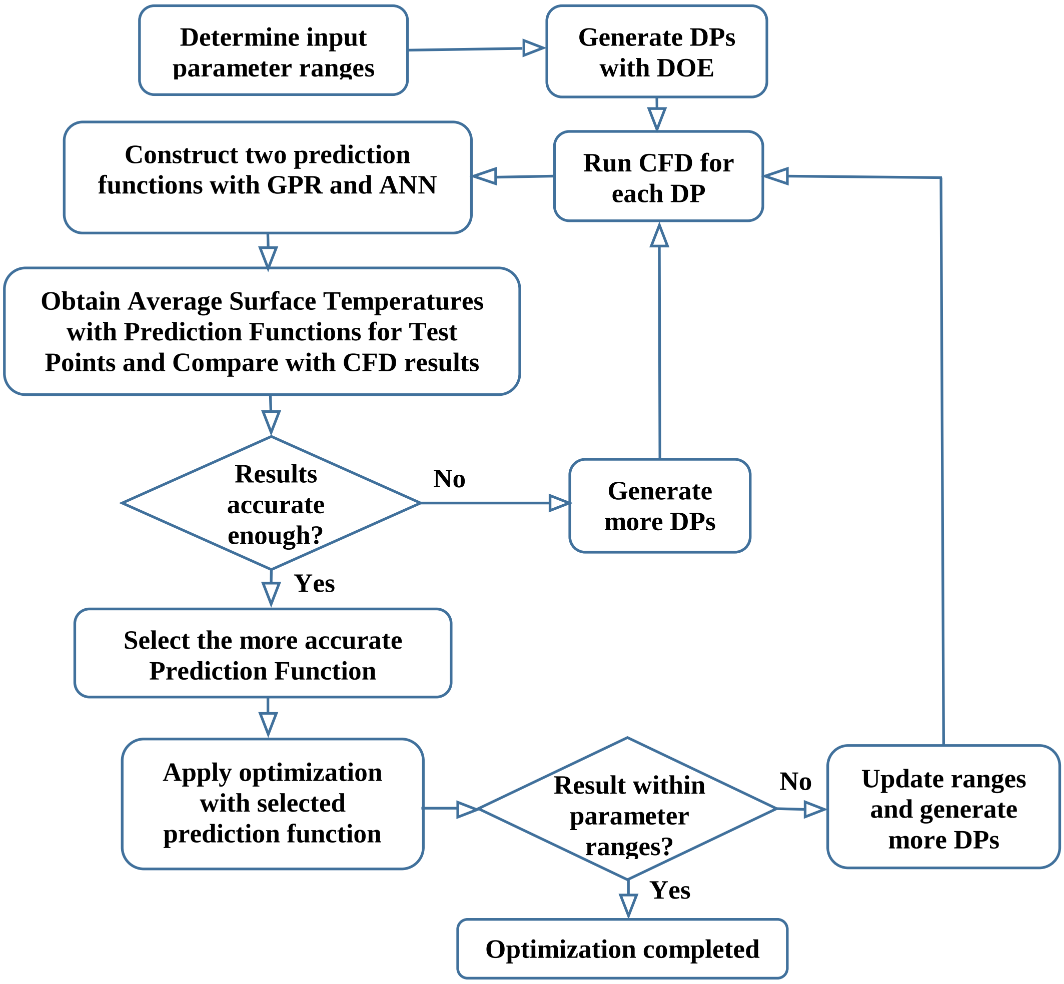

Figure 1.4. Optimization Process Flow Chart

CHAPTER 2

DESIGN OF EXPERIMENT

In this chapter, a design-of-experiments study is carried out to build a CFD analyses matrix. The matrix consists of DPs and a DP consists of a set of numerical values of the prediction function input parameters. The input parameters are the fan and exhaust locations and the fan mass flow rate. Then, a CFD analysis is run for each DP, such that the analysis is set up using the numerical input parameter values of this DP.

2.1. Avionics Temperature Limits

The required mass flow rate is the smallest possible mass flow rate which ensures that the thermal environment inside the bay is suitable for all of the avionics equipment and its value is determined by checking whether avionics operate below their temperature limits or not.

In aviation industry, the operating temperatures limits of avionics are generally stated as the ambient temperature. i.e. the maximum ambient temperature at which the avionics could operate is stated as the limit temperature. The ambient temperature limit for all of the avionics equipment is assumed to be 343.15 K in the current study. In order to assess whether the thermal conditions of the bay is suitable or not, the average air temperature inside the bay may be used. However, it is not possible to check the local temperatures with such an approach. i.e. there might be hot zones inside the bay with temperature values higher than the operating limit, although the overall air average temperature is within the limits. Therefore, another method must be used that accounts for the local hot zones as well.

In order to prove that the equipment operates properly at the stated limit ambient temperature, each equipment is tested by placing them individually inside a temperature controlled chamber. The air velocity inside the chamber is close to zero and the air temperature inside the chamber is set to the limiting ambient temperature. The equipment is operated inside the chamber for a certain amount of time to determine whether they function properly or not.

To account for the local zones, the avionics are tested in the temperature-controlled chambers. The average surface temperatures of all avionics equipment are calculated analytically as they are located at the testing chamber at an ambient temperature of 343.15 K. Then, the calculated surface temperatures are used as the limiting values. That is, the average surface temperatures of the equipment are used to check the thermal environment around the equipment rather than using the ambient temperature directly.

When the avionics are place inside the temperature-controlled testing chamber, the heat loads of the equipment are transferred by free convection to the air inside the chamber and by radiation to the chamber walls. The lower wall of the equipment is in contact with the chambers floor. Therefore, the bottom wall is assumed to be adiabatic. As a result, convection and radiation occur only from the side walls and top wall of the equipment. The heat transfer process from an equipment is shown in Figure 2.1.

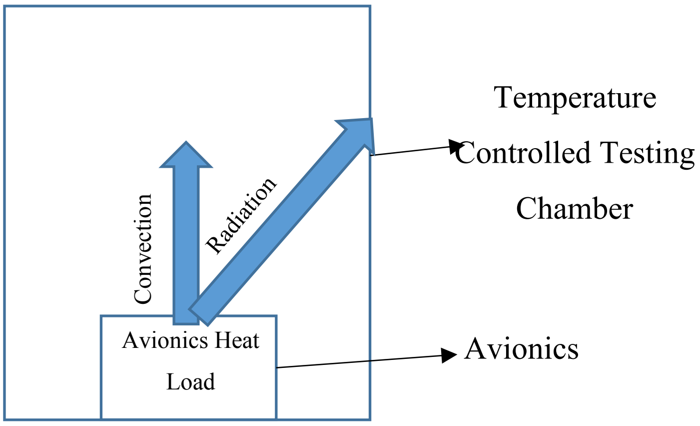

Figure 2.1. Heat Transfer Processes inside Testing Chamber

When a simple energy balance is performed for avionics, Eq.(1) is obtained..

$$Q_{heat\ load} = Q_{radiation} + Q_{convection} \qquad (1)$$

where $Q_{\text{heat load}}$ is the heat load of avionics, $Q_{\text{radiation}}$ is the radiative heat transfer to the walls of the chamber, and $Q_{\text{convection}}$ is the convective heat transfer to the air inside the chamber.

$Q_{\text{radiation}}$ and $Q_{\text{convection}}$ may be obtained by Eq.(2) and Eq.(3). The air temperature inside the chamber is at the limiting temperature (343.15 K) and the walls of the chamber are also assumed to be at the same temperature.

$$Q_{radiation} = \sigma\ \varepsilon_{avionics}\ A_{avionics}\ ({T_{avionics}}^{4} - 343.15K^{4}) \qquad (2)$$

$$Q_{convection} = h_{average}\ A_{avionics}\ (T_{avionics} - 343.15K) \qquad (3)$$

where σ is Stefan Boltzmann constant, $\varepsilon_{avionics}$ is emissivity of the surface of avionics, $A_{avionics}$ is the summation of the areas of the side walls and the top wall of the avionics, $h_{average}$ is the average convective heat transfer coefficient from the side walls and the top wall of the equipment and $T_{avionics}$ is the average surface temperature of the avionics.

$h_{average}$ can be obtained as follows by Eq.(4),

$$h_{average} = \frac{(h_{vertical}\ A_{vertical} + h_{top}\ A_{top})}{A_{avionics}} \qquad (4)$$

where $h_{vertical}$ is the convective heat transfer coefficient by the side walls, h_{top} is the convective heat transfer coefficient by the top wall, $A_{vertical}$ is the area of the side walls and A_{top} is the area of the top wall.

When the Grashof number (Gr) for the vertical walls and the top wall of all avionics equipment is calculated, the flow is found to be laminar (Gr<108) [33]. In Jamnia [33], the following heat transfer coefficient correlations are suggested for the sidewalls and the top wall for laminar flow by Eq.(5) and Eq.(6).

$$h_{vertical} = 1.65 \left(\frac{T_{avionics} - 343.15K}{L}\right)^{0.25} \tag{5}$$

$$h_{top} = 2.06 \left(\frac{T_{avionics} - 343.15K}{L}\right)^{0.25} \tag{6}$$

where L is the height of the vertical walls. On the other hand, L is calculated as shown in Eq.(7) for the top walls. L values are also used as the characteristic dimensions for the calculation of Gr.

$$\frac{1}{L} = \frac{1}{width} + \frac{1}{length} \tag{7}$$

The limits for the avionics average surface temperatures that were obtained by solving above equations are shown in Table 2.1. The heat loads of the avionics are also included.

Table 2.1. *Heat Loads and Surface Temperature Limits*

Avionics Equipment	*Heat Load (W)*	*Temperature limit (K)*
1	15	360.2
2	85	382.7
3	45	385.5
4	35	385.3
5	120	384.7
6	160	393.6
7	130	391.6
8	135	385.0
9	80	399.6
10	45	383.4
11	30	364.6

The required mass flow calculations are performed for the rotorcraft on the ground. Since there is no external air velocity, the amount of heat transferred through the skin and the floor of the avionics bay is lesser. In other words, the ground condition is the worst condition in terms of avionics cooling. The outside air temperature is assumed to be 323.15 K.

2.2. Determining Ranges for Parameters

In order to carry out the design of experiment study, the input parameter ranges must be determined firstly. The fan and exhaust locations are determined by two parameters for each. As it can be seen in Figure 2.2, the center points of the fan and exhaust are first projected onto a horizontal plane. The x and y coordinates of these projected points are the parameters used to determine the locations of the fan and exhaust on the skin.

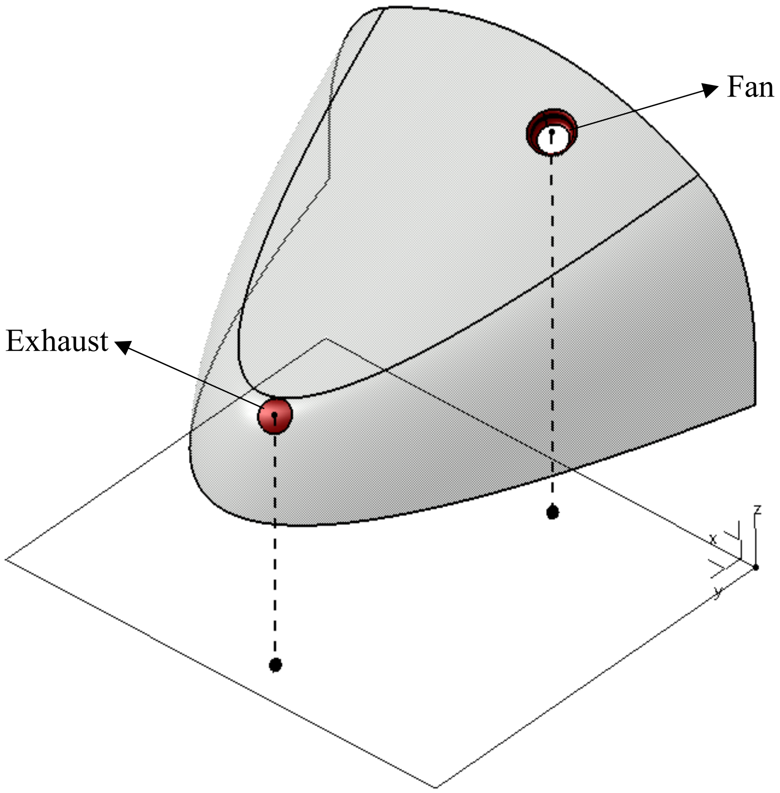

Figure 2.2. Determination of Fan and Exhaust Locations

The ranges of the fan and exhaust locations are formed by the geometry of the skin, the fan and the exhaust, and are shown in Figure 2.3 on the nose avionics bay skin. Due to the irregular shape of the skin, they are represented by equations instead of simple numeric values. The orange-colored curve represents the boundary of the fan location envelope, whereas, the green-colored curve represents the boundary of the exhaust location envelope. In Figure 2.4 and Figure 2.5, the three dimensional orange-colored and the green-colored curves are projected on a horizontal plane similar to the one shown in Figure 2.2. As it can be seen, the ranges for the fan and exhaust locations are the envelopes constrained by a parabola and a line on the horizontal plane. Note that the two envelopes are slightly different. This is due to the different geometries of the fan and the exhaust.

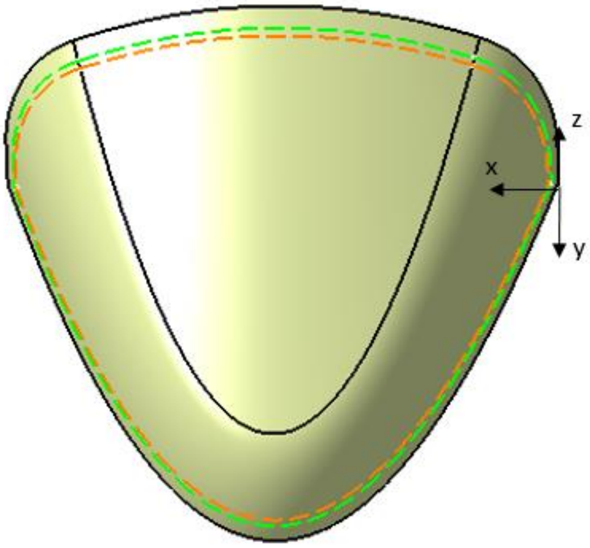

Figure 2.3. Fan and Exhaust Envelopes on Nose Skin

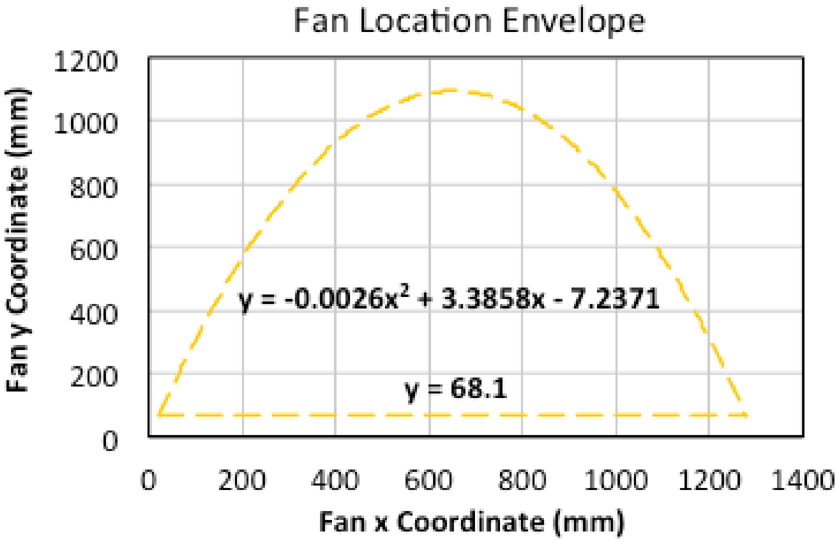

Figure 2.4. Fan Envelope Projected on Horizontal Plane

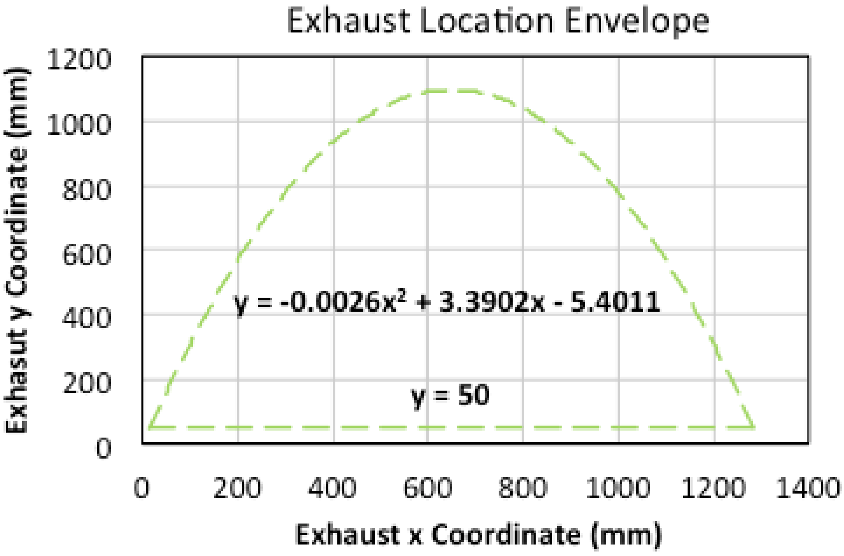

Figure 2.5. Exhaust Envelope Projected on Horizontal Plane

Determination of the upper and lower limits for the mass flow rate is a less of a straight forward procedure compared to that of the fan and exhaust locations. A very large mass flow rate for the upper limit and a zero mass flow rate for the lower limit could be selected to ensure that the range includes the optimum point. However, such a larger range would require a higher number of DPs to generate an accurate enough prediction function. A CFD analysis is run for each DP, and the CFD analyses are time consuming. Therefore, the range of the parameters has to be narrowed down as much as possible.

To determine the upper limit of mass flow rate range, the fan and exhaust locations given in Table 2.2 are selected randomly. Then a series of CFD analyses are run for this fan-exhaust arrangement with different mass flow rate values. The aim is to determine the approximate required mass flow rate that keeps all of the avionics surface temperatures below the limiting values. The mass flow rate values are selected by a trial-and-error process.

The mass flow rate obtained by this process is selected as the upper limit of the range. It is mostly like that the randomly selected fan and exhaust locations are not the optimum ones. Due to this reason, it is expected that the required mass flow rate of the optimum case will be most probably lower than the value obtained by this procedure. Therefore, it can be concluded that the mass flow rate obtained could be used as the upper limit of the mass flow rate range.

On the other hand, if it is found out that the randomly selected fan and exhaust locations are the optimum ones by chance, then the optimization algorithm will also converge to this randomly selected point.

Table 2.2. *Selected Fan and Exhaust Locations*

Fan Location		*Exhaust Location*	
x coordinate (mm)	*y coordinate (mm)*	*x coordinate (mm)*	*y coordinate (mm)*
1200.5	132.4	57.0	153.6

The selected fan and exhaust locations are also graphically shown in Figure 2.6.

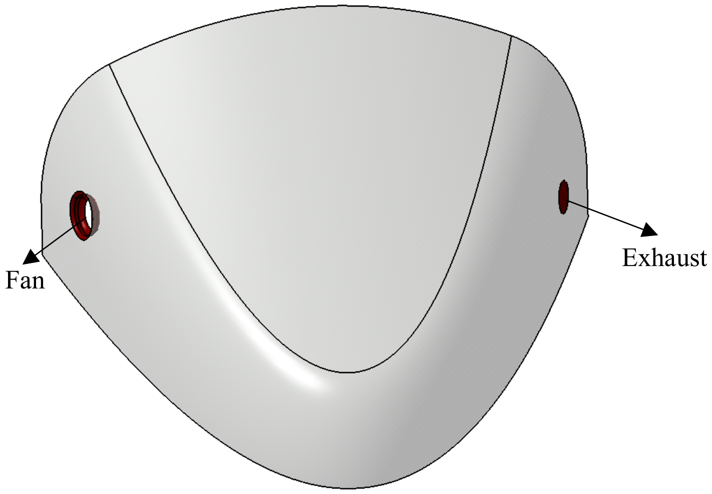

Figure 2.6. Locations of Selected Fan and Exhaust Locations for the Determination of Mass Flow Rate Upper Limit

The purpose is to determine the upper limit and not the precise value of the required mass flow rate. Determining the lowest mass flow rate with a high accuracy would be too time consuming, since a CFD analysis is run at each iteration. Therefore, the process is stopped when some of the avionics surface temperatures get close enough to their limiting values.

The upper limit for the mass flow rate range becomes 0.055 kg/s. The average surface temperatures obtained by CFD are shown in Table 2.3. The details of the CFD analyses will be provided in the next chapters. The average surface temperature of avionics 1 is the one closest to its limiting value. Therefore, the required minimum mass flow rate is mainly determined by avionics 1. In addition, the volume-averaged solid temperatures inside the avionics are also shown in Table 2.3. As it can be seen, those values are close to the averages surface values. As it is explained in CHAPTER

3, the material of avionics has a high thermal conductivity. Therefore, the heat load of the equipment could be transferred inside the avionics by conduction even with small temperature gradients, which results in small differences between the average surface values and volume-averaged values.

Table 2.3. *Avionics Average Temperature Results*

Avionics Equipment Number	*Average Surface Temperature (K)*	*Volume-Averaged Temperature (K)*
1	357.7	357.8
2	351.7	351.8
3	381.4	381.5
4	378.3	378.4
5	371.4	371.6
6	378.2	378.4
7	381.6	381.7
8	370.0	370.0
9	385.2	385.3
10	377.5	377.6
11	352.9	352.9

An approximation for the lower limit of mass flow rate can be made by using a simple energy balance for the nose avionics bay. The temperature field inside the bay is assumed to be uniform and at the ambient temperature limits of the avionics, i.e 343.15 K. That is, the air supplied by the fan is distributed so effectively that no hot zones inside the bay occur. In case of the existence of such hot zones, the mass flow rate has to be increased further to reduce the temperature level of these zones below 343.15 K. Therefore, the uniform-temperature assumption is for an idealized situation and it is expected that the mass flow rate calculated for this case will be smaller than the optimum case. In case it turns out that the mass flow rate of the optimum case is less than the lower limit, additional DPs will be added and the prediction function will be improved to extend over this new mass flow rate range accurately.

The temperature of the air supplied to the avionics bay by the fan is the same as the outside air temperature (323.15 K) and the temperature of the air passing through the exhaust of the bay is also 343.15 K. As it can be seen in Figure 2.7, the heat loads of the avionics are transferred to the air supplied by the fan and to the outside air across the skin and the floor of the avionics bay.

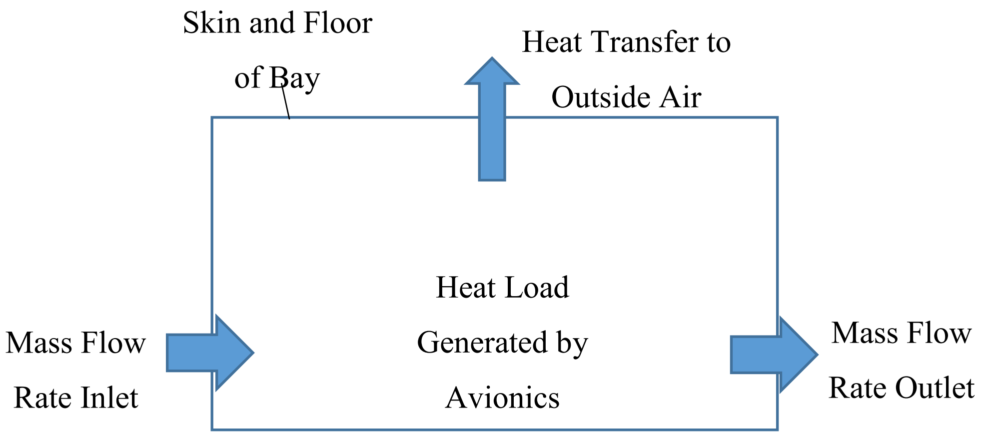

Figure 2.7. Energy Balance for Avionics Bay

Therefore the following energy balance equation Eq.(8) may be solved to obtain the required mass flow rate.

$$\dot{m}\, c_p \left(T_{exhaust} - T_{fan}\right) = \left(\sum_{\substack{avionics\\1}}^{\substack{avionics\\11}} Q_{heat\ load}\right) - Q_{outside} \qquad (8)$$

where $\dot{m}$ is the mass flow rate of the fan, c_p is specific heat of air, $T_{exhaust}$ is the air temperature at the exhaust, T_{fan} is the temperature of air supplied to the bay by the fan, $Q_{heat\ load}$ is the heat load generated by the avionics and $Q_{outside}$ is the heat transferred to the outside air through the skin and the floor of the bay.

$Q_{outside}$ is calculated by Eq.(9).

$$Q_{outside} = U(A_{skin} + A_{floor})(T_{inner\ wall} - T_{outside}) \qquad (9)$$

Here, U is the overall heat transfer coefficient, A_{skin} is the area of the skin of the bay, A_{floor} is the area of the floor of the bay, $T_{inner\ wall}$ is the average temperature of the inner wall surfaces of the skin and the floor, and $T_{outside}$ is the outside air temperature.

U and $T_{inner\ wall}$ must be known to be able to solve equations Eq.(8) and Eq.(9). Additional equations for these two unknowns are obtained by an investigation of the heat transfer process through the skin and the floor as shown in Figure 2.8.

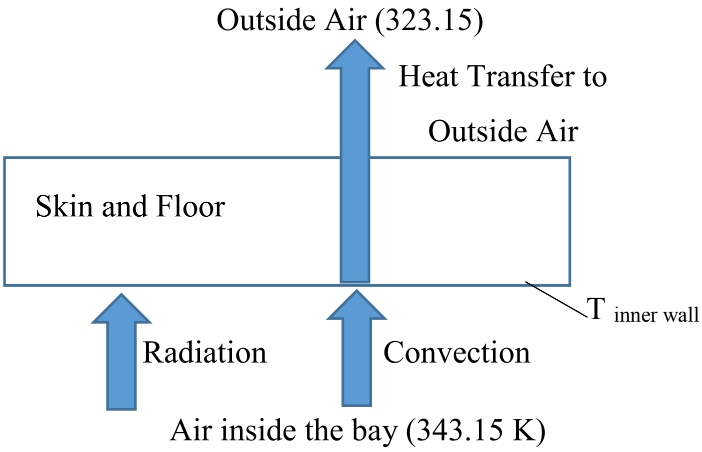

Figure 2.8. Heat Transfer Across Skin and Floor

Heat transfer between the inner wall of the skin and the floor and the outside air occurs by conduction and convection. Therefore, U in Eq.(9) can be calculated as follows by Eq.(10).

$$U = \frac{k}{l} + h_{outside} \qquad (10)$$

where k is the thermal conductivity of the skin and floor material, l is the thickness of the skin and the floor, and $h_{outside}$ is the convective heat transfer coefficient at the outer surface of the skin and the floor.

The outside wind velocity is taken as zero in order to be more conservative. $h_{outside}$ is equal to 11.35W/m^{2}K, when the wind velocity is zero[34]. As the wind velocity increases, $h_{outside}$ increases, and a larger amount of heat could be transferred through the skin and floor.

In addition, $T_{inner\,wall}$ must be known to be able to solve Eq.(8) and Eq.(9) for mass flow rate. A surface energy balance at the inner surfaces of the skin and floor is used to determine $T_{inner\,wall}$. With the help of Figure 2.8, the surface energy balance in Eq.(11) can be written:

$$Q_{outside} = Q_{radiation} + Q_{convection} \tag{11}$$

Here, $Q_{radiation}$ is the net radiative heat transfer occurring by the inner surface of the skin and the floor and $Q_{convection}$ is the convective heat occurring between the inner wall surface of the skin and the floor and the air inside the nose avionics bay.

$Q_{radiation}$ is be calculated by Eq.(12)

$$Q_{radiation} = \alpha E_{irradiation} - E_{emission} \tag{12}$$

α represents the absorptivity of the inner surface of the skin and the floor, $E_{irradiation}$ is the radiation incident on these surfaces and $E_{emission}$ is the radiation emitted by the same surfaces.

$E_{irradiation}$ and $E_{emission}$ can be calculated by Eq.(13) and Eq.(14).

$$E_{irradiation} = \sum_{i=1}^{11} [f\sigma\,(A_{skin} + A_{floor})\,(\varepsilon_{avionics}\ T_{avionics}{}^{4}\,)] \tag{13}$$

$$E_{emission} = \sum_{i=1}^{11} [f\sigma\,(A_{skin} + A_{floor})\,(\varepsilon_{inner\,wall}\ T_{inner\,wall}{}^{4}\,)\,] \tag{14}$$

where f is the view factor from the inner surface of the skin and the floor to each avionics equipment, σ is the Stefan Boltzmann constant, $\varepsilon_{avionics}$ is the emissivity of the surface of avionics, $T_{avionics}$ is the average surface temperature of avionics and $\varepsilon_{inner\ wall}$ is the emissivity of the inner surface of the skin and the floor.

In Eq.(13), it is assumed that the only source of irradiation is the radiation emitted by the avionics equipment. Normally, there is one more irradiation component. This component is the radiation reflected by the surfaces of avionics. The surfaces of the avionics have a low reflectivity value. Additionally, including the reflectivity in the calculation of radiation makes it significantly more difficult to solve. Due to these two reasons, irradiation due to reflectivity is neglected.

The limiting average surface temperatures are defined as $T_{avionics}$ in Eq.(13) and the view factors in Eq.(13) and Eq.(14) are obtained from the CFD model in the software used for the analyses. The view factors are given in Table 2.4.

Table 2.4. *Avionics Equipment View Factors*

Avionics Equipment Number	*View Factor*
1	0.0207
2	0.0292
3	0.0238
4	0.0134
5	0.0641
6	0.0633
7	0.0308
8	0.0434
9	0.0168
10	0.0168
11	0.0189

Finally, Q convection may be obtained by equation Eq.(15).

$$Q_{convection} = h_{inside}(A_{skin} + A_{floor})(T_{inside} - T_{inner\ wall}) \tag{15}$$

h_{inside} is the convective heat transfer coefficient between the inner surface of the skin and the floor and the air inside the bay, T_{inside} is the average air temperature inside the bay.

h_{inside} is calculated by Eq.(16) as described in [34].

$$h_{inside} = 11.35 + 1.781\ V_{inside} \tag{16}$$

Here V_{inside} is the average air velocity magnitude inside the bay.

In order to determine h_{inside}, the air velocity magnitude inside the bay must be known. The velocity magnitude inside the bay is assumed to be zero as an initial guess. Then the set of equations above are solved to determine the lower limit of the range of the mass flow rate. The CFD analysis is carried out with the calculated mass flow rate, and the fan and exhaust locations shown in Figure 2.6 are used. The average air velocity magnitude inside the bay is obtained from the CFD analysis and h_{inside} value is updated. The mass flow rate is calculated again with the new h_{inside} value. This process is repeated a couple of times until the average air velocity inside the bay and the mass flow rate becomes compatible.

The average air velocity magnitude inside the bay will change depending on the fan and exhaust locations. The only purpose of the calculations carried out for the lower limit of the mass flow rate range is to be able to narrow down the range. Therefore, the only expectation from the mass flow rate lower limit is to be smaller than the optimum value. As a result, the assumptions made during the calculation of the lower limit do not affect the accuracy of the optimization process directly.

As a result of this process, the lower limit of the mass flow rate is found to be 0.024 kg/s.

2.3. Design of Experiment Study

For the Design of Experiment study, the Model-Based Calibration toolbox of Matlab [35] is used. There are three different types of design-of-experiments methods, namely Classical Designs, Optimal Designs and Space Filling Designs. The method of Classical Designs can be used only for the box-like input parameter domains. Due to the fan and exhaust location envelopes, the domain of the current study is irregular shaped. As a result, classical designs could not be used in the Design of Experiment study. The method of Optimal Designs can be used for the irregular-shaped domains, but it requires detailed prior knowledge on the type of the mathematical model that will be fit to the data points, and can only be used with linear regression models. On the other hand, according to Montgomery [36], the method of Space Filling Designs is a suitable option for the computational investigations where there is no prior detailed information on the data to be fit, as is the case in the current study. This method can also be used for the irregular-shaped domains. Hence, the method of Space Filling Designs is selected to generate the design points in this study.

The aim of the Space Filling Design is to distribute the design points across the domain evenly. There are different methods to perform this distribution. In this study, Halton Sequence model is used to generate the DPs. This method is a low-discrepancy one. For instance, a Design of Experiment study is created with fifty DPs. Then, it is desired to increase the number of DPs and a new study is performed that generates sixty DPs. When low-discrepancy methods are used, the first fifty DPs of the latter study are same as the fifty points of the first study. On the other hand, if other methods were used, the second study would yield a completely new set of DPs. At the beginning of this study, it was not known how much DPs were required to build an accurate enough prediction function. Therefore, the number of the DPs was required to be increased progressively during the study. If a low-discrepancy method was not selected, the DPs would start to become unevenly distributed over the parameter domain; as the number of DPs were increased progressively. This would result in a prediction function, which is more accurate at some portions of the domain and less accurate at other parts of domain.

Halton Sequence utilizes index numbers to generate DPs. A different prime base is appointed for each of the five input parameters. Then the index number is expanded at the appointed prime bases by five times, and the coefficients of expansions are obtained as given by Eq.(17) [37].

$$t = \sum_{i=0} a_i {e_j}^i \tag{17}$$

Where t is the index of the DP, a's are the coefficients of expansion and e is the base of expansion.

Then a number between 0 and 1 is obtained for each of the five expansions by the utilization of radical inverse function as given in Eq.(18). [37]

$$\phi_{e_j(n)} = \sum_{i=0} a_i {e_j}^{-i-1} \tag{18}$$

where ϕ is the number obtained by the Halton Sequence procedure.

Then ϕ's are scaled with the actual ranges of the input parameters to determine the input parameter's numerical values stored by the DP. The procedure is repeated with the next index number to generate the next DP. The Halton Sequence procedure is explained in detail by an example in APPENDIX A.

It is found out that one hundred and seventy seven DPs are required to obtain an accurate enough prediction function. The DPs are shown in Appendix B in tabular form. In addition, the generated DPs are shown on the fan and exhaust location envelopes in Figure 2.9 and Figure 2.10. Here, the fan location envelope in Figure 2.9 is divided into four quadrants with each depicted with a different color. In addition to the coloring, those fan locations coinciding with the curved side surface of the skin are also circled in black to distinguish them from the others at the top of the skin. Then, each exhaust location that belongs to a fan/exhaust pair is coded with the same color with its corresponding fan location and is demonstrated in the exhaust location envelope in Figure 2.10. The exhaust locations that pair up with the fan locations that are on the side surface are circled in black as well. It can be observed that the DPs are indeed evenly distributed across the whole domain.

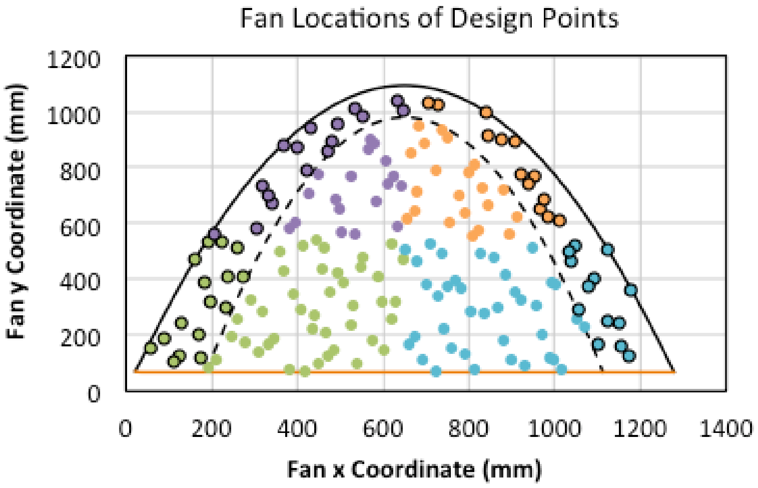

Figure 2.9. Fan Locations of Design Points

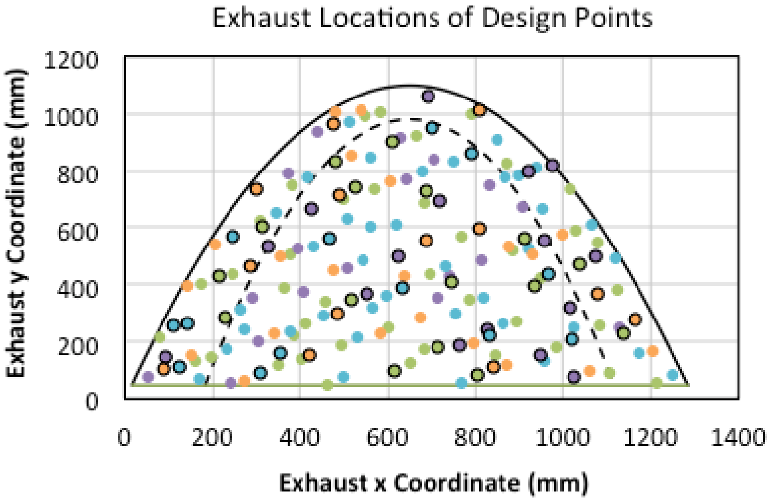

Figure 2.10. Exhaust Locations of Design Points

The design-of-experiment study could have generated DPs with coincident fan and exhaust locations, since no constraints regarding this issue were applied. However, it is observed that such a case does not occur. Therefore, an extra effort to apply such a constraint was not made.

CHAPTER 3

CFD ANALYSES

In this chapter, the details about the CFD analyses carried out for the DPs are given. The following sections will summarize the governing equations and the turbulence models used, the validation study performed, the mesh sensitivity, and the analysis for the calculation of the numerical error.

3.1. Problem Setup

Fluent Release 18.1 is used to run the CFD analyses. During the calculations, the energy equation is activated to solve for the temperature field inside the bay. In addition, radiative heat transfer is accounted for by the utilization of the surface-to-surface radiative heat transfer model. The Realizable k-ε turbulence model is used to account for turbulence with enhanced wall treatment. The Realizable k-ε turbulence model is generally known to provide accurate predictions for separated flows, spreading rate of round jets, and flows with complex features [38]. In addition, the enhanced wall treatment is used to capture hydraulic and thermal boundary layers around the avionics more accurately.

The pressure-based coupled solver of Fluent Release 18.1 [38] is used in the analyses. The second order upwind scheme is used for the spatial discretization of all conservation equations. The results are obtained through a pseudo-transient analysis utilizing time-stepping as a way of under relaxation to improve convergence of the solution.

In addition, stagnant zones may occur inside the bay depending on the fan and exhaust locations. At these stagnant zones, natural convection becomes important. Therefore, gravity is also enabled to account for natural convection.

The analyses are carried out on a workstation including two processors with a total physical core number of 16. In addition, the workstation has 64 gigabytes of physical memory. It takes about one and a half hours to complete a CFD analysis for a DP.

3.2. Governing Equations

Conservation of mass, conservation of momentum and conservation of energy equations are solved to obtain the results.

In order to account for turbulence, turbulence viscosity method is used. Firstly, the flow variables are decomposed into mean and fluctuating components. During the analyses, natural convection is also accounted for as there could be regions inside the bay where air is stagnant. The density is taken as a variable so that natural convection can also be accounted for in the analysis as there are potential regions of stagnant air inside the bay. The "Incompressible Ideal Gas" model of the commercial CFD program is selected for the air density. That is, the density of the air changes with only temperature but not with pressure. In the Boussinesq buoyancy force approximation, the density is treated as a variable only in the buoyancy force term of the conservation of momentum equation. But here, the density is treated as a variable in all applicable terms of the conservation equations. Due to this variable density model, the velocity component could not be decomposed into its mean and fluctuating components by using the standard time averaging. The mean component is obtained as in Eq.(19) by including the density as well.

$$\tilde{u}_i = \frac{1}{\bar{\rho} t} \int_0^t \rho u_i d\tau \tag{19}$$

Then as given in Eq.(20), the fluctuation part becomes.

$$u_i'' = u_i - \tilde{u}_i \tag{20}$$

Inserting above expressions into the conservation equations, following equations (Eq.(21), Eq.(22) and Eq.(23)) are obtained. The obtained conservation of momentum equation is called the Favre Averaged Navier-Stokes rather than the Reynolds

Averaged Navier-Stokes due to the averaging method of the mean velocity component.

$$\frac{\partial}{\partial x_i}(\bar{\rho}\,\tilde{u}_i) = 0 \tag{21}$$

$$\frac{\partial}{\partial x_j}\left(\bar{\rho}\tilde{u}_i\tilde{u}_j\right) = -\frac{\partial\overline{\rho u_i'' u_j''}}{\partial x_j} - \frac{\partial \bar{p}}{\partial x_i} + \frac{\partial}{\partial x_j}\left[\mu\left(\frac{\partial \tilde{u}_i}{\partial x_j} + \frac{\partial \tilde{u}_j}{\partial x_i} - \frac{2}{3}\delta_{ij}\frac{\partial \tilde{u}_l}{\partial x_l}\right)\right] + \bar{\rho} g_i \tag{22}$$

$$\frac{\partial}{\partial x_i}(\tilde{u}_i(\bar{\rho}E + \bar{p}) = \frac{\partial}{\partial x_j}\left[k_{eff}\left(\frac{\partial T}{\partial x_j}\right)\right] \tag{23}$$

Here, ρ is the density, u is the velocity component, p is pressure, g is the gravitational vector component, μ is the viscosity, δ is the Kronecker-Delta function, E is total energy, k_{eff} is the effective thermal conductivity, and T is the temperature. The bar notation means that the variable is time averaged.

In order to be able solve above equation, additional equations are required to determine $\overline{\rho u_i'' u_j''}$ term. The Boussinesq approach is used to determine this term as in Eq.(24).

$$-\overline{\rho u_i'' u_j''} = \mu_t\left(\frac{\partial \tilde{u}_i}{\partial x_j} + \frac{\partial \tilde{u}_j}{\partial x_i}\right) - \frac{2}{3}\left(\bar{\rho} k_{turb} + \mu_t \frac{\partial \tilde{u}_k}{\partial x_k}\right)\delta_{ij} \tag{24}$$

where μ_t is the turbulence viscosity and k_{turb} is the turbulent kinetic energy.

In addition, the effective thermal conductivity term, k_{eff}, exists in the conservation of energy equation Eq.(23) , which is also calculated by the utilization of the turbulence viscosity as given by Eq.(25).

$$k_{eff} = k + \frac{c_p\,\mu_t}{Pr_t} \tag{25}$$

where k is the thermal conductivity and c_p is specific heat.

The governing equations given above are for the fluid domain. During the analyses, avionics are modeled as blocks of solids and volumetric heat sources are defined for these blocks to represent the heat loads of the equipment. Therefore, the energy equations is also solved for solids during the analyses. The energy equations takes the form given by Eq.(26) for the solids.

$$\frac{\partial}{\partial x_j}\left[k\left(\frac{\partial T}{\partial x_j}\right)\right] + S_E = 0 \tag{26}$$

where S_E is energy source term.

3.2.1. Turbulence Models

Fluent software offers different turbulence models to determine turbulence viscosity. In the following sections, four of these models are briefly introduced. These models are the Standard k-ε turbulence model, Renormalization Group (RNG) k-ε turbulence model, Realizable k-ε turbulence model and Shear-Stress Transport (SST) k-ω turbulence model, namely. During the analyses of the DPs, the Realizable k-ε turbulence model is used as stated above. However, analyses with the other turbulence models are carried out as well, in order to evaluate the effect of the turbulence model selection on the results. All of these analyses are carried out with the same mesh and the findings are presented in CHAPTER 6.

3.2.1.1. Standard k-ε Turbulence Model

The turbulence viscosity, μ_t, is calculated as a function of turbulence kinetic energy (k_{turb}) and turbulence dissipation rate (ε) via Eq.(27).

$$\mu_t = \overline{\rho} C_\mu \frac{{k_{turb}}^2}{\varepsilon} \tag{27}$$

Here, C_μ is a constant and ε is the turbulence dissipation rate,

This model is a semi-empirical model for high Reynolds numbers that has been extensively used and is known to provide reasonable accuracy for a wide range of turbulent flows [38]. Following additional equations (Eq.(28) and Eq.(29)) are solved to obtain the turbulence kinetic energy and turbulence dissipation rate.

$$\frac{\partial}{\partial x_i}(\bar{\rho} k_{turb} \tilde{u}_i) = \frac{\partial}{\partial x_j}\left[\left(\mu + \frac{\mu_t}{\sigma_k}\right)\frac{\partial k_{turb}}{\partial x_j}\right] + G_k + G_b - \bar{\rho}\varepsilon - Y_M + S_k \quad (28)$$

$$\frac{\partial}{\partial x_i}(\bar{\rho} \varepsilon \tilde{u}_i) = \frac{\partial}{\partial x_j}\left[\left(\mu + \frac{\mu_t}{\sigma_\varepsilon}\right)\frac{\partial \varepsilon}{\partial x_j}\right] + C_{1\varepsilon}\frac{\varepsilon}{k_{turb}}(G_k + C_{3\varepsilon} G_b) - C_{2\varepsilon}\bar{\rho}\frac{\varepsilon^2}{k_{turb}} + S_\varepsilon \quad (29)$$

where σ_k is the Prandtl number for turbulence kinetic energy, σ_ε is the Prandtl number for turbulence dissipation rate, G_k and G_b represents the generation of turbulence due to mean velocity gradients and buoyancy, respectively. Y_M is the contribution of the fluctuating dilatation incompressible turbulence to the overall dissipation rate, $S_k$and S_ε are the source terms for turbulence kinetic energy and turbulence dissipation rate, respectively. $C_{1\varepsilon}, C_{2\varepsilon}$ and $C_{3\varepsilon}$ are the model constants. The bar notation means that the variable is time averaged.

G_k, G_b and Y_M terms are calculated by Eq.(30) - Eq.(32).

$$G_k = \mu_t S^2 \quad (30)$$

$$G_b = \beta g_i \frac{\mu_t}{Pr_t}\frac{\partial T}{\partial x_i} \quad (31)$$

$$Y_M = 2\bar{\rho}\varepsilon\frac{k_{turb}}{a^2} \quad (32)$$

S is the modulus of the mean rate-of-strain tensor, β is thermal expansion coefficient, Pr_t is the turbulence Prandtl number and a is speed of sound.

3.2.1.2. RNG k-ε Turbulence Model

The standard k-ε turbulence model is improved using a statistical technique, producing the RNG k-ε turbulence model. Due to the additional features it has, such as the improvement in swirling flow predictions and the involvement of low Reynolds number effects, the RNG k-ε turbulence model is known to be more reliable for a wider range of flows [38]. The turbulence viscosity is also determined by equation

Eq.(27). To obtain the turbulence kinetic energy and the turbulence dissipation rate, the following equations (Eq.(33) and Eq.(34)) are solved:

$$\frac{\partial}{\partial x_i}(\bar{\rho} k_{turb}\tilde{u}_i) = \frac{\partial}{\partial x_j}\left[\alpha_k \mu_t \frac{\partial k_{turb}}{\partial x_j}\right] + G_k + G_b - \bar{\rho}\varepsilon - Y_M + S_k \tag{33}$$

$$\begin{aligned}\frac{\partial}{\partial x_i}(\bar{\rho}\varepsilon\tilde{u}_i) = {} & \frac{\partial}{\partial x_j}\left[\alpha_\varepsilon \mu_t \frac{\partial \varepsilon}{\partial x_j}\right] + C_{1\varepsilon}\frac{\varepsilon}{k_{turb}}(G_k + C_{3\varepsilon}G_b) - C_{2\varepsilon}\bar{\rho}\frac{\varepsilon^2}{k_{turb}} \\ & - R_\varepsilon + S_\varepsilon\end{aligned} \tag{34}$$

Here, α_k is the inverse effective Prandtl number for turbulence kinetic energy and α_ε is the inverse effective Prandtl number for turbulence dissipation rate.G_k, G_b and Y_M are calculated similarly to the Standard k-ε Turbulence Model.

3.2.1.3. Realizable k-ε Turbulence Model

For the Realizable k-ε Turbulence Model, the following transport equations (Eq.(35) and Eq.(36)) are used to solve for turbulence kinetic energy and turbulence dissipation rate. The turbulence viscosity is also determined by equation Eq.(27).

$$\frac{\partial}{\partial x_i}(\bar{\rho} k_{turb}\tilde{u}_i) = \frac{\partial}{\partial x_j}\left[\left(\mu + \frac{\mu_t}{\sigma_k}\right)\frac{\partial k_{turb}}{\partial x_j}\right] + G_k + G_b - \bar{\rho}\varepsilon - Y_M + S_k \tag{35}$$

$$\begin{aligned}\frac{\partial}{\partial x_i}(\bar{\rho}\varepsilon\tilde{u}_i) = {} & \frac{\partial}{\partial x_j}\left[\left(\mu + \frac{\mu_t}{\sigma_\varepsilon}\right)\frac{\partial \varepsilon}{\partial x_j}\right] + \bar{\rho}C_1 S\varepsilon - \bar{\rho}C_2\frac{\varepsilon^2}{k_{turb} + \sqrt{\nu\varepsilon}} \\ & + C_{1\varepsilon}\frac{\varepsilon}{k}C_{3\varepsilon}G_b + S_\varepsilon\end{aligned} \tag{36}$$

with

$$C_1 = max\left[0.43, \frac{S\frac{k_{turb}}{\varepsilon}}{5 + S\frac{k_{turb}}{\varepsilon}}\right] \tag{37}$$

where C_2 is a model constants, and G_k, G_b and Y_M are calculated similarly to the Realizable k-ε Turbulence Model.

3.2.1.4. SST k-ω Turbulence Model

This approach uses the k-ω model in the near-wall region and k-ε model further away from the wall. It has been confirmed that the SST k-ω turbulence model has better performance in predicting adverse pressure gradients [39]. For the SST k-ω Turbulence Model, turbulence viscosity is calculated via Eq.(38)- Eq.(41).

$$\mu_t = \frac{\bar{\rho} k_{turb}}{\omega} \frac{1}{\max\left[\frac{1}{\alpha^*}, \frac{SF_2}{a_1 \omega}\right]} \tag{38}$$

$$\alpha^* = \alpha^*{}_{\infty} \left(\frac{\alpha^*{}_0 + \frac{\bar{\rho} k_{turb}}{6\mu\omega}}{1 + \frac{\bar{\rho} k_{turb}}{6\mu\omega}} \right) \tag{39}$$

$$F_2 = \tanh\left(\phi_2{}^2\right) \tag{40}$$

$$\phi_2 = max\left[2\frac{\sqrt{k_{turb}}}{0.09\omega y}, \frac{500\mu}{\bar{\rho} y^2 \omega}\right] \tag{41}$$

where ω is the specific turbulence dissipation rate, S is the modulus of the mean rate-of-strain tensor, y is the distance to the next surface, and $\alpha^*{}_{\infty}, \alpha^*{}_0$ are the model constants.

The transport equation for turbulence kinetic energy and specific turbulence dissipation rate are given in Eq.(42) and Eq.(43).

$$\frac{\partial}{\partial x_i}\left(\bar{\rho} k_{turb} \tilde{u}_i\right) = \frac{\partial}{\partial x_j}\left[\Gamma_k \frac{\partial k_{turb}}{\partial x_j}\right] + G_k - Y_k + S_k \tag{42}$$

$$\frac{\partial}{\partial x_i}\left(\bar{\rho} \omega \tilde{u}_i\right) = \frac{\partial}{\partial x_j}\left[\Gamma_\omega \frac{\partial \omega}{\partial x_j}\right] + G_\omega - Y_\omega + D_\omega + S_\omega \tag{43}$$

$\Gamma_k$and Γ_ω are the effective diffusivities of turbulence kinetic energy and specific turbulence dissipation rate, respectively. G_k represents the production of turbulence kinetic energy and G_ω represents the production of specific turbulence dissipation rate.

Y_k and $Y_\omega$represent the dissipation of k_{turb} and ω due to turbulence, respectively. D_ω is the cross-diffusion term, S_k is turbulence kinetic energy source term, and S_ω is the specific turbulence dissipation rate source term.

For the SST k-ω turbulence model, the residuals stayed at the level of 2x10^{-3} during the CFD calculation. The monitored values of local velocity were found to be oscillating within approximately 0.4 m/s. The oscillation in average avionics surface temperatures was around 2.5K on average, while up to 4.5K of variations could be observed. Since y+ was kept below 1 across the domain, the mesh is considered to be refined enough. When the mesh for the boundary layer was further refined, the oscillations were still observable in the solution. Keeping this in mind, the results from the SST k-ω turbulence model is also included in CHAPTER 6 so that a comparison with the predictions from the other turbulence models can be performed to a reasonable approximation.

3.3. Validation Study

Literature is reviewed to obtain experimental data for a case related to avionics bay cooling. However, there is a lack of studies related to the avionics bay cooling in literature. Therefore instead, a case with simple geometry producing similar flow patterns to those observed in a cooled avionics bay is selected, with the goal of matching the general trends in the experiments. It should be noted that it is not a straightforward task to perform a validation for such a complex geometric model. Hence, in support of this effort, the discretization error and convergence in computational analyses will be introduced in the next sections, which demonstrate the confidence in the results. In the avionics bay, free jet flows occur due to the use of the fan. This jet impinges on the avionics equipment and the walls of the bay. On the other hand, an air flow with smaller velocity magnitudes, where buoyancy forces may be effective, is observed at the zones in the absence of the free jet and impingement.

The study of D. Singh et al [40] is selected as for validation. The geometry of the validation case is shown in Figure 3.1. A cylinder is heated by using a stainless steel foil. A free jet is formed by a nozzle that is located above the heated cylinder. In addition, the heated cylinder is confined by a semi-cylinder. This case includes a free jet with impingement. In addition, a flow field with lower velocity values is observed at the points out of the jet and the impingement zone.

The dimensions and boundary conditions are not directly stated in [40]. The results are represented by the utilization of non-dimensional parameters. These parameters are the Reynolds number of the free jet, the ratio of the heated cylinder diameter to that of the confinement, and the ratio of the nozzle-heated cylinder distance to the heated cylinder diameter.

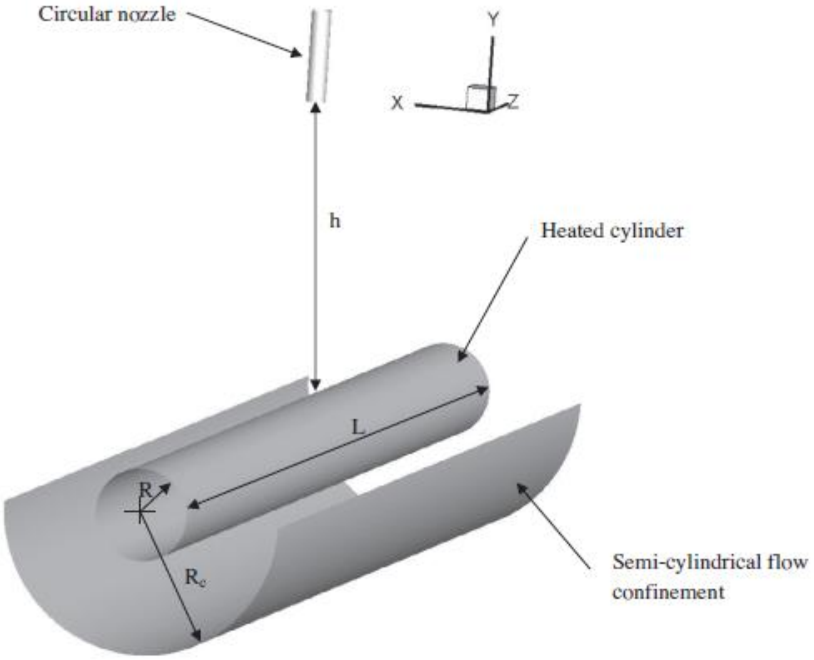

Figure 3.1. Geometry of Validation Case [40]

For the validation, a model with the dimensions shown in Figure 3.2 is built. The dimensions are determined with the help of the non-dimensional parameters stated in [40].

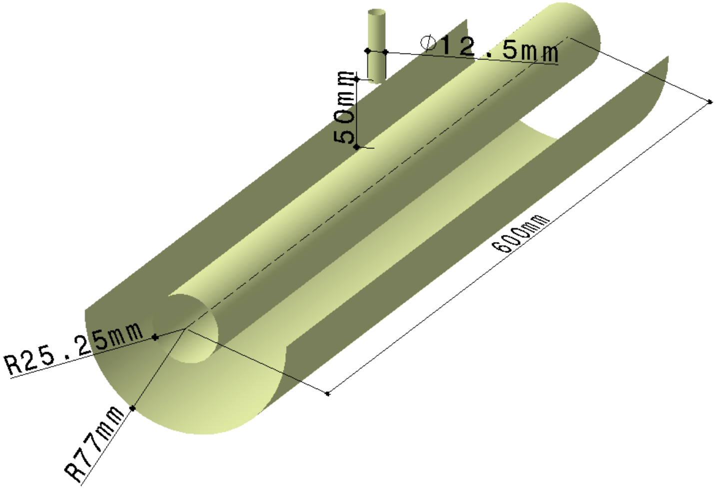

Figure 3.2. Dimensions of Validation Model

The computational domain used for validation can be seen in Figure 3.3.

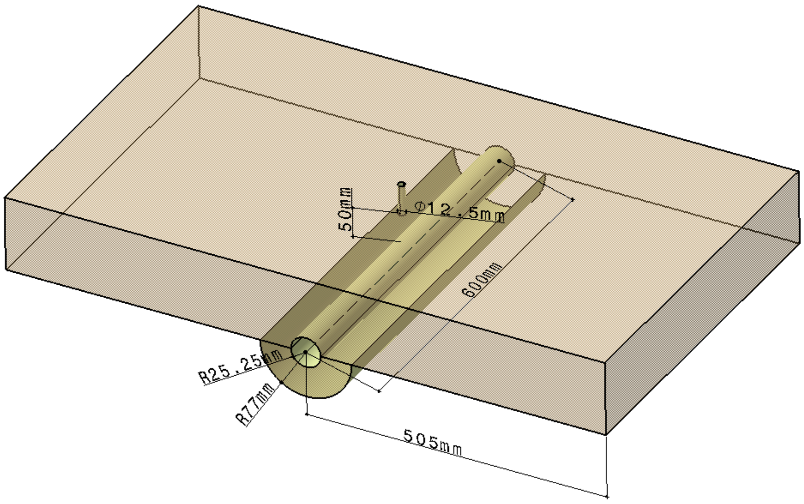

Figure 3.3. Computational Domain Used in Validation

A mesh consisting of 3.5 million cells is used for the analysis. Fluent Release 18.1 [38] is used for meshing. Firstly a surface mesh consisting of triangular elements is created. The cell sizes are given in Table 3.1. The stagnation zone where the air jet impinges on the cylinder wall is refined since complex flow patterns are expected in this region.

Table 3.1. *Validation Case Surface Mesh Cell Size*

Zone Name	*Cell Size*
Heated Cylinder	1.3 mm
Semi Cylinder Confinement	1.3 mm
Stagnation Zone on Heated Cylinder	0.5 mm
Jet Exit	0.5 mm
Computational Domain Walls	6.0 mm

After the generation of the surface mesh, the volume mesh is generated. Fifteen layers of prisms are used at the walls to capture the boundary layer. The first layer thickness is 0.035 mm and the prism layer growth rate is 1.2.

The details of the mesh used in the analysis can be seen in Figure 3.4. The stagnation zone is refined using the curves created by uniting the edges of the cells at this region. i.e. a separate surface is not created to apply refinement at this region to ease the process.

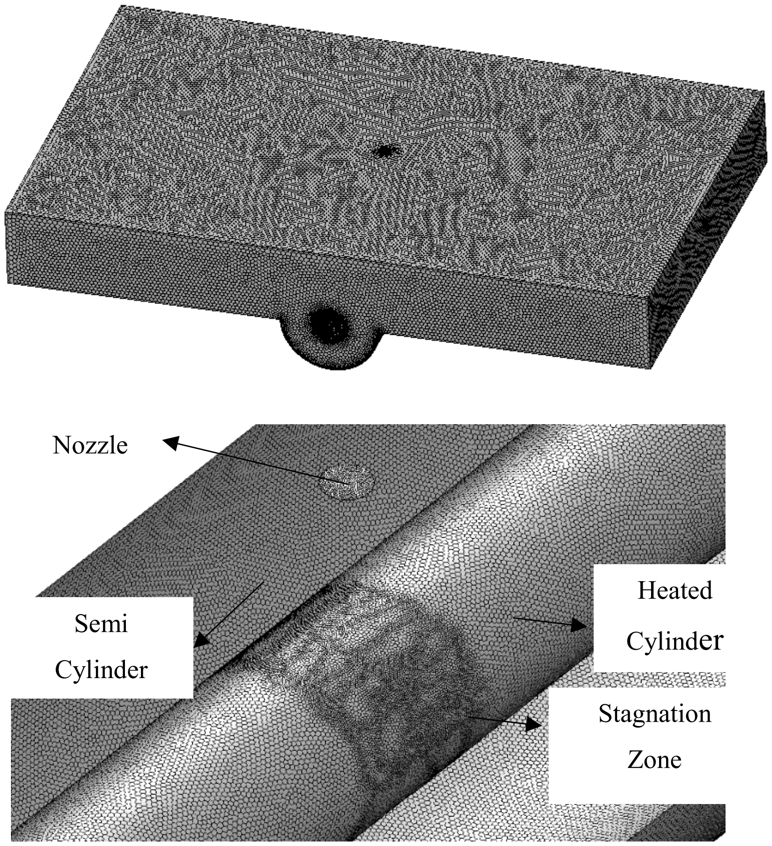

Figure 3.4. Details of Mesh Used in Validation Analysis

The boundary conditions applied are given in Table 3.2.

Table 3.2. *Validation Case Boundary Conditions*

Zone Name	*Boundary Condition*
Heated Cylinder	Wall
Semi Cylinder Confinement	Wall
Jet Exit	Velocity Inlet
Computational Domain Walls	Pressure Outlet

In addition, a uniform heat flux of 1050.527 W/m^2 is applied to the heated cylinder. On the other hand, the wall of semi-cylinder confinement is adiabatic. Temperature of the air at the nozzle exit is 300 K and a fully-developed turbulent velocity profile is applied here.

In order to determine the velocity profile, a separate CFD analysis is carried out. The model is obtained by extruding cross-section of the nozzle 1037.5 mm in a direction normal to the exit plane, which forms a straight pipe.

Wall condition is applied at the pipe walls. A pressure outlet condition is applied at the exit and the mass flow rate inlet boundary condition with a value of 0.00181 kg/s is applied at the inlet. Test data is available for the Reynolds numbers of 10000, 15000, 20000 and 25000. For validation, the mass flow rate corresponding to a Reynolds number of 10000 is used. The Reynolds number is calculated as given in Eq.(44).

$$Re=\frac{4\dot{m}}{\pi d\mu} \tag{44}$$

where $\dot{m}$ is the mass flow rate in kg/s, d is the diameter of the nozzle exit in m and μ is the dynamic viscosity in Ns/m^2.

Since the only interest is determining the velocity profile, the energy equation is not solved and no thermal boundary conditions are required for this case. Additionally, the material properties given in Table 3.3 are used for air [41].

Table 3.3. *Material Properties*

Density	*Dynamic Viscosity*
1.174 kg/m^3	1.789x10-5 Ns/m^2

The model used to obtain fully developed turbulent velocity profile can be seen in Figure 3.5. In addition, the velocity profiles at three different locations along the pipe are shown. These three locations are 40mm, 110mm and 180mm away from the exit. There are no significant changes between these profiles, meaning that the length of the straight pipe is long enough so that a fully-developed turbulent flow could be achieved at the exit and the velocity profile obtained from this analysis could be used.

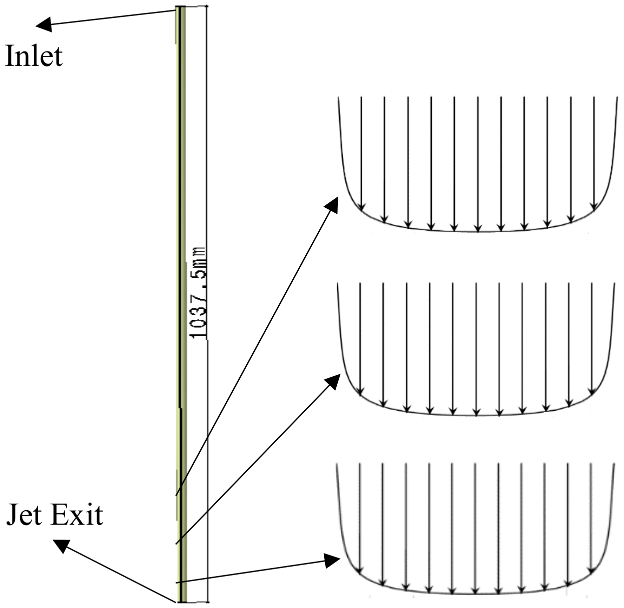

Figure 3.5. Model Used to Determine Fully Develop Turbulent Velocity Profile

Radiative heat transfer is also considered during the analysis. A surface-to-surface radiative heat transfer model is used. The emissivity of the heated cylinder surface is 0.17 and the semi-cylinder confinement is treated as a black body [40].

As mentioned above, the experimental results are represented by the utilization of three non-dimensional parameters in [40]. These parameters are the Reynolds number of the jet, the ratio of the heated cylinder diameter to the confinement diameter and the ratio of the nozzle-heated cylinder distance to the heated cylinder diameter. The values of these non-dimensional parameters are shown in Table 3.4.

Table 3.4. *Non-Dimensional Parameters of Validation Model*

Non-Dimensional Parameter	*Values*
Reynolds number of free jet	10000
Ratio of heated cylinder diameter to confinement diameter	3.05
Ratio of distance between nozzle and heated cylinder to heated cylinder diameter	4.0

The change of the wall temperature along the cylinder is shown in the axial direction, z, normalized by the heated cylinder diameter, D_{heated} in Figure 3.6. The origin is located at the symmetry plane of the cylinder. The variation in the temperature is shown at several angles around the cylinder, where 0° corresponds to the jet stagnation point at the top of the cylinder and 180° is the bottom. The CFD results are plotted at the same locations where the measurements are available.

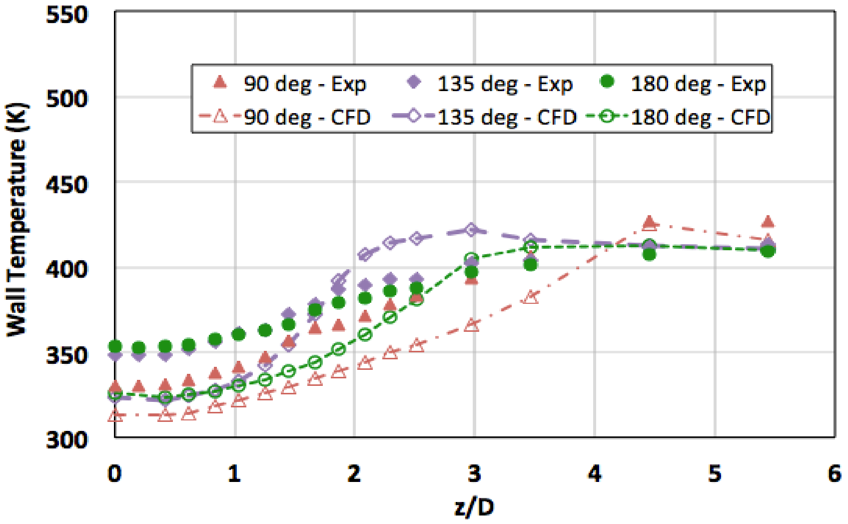

Figure 3.6. Comparison of Local Wall Temperatures Obtained from Experimental Data and Numerical Analysis (Experimental Data from Ref. [40])

It is observed that the wall temperature errors are high in the regions close to the stagnation zone. This issue is also observed in [40]. The errors are higher for the 135° and 180° cases than those for the 90° case. Despite those differences, however, the computational results show reasonable agreement with the data. This agreement improves further along the remaining of the cylinder surface, while the maximum difference between the predictions and the data is found near the stagnation point for the 180° angle. Despite the relatively high differences between the CFD results and the experimental measurements in the first half of the axial direction, it is observed that the CFD analyses are able to capture the general trends of the temperature measurements.

A mesh sensitivity study was also performed for the validation case. The mesh with the cell sizes given in Table 3.1 has 3.5 million cells. Results are obtained for a mesh containing 1.8 million cells, as well. Local wall temperature values at 90°, 135° and 180° obtained with this two meshes are then compared. It is observed that the average difference between the results is only 0.5% and the maximum difference is 2.8% as observed around the middle part of the cylinder for the 135° case. With this, it is concluded that the results are insensitive to the mesh size and the errors between the experimental and numerical results could not be significantly decreased by solving the validation case with finer meshes.

3.4. Analyses of Design Points

In this section, the details about the analyses carried out for the DPs are given.

3.4.1. Boundary Conditions and Material Properties

The boundary conditions applied are given in Table 3.5.

Table 3.5. *Boundary Condition Types*

Zone Name	*Boundary Condition*
Fan	Mass Flow Rate Inlet
Exhaust	Pressure Outlet
Skin	Wall
Floor	Wall
Frame	Wall

For the fan, the mass flow rate values obtained by the design-of-experiment study are applied. The temperature of the air is at 323.15K, since the fan directly supplies the outside air into the interior of the bay. In order to represent the exhaust, a pressure outlet boundary condition is used with a static pressure value of 101.325 kPa. For the skin, the no-slip boundary condition and convective heat transfer boundary condition are applied. Two inputs are required to apply this boundary condition. These are the outside air temperature and the convective heat transfer coefficient by the outer surface of the skin. The analyses are carried out for an outside air temperature of 323.15 K and the convective heat transfer coefficient is calculated by Eq.(45) [34].

$$h_{outside} = 11.35 + 1.781\, V_{wind} \qquad (45)$$

where $h_{outside}$ is the convective heat transfer coefficient by the outer surface of the skin and V_{wind} is the outside wind velocity.

The wind velocity is assumed to be 0. As a result, the convective heat transfer coefficient becomes 11.35 W/m^{2}K for the skin.

Additionally skin has a thickness and heat is transferred across the skin by conduction. The thickness of the skin is 1 mm. This thickness is not meshed, since it would increase the mesh size significantly. Instead, the conductive heat transfer is considered by a thin-wall assumption analytically. Due to the small thickness value, the conductive heat transfer is assumed to be only in the direction normal to the surface. During the calculations, the thermal resistance of the skin is used to determine the temperature of the outer and inner wall surfaces of the skin [38]. The thermal resistance is defined as

${l}/_{k}$, where l is the thickness of the skin and k is the thermal conductivity of the wall material.

The boundary condition settings for the floor are the same as the ones for the skin. In the analyses, the nose avionics bay of a rotorcraft with retractable nose landing gears is used. The analyses are carried out for the ground case, since this is the worst case in terms of avionics cooling. Since the rotorcraft is on the ground, the landing gears are extracted and the landing gear doors are open. The nose landing gear is usually located under the nose avionics bay and since the landing gear doors are open, the outer surface of the avionics bay floor is exposed to the outside air directly. Therefore, the convective heat transfer boundary condition is applied to the floor as well. In addition, floor has a 1 mm thickness. The conduction across the floor is also handled with the thin-wall assumption.

On the other hand, the adiabatic boundary condition is applied to the frame. The frame is located between the nose avionics bay and the cockpit. The average air temperature values inside the bay are expected to be around 343.15 K. The temperature values inside the cockpit is much less than this value, since cockpit is an occupied zone. Therefore, heat is transferred from the nose avionics bay to the cockpit during normal operation and has a cooling effect on the avionics bay. However, in this study the frame is assumed to be adiabatic, since there is no certain information about the temperature inside the cockpit. This assumption is a conservative one in terms of avionics cooling.

Next boundary condition is the heat load of the avionics equipment. Avionics heat loads could be represented by two different boundary condition types. The first one is by applying the heat-flux boundary condition to the avionics surface. The second one is to define a volumetric heat source. In order to define a volumetric heat source, the avionics equipment needs to be meshed and the energy equations must be solved inside the avionics equipment. This causes an increase in the mesh size. On the other hand, if the heat-flux boundary condition is applied, this imposes that the same amount of heat is transferred from each surface of the avionics equipment independent of the flow field around. For example, an avionics could be located such that one of its faces is exposed to the high-speed air from the fan, while the other faces are not. Normally, a higher amount of heat is transferred through the face exposed to a high-speed flow compared to the other ones. If the volumetric heat source boundary condition is applied, this effect can be accounted for. Therefore, the heat load of the avionics equipment are represented with the volumetric heat source method with the values given in Table 3.6.

Table 3.6. *Volumetric Heat Generation Values*

Avionics Equipment	*Volumetric Heat Generation (W/m3)*
Avionics 1	12904.1
Avionics 2	15474.5
Avionics 3	28274.76
Avionics 4	33835.17
Avionics 5	15727.53
Avionics 6	18803.07
Avionics 7	23104.35
Avionics 8	14040.48
Avionics 9	36903.01
Avionics 10	29101.93
Avionics 11	14786.22

In addition to the included gravity, the density of the air must be varying as a function of temperature to account for natural convection as explained before. The thermal conductivity and dynamic viscosity of air are assumed to be constant with values of 0.0295 W/m K and 2.049×10^{-5} kg/m s, respectively [41].

Solid material properties are given in Table 3.7. The materials of the skin, floor and frame are carbon fiber composite and the avionics are made of aluminum. The surface emissivity values, which are used during the radiative heat transfer calculations, are also shown in Table 3.7.

Table 3.7. *Solid Material Properties [41]*

Material	*Density (kg/m3)*	*Specific Heat (J/kg-K)*	*Thermal Conductivity (W/m-K)*	*Surface Emissivity*
Composite	1400	935	11.1	0.80
Aluminum	2719	871	202.4	0.78

3.4.2. Mesh Sensitivity

Three different polyhedral meshes consisting of approximately 1, 1.9 and 4 million cells is used for the analysis. The surface mesh cell sizes used to generate these three meshes are given in Table 3.8.

Fifteen layers of prisms are generated near the walls to solve the boundary layer accurately. The first layer thickness is 0.07 mm and the growth rate of the prism layers is 1.15. The prism layer parameters are common for all three meshes.

As mentioned in the previous section, a CFD analysis for each DP is performed. Therefore, one hundred and seventy seven CFD analyses are run in total. It is not feasible to perform a mesh sensitivity study for each DP. Hence, the mesh sensitivity study is performed only for the case that is used in the determination of the upper limit of the range of the mass flow rate. For this case, higher gradients in the flow field is expected due to higher mass flow rate value. The geometry of the case used for the mesh sensitivity study is shown in Figure 2.6. The fan mass flow rate value is 0.055 kg/s as mentioned previously.

Table 3.8. *Surface Mesh Cell Size Used to Generate Meshes With 1, 1.9 and 4 Million Cells*

Zone Name	*Coarse Mesh Cell Sizes*	*Medium Mesh Cell Sizes*	*Fine Mesh Cell Sizes*
Skin, Floor and Frame	12.95 mm	9.5 mm	6.8 mm
Avionics Located on Floor (Avionics 2, Avionics 5, Avionics 6, Avionics 7, Avionics 8)	12.95 mm	9.5 mm	6.8 mm
Avionics Located on Rack (Avionics 1, Avionics 3, Avionics 4, Avionics 9, Avionics 10, Avionics 11)	10.8 mm	8 mm	5.7 mm
Fan, Exhaust	6.7 mm	5 mm	4 mm

In order to determine whether the results become insensitive to the mesh size, the average avionics surface temperature values are used. The results obtained with coarse, medium and fines meshes are shown in Table 3.9. The difference between the coarse and the medium mesh is 0.66 K on average for all equipment; this difference is reduced to 0.33 K between the medium and the fine mesh. These differences correspond to 0.2% and 0.1%, respectively. In addition, it is observed that the average surface temperature differences between coarse and medium mesh is a little high for Avionics 10 with a difference of 1.5 %. Such high difference is not observed between the medium and fine mesh results. Hence, the medium mesh is used for the DP analyses. The change in the average avionics surface temperature results are also shown graphically in Figure 3.7.

Table 3.9. *Average Avionics Surface Temperature Results Obtained With Three Meshes*

Avionics	*Coarse Mesh (K)*	*Medium Mesh (K)*	*Fine Mesh (K)*
Avionics 1	357.0	357.7	357.4
Avionics 2	352.0	351.7	351.4
Avionics 3	382.8	381.4	380.3
Avionics 4	378.8	378.3	377.3
Avionics 5	372.0	371.4	371.4
Avionics 6	378.2	378.2	378.3
Avionics 7	380.8	381.6	381.3
Avionics 8	370.4	370.0	370.3
Avionics 9	385.5	385.2	384.7
Avionics 10	379.2	377.6	377.0
Avionics 11	353.3	352.9	352.2

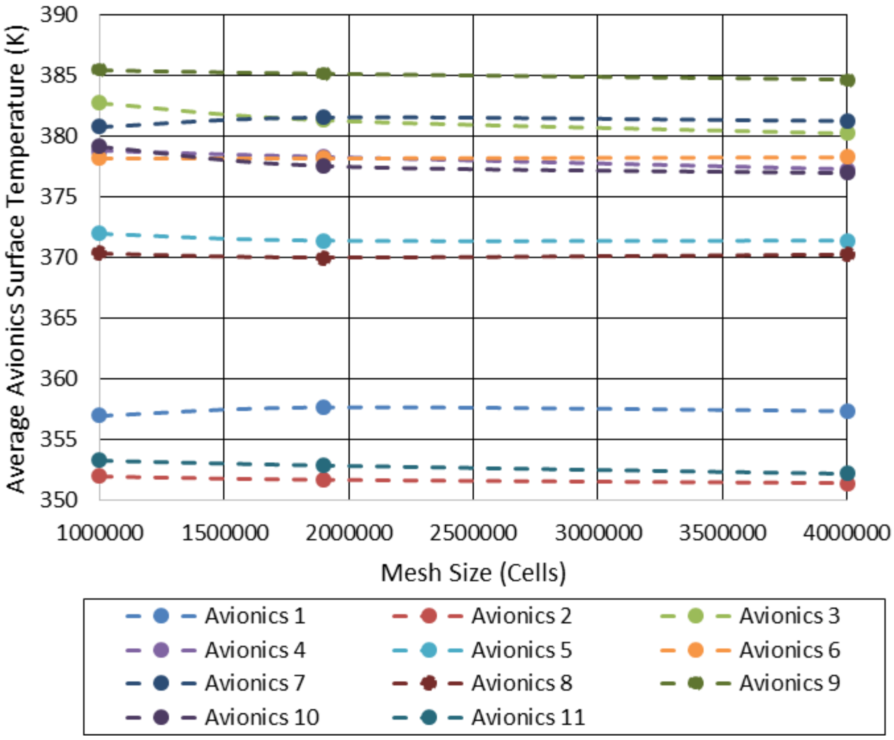

Figure 3.7. Change in Average Avionics Surface Temperature Results With Mesh Size

The details of the medium mesh surface cells can be seen in Figure 3.8 and Figure 3.9.

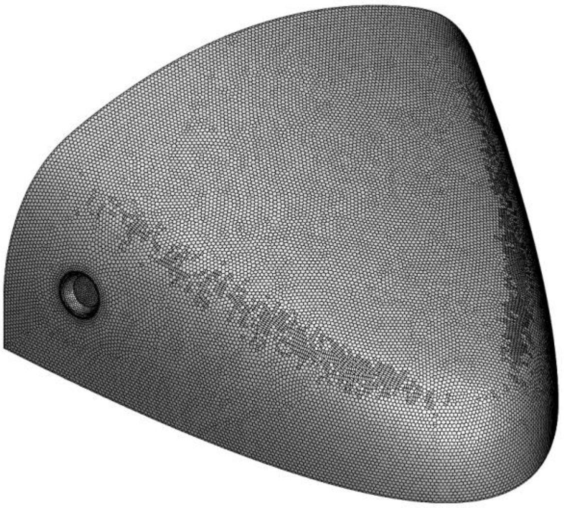

Figure 3.8. Details of Medium Mesh Surface Cells Over Skin and Fan

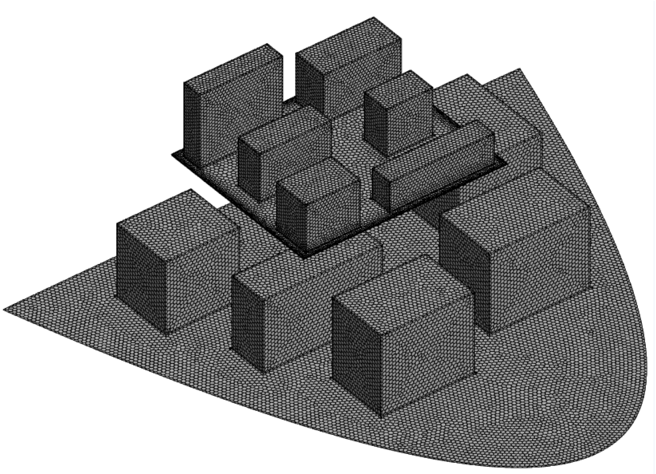

Figure 3.9. Details of Medium Mesh Surface Cells Over Avionics, Rack and Floor

A close-up view of the medium mesh volume cells are shown in Figure 3.10 on a horizontal plane with a focus on the prism layer. The fluid cells are colored in light gray, whereas the solid cells are given in dark gray.

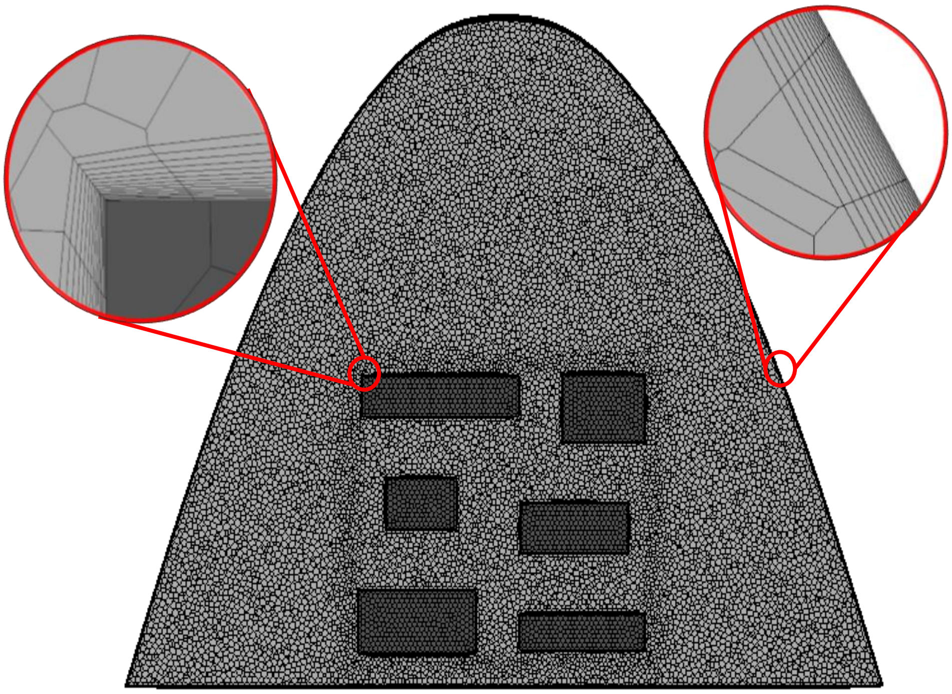

Figure 3.10. Details of Medium Mesh Volume Cells

To quantify the numerical uncertainty, the Richardson extrapolation [42] is used. The spatial discretization error is calculated via the Grid Convergence Index (GCI) defined by Eq.(46).

$$GCI = F_S \frac{|\xi|}{r^p - 1} \tag{46}$$

where F_S is the factor of safety with the recommended conservative value of 3 by Roache [43], and p is the order of accuracy which is taken as the theoretical value of 2, due to the use of the second order upwind scheme in the computations. The refinement factor, r, and the relative error between the fine and medium meshes, ξ, are given in Eq.(47) and Eq.(48)as follows:

$$r = \left(\frac{N_{fine}}{N_{medium}}\right)^{\frac{1}{D}} \tag{47}$$

$$\xi = \frac{f_{medium} - f_{fine}}{f_{fine}} \tag{48}$$

Here, f represents the predicted values by the medium and fine meshes, and N is the number of nodes in those meshes. The medium and fine meshes mentioned above have 6.1 million and 13.8 million nodes, respectively, giving a value of 1.31, which satisfies the criteria given in [42]. D is the dimensionality of the study, and hence, is taken as 3 in the above calculations. The GCI is calculated for the avionics surface temperature. It is found to be 0.53% on average, and less than 1.12% for all equipment in the avionics bay, suggesting a small discretization error.

Next, y+ values are checked to determine whether the first layer thickness of the prism layer is selected accurately or not. Since, enhanced wall treatment is used, y+ values of the first prism layer cells must be below 1. The y+ contours for the medium mesh are shown in Figure 3.11. The values slightly higher than 1 correspond to those local areas where the jet of the fan impinges on. A relatively higher y+ value is seen on the corner of avionics equipment 2, as this equipment sits in the line of the jet.

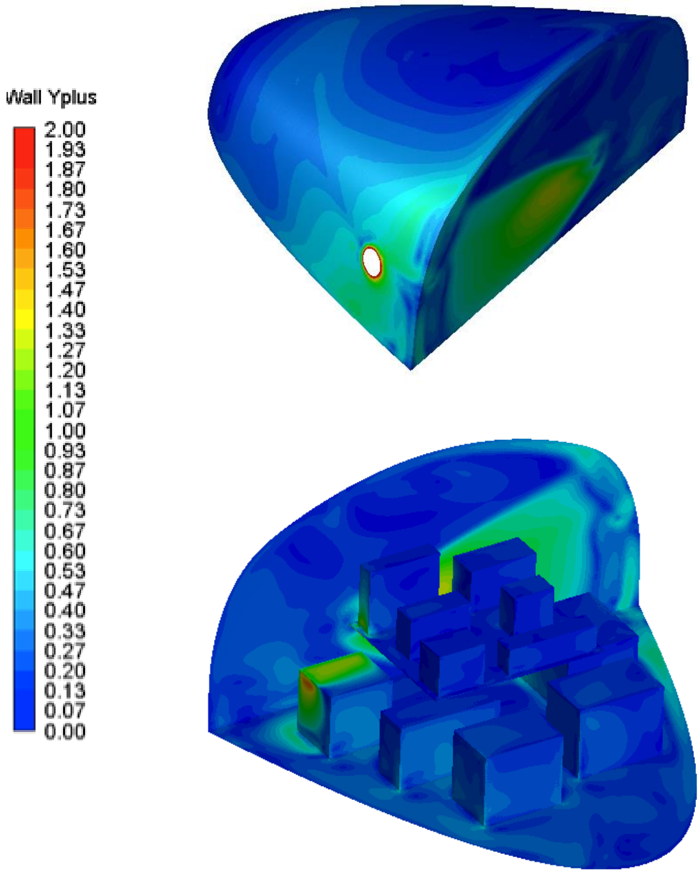

Figure 3.11. y+ Contours

The fluid temperature contours at two planes parallel to the floor are shown in Figure 3.12. The first column of contours is from a plane 150 mm offset to the floor and the second column of contours is from a plane 300 mm offset to the floor. Generally, there are no significant differences between the meshes at both planes. The energy equation is also solved inside the avionics equipment, as stated above.

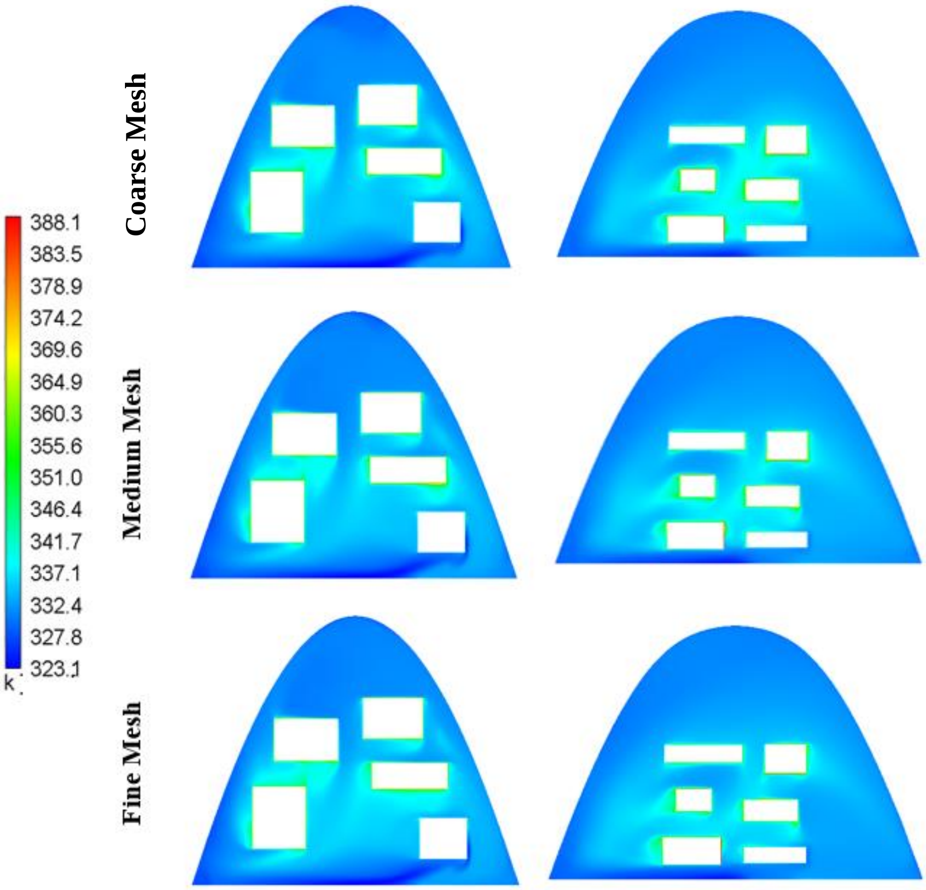

Figure 3.12. Fluid Temperature Contours for Three Meshes

In Figure 3.13, the solid temperature contours inside avionics 9 are shown at two of the equipment mid sections. Avionics 9 is selected, since this equipment has the highest volumetric heat generation value, as seen in Table 3.6. Therefore, higher temperature gradients are expected inside avionics 9. When the contours are investigated, it is seen that the temperature gradients are small and no significant differences are observed between the coarse, medium and fine meshes. The color changes between the coarse, medium and fine mesh contours are due to the fact that the upper and lower limits of the color map are very close to each other. Therefore, even small changes in the temperature magnitudes cause large color changes. It can be observed that the differences in the local temperature magnitudes are less than 1K.

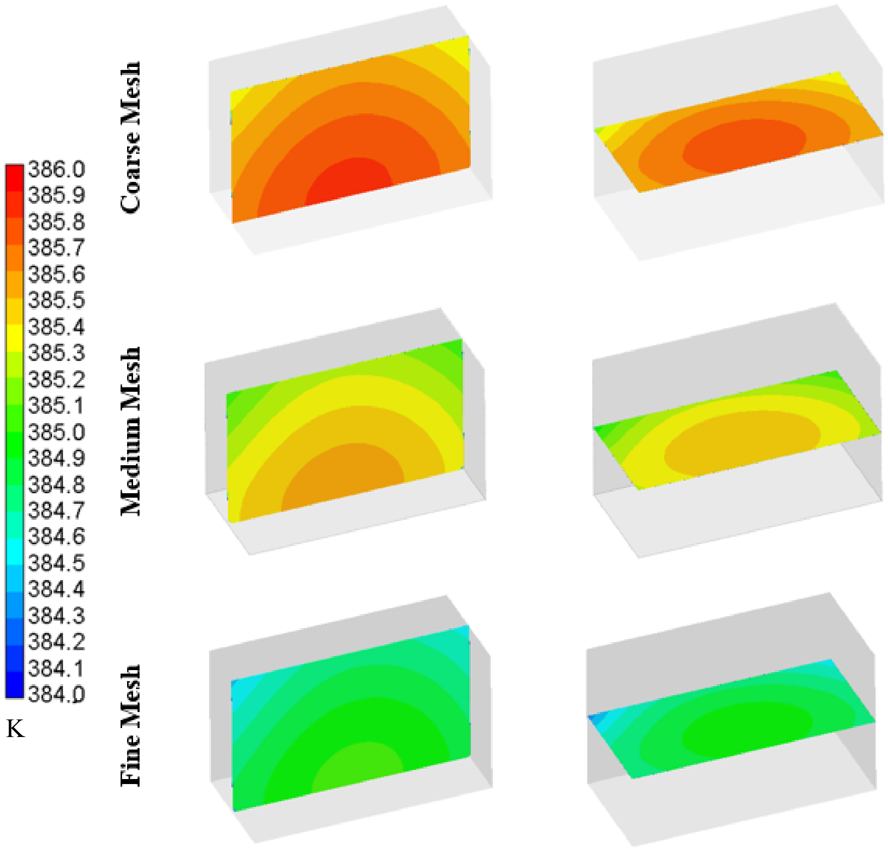

Figure 3.13. Solid Temperature Contours for Three Meshes for Avionics 9

3.4.3. Convergence Check

In order to check whether the results have converged or not, the residuals are monitored. The change of residuals for the analysis performed with the medium mesh is shown in Figure 3.14. It is suggested that the energy equation residuals should be lower than 10^{-6} and all other residuals should be lower than 10^{-4} [38]. In this study, the residuals drop below these suggested values.

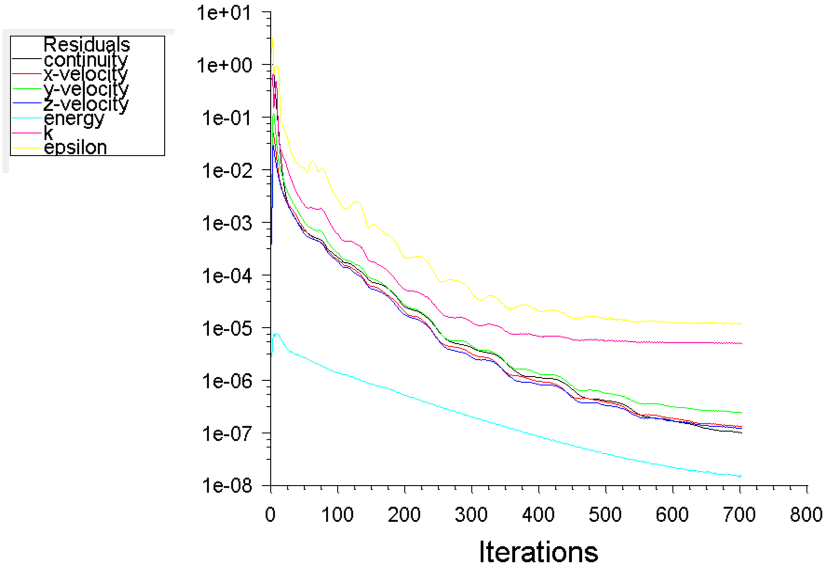

Figure 3.14. Change of Residuals for Analysis Performed With Medium Mesh

Some flow field parameters of interest are also monitored to check the convergence of the computations. Firstly, three points are created inside the bay and the velocity magnitude parameters are monitored. The change in velocity magnitudes is given in Figure 3.15. The approximate locations of these three points are shown in Figure 3.16.

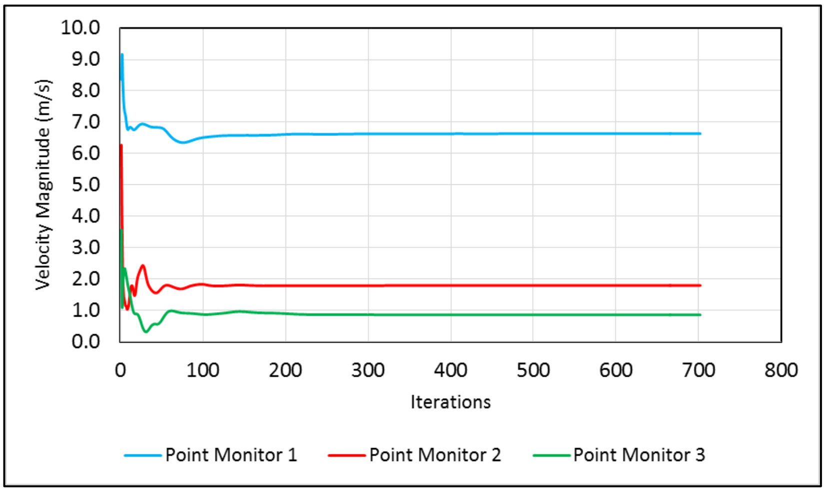

Figure 3.15. Velocity Magnitude Point Monitors

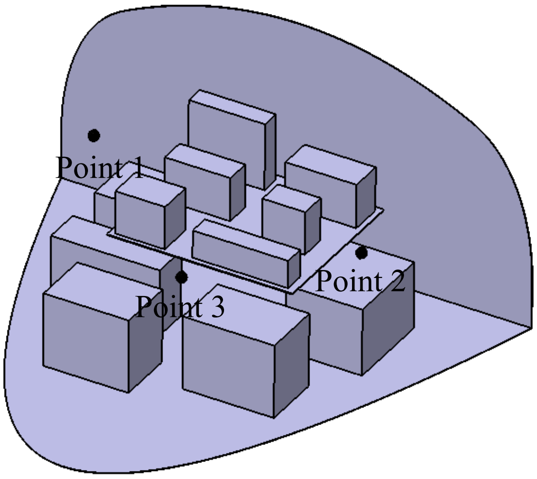

Figure 3.16. Approximate Locations of Point Monitors

The volume-averaged air temperature inside the nose avionics bay and the average avionics surface temperatures are also monitored. In Figure 3.17, the change in the volume-averaged air temperature can be seen. The variation in the avionics average surface temperatures with iterations is shown in Figure 3.18 for all eleven avionics. It is observed that all monitored parameters smoothly converge around a value.

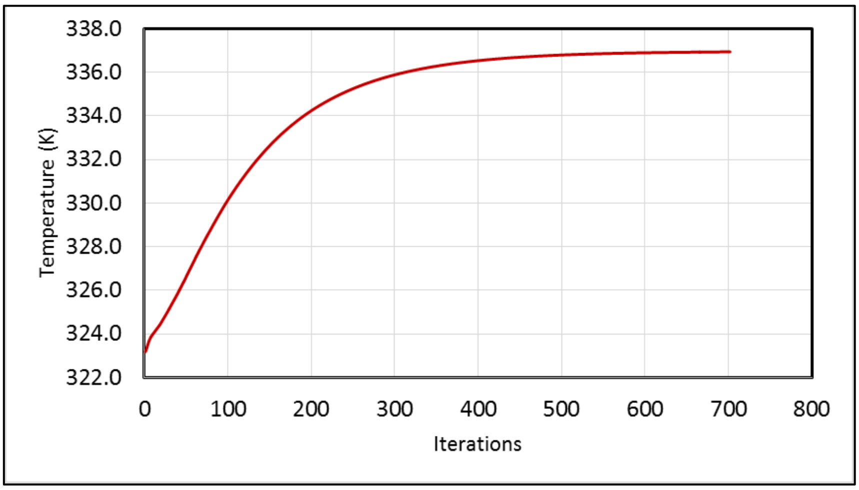

Figure 3.17. Volume Averaged Air Temperature

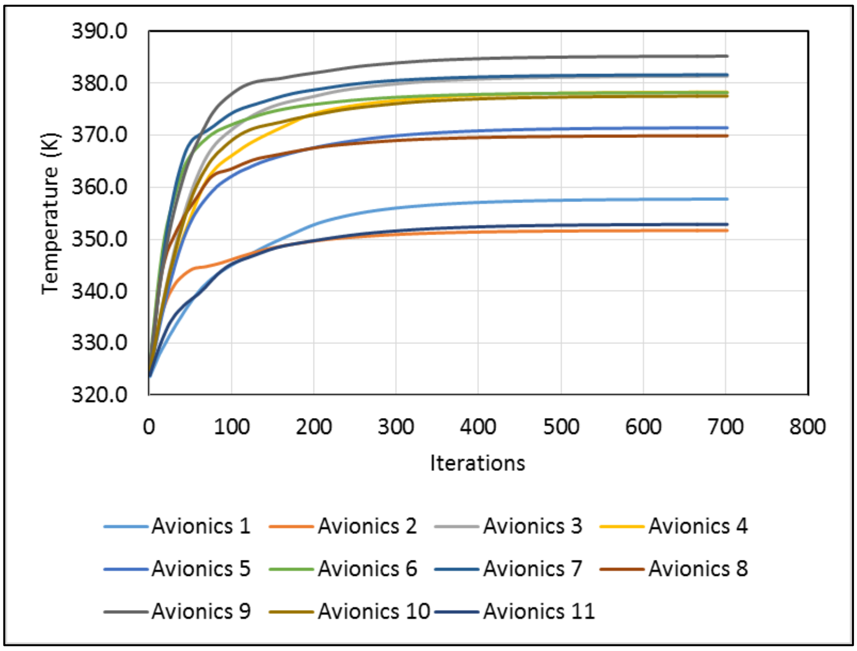

Figure 3.18. Avionics Average Surface Temperatures

CHAPTER 4

PREDICTION FUNCTION

In this chapter, details on the prediction function are explained. Two different prediction functions are built with two different methods. The first prediction function is built by using the Gaussian Process Regression method and the second one is built by using the Artificial Neural Networks. The accuracy of these two prediction functions are compared by utilization of test cases and one of them is selected to be used with the optimization algorithm to determine the optimum fan and exhaust locations.

4.1. Gaussian Process Regression

A Gaussian Process is a collection of a finite number of random variables, which has a multivariate Gaussian distribution as a joint probability density function [44]. Mathematical representation of a Gaussian Process can be seen in Eq.(49). The random variables are used to represent the avionics average surface temperature values corresponding to different input variable sets.

$$f(\boldsymbol{x}) \sim GP(m(\boldsymbol{x}), k(\boldsymbol{x}, \boldsymbol{x}')) \tag{49}$$

In this equation, $\boldsymbol{x}$ is the input variables vector consisting of the fan mass flow rate, fan x coordinate, fan y coordinate, exhaust x coordinate and exhaust y coordinate, $m(\boldsymbol{x})$ represents the mean value of the random avionics average surface temperature for $\boldsymbol{x}$, and $k(\boldsymbol{x},\boldsymbol{x}')$ is the variance-covariance matrix.

As it can be seen in Eq.(49), two parameters must be determined for the Gaussian Process. These are the mean values of the random variables and the variance-covariance matrix. The variance-covariance matrix is used to define the shape of the multivariate Gaussian distribution. The diagonal elements of the matrix stores the variance of each random variable and other elements store the covariance of random variables with each other.

In order to understand the effects of the mean function and the variance-covariance matrix, consider a Gaussian Process that consists of two random variables, namely y1 and y2. In Figure 4.1, the probability density distribution of these two random variables is shown. As it can be seen, the most probable values of random variables y1 and y2 are (0,0), as the probability distribution function owns the highest value at (0,0) point. For other y1 and y2 value pairs, the probability decreases. The mean values are also obtained by averaging the possible values of y1 and y2 and the mean values are (0,0) for this Gaussian Process.

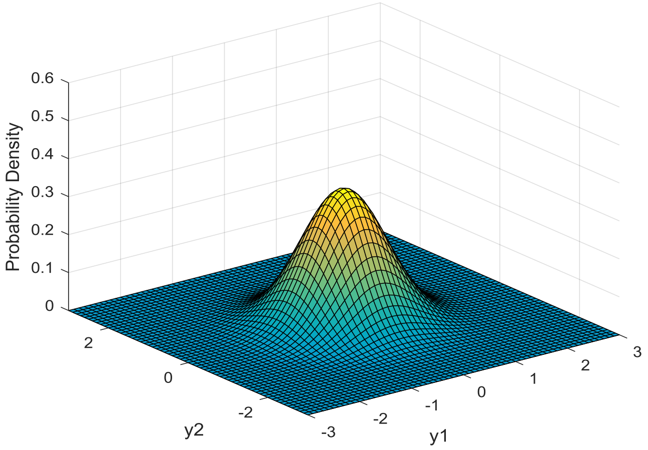

Figure 4.1. Probability Density Distribution of Random Variables y1 and y2

As the mean values of these two random variables are changed, the shape of the probability density functions does not change, but, the function is repositioned such that the point with the highest probability changes. In Figure 4.2, a new probability density distribution for y1 and y2 is shown for mean values of (1,2). Here, the point with the highest probability corresponds to (1,2). The variance-covariance matrix of the multivariate Gaussian distribution shown in Figure 4.1 and Figure 4.2 is a 2 by 2 matrix, since the Gaussian Process consists of two random variables with the values: $\begin{bmatrix} 0.45 & 0 \\ 0 & 0.45 \end{bmatrix}$.

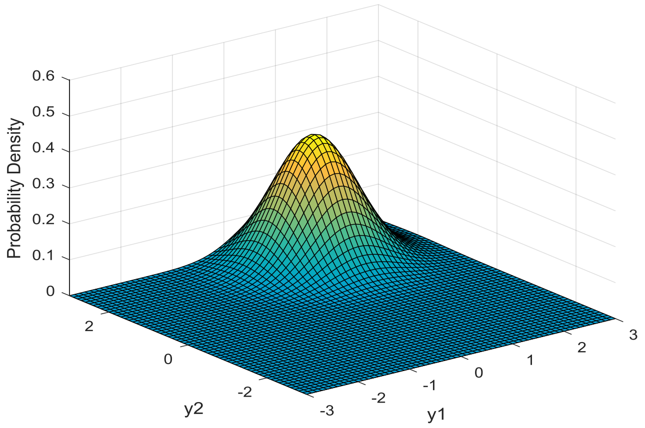

Figure 4.2. Probability Density Distribution of Random Variables y1 and y2 with New Mean Values

When the variance-covariance matrix is modified as $\begin{bmatrix} 0.1 & 0 \\ 0 & 0.8 \end{bmatrix}$, the probability density function is reshaped as shown in Figure 4.3. The mean values are kept at (0,0).

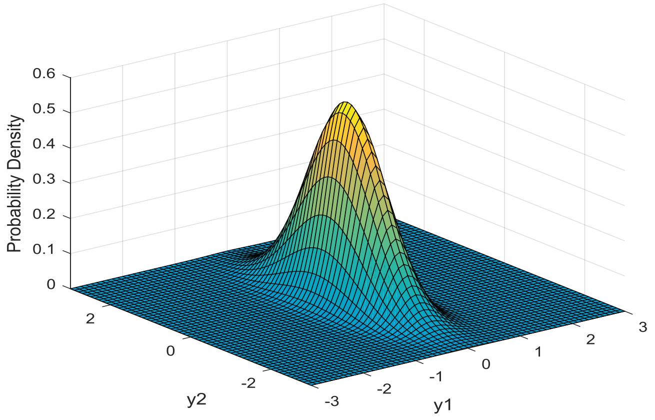

Figure 4.3. Probability Density Distribution of Random Variables y1 and y2 with New Variance Values

As it can be seen, it becomes more probable that y1 gets values around its mean value 0. This is due to the small variance of y1. Whereas, probability density distribution of y2 is more scattered due to the high variance.

Finally, the shape of the probability density function becomes as shown in Figure 4.4 when the values of the off-diagonal elements are changed as $\begin{bmatrix} 0.1 & -0.3 \\ -0.3 & 0.8 \end{bmatrix}$.

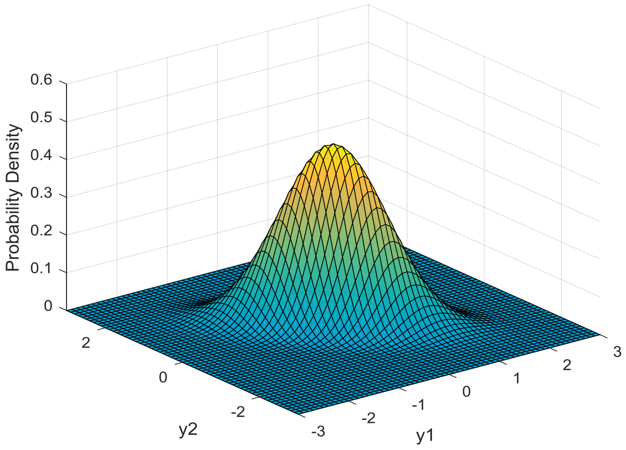

Figure 4.4. Probability Density Distribution of Random Variables y1 and y2 with New Covariance Values

In this new shape, the probability density function is stretched in the diagonal direction. This means that y1 and y2 are correlated with each other. The Variance-Covariance matrix is a symmetric matrix. The first off-diagonal element shows the covariance of y1 with y2 and the second off-diagonal element shown the covariance of y2 with y1. These two values must be the same. This is also valid for variance-covariance matrixes of Gaussian Processes with higher number of random variables.

For the Gaussian Process Regression, the Matlab Statistics and Machine Learning Toolbox is used. Firstly, a Gaussian Process is created. The number of the random variables is equal to the number of the DPs and one extra random variable. The additional random variable is used to predicted the avionics surface temperatures for the desired new input parameter set of the fan mass flow rate, fan x and y coordinates, and exhaust x and y coordinates. The mean values of the random variables and the variance-covariance matrix of the multivariate Gaussian distribution are user defined. A prediction function capable of predicting the average surface temperature of only one avionics at a time could be created with Gaussian Process Regression. Therefore, Gaussian Process Regression is performed eleven times to create eleven prediction functions, each of which predicts the average surface temperature of a separate avionics.

Matlab has some predefined functions to determine the random variable mean values and the variance-covariance matrix. The functions shown in Table 4.1 are used for the eleven prediction functions and are determined by trial and error.

Table 4.1. *Function to Define Mean Values and Variance-Covariance Matrix*

Avionics Equipment	*Mean Value Function*	*Variance-Covariance Function*
Avionics 1	Pure Quadratic Polynomial	ARD Matern 3/2
Avionics 2	Pure Quadratic Polynomial	ARD Squared Exponential
Avionics 3	Pure Quadratic Polynomial	Squared Exponential
Avionics 4	Linear Polynomial	Matern 5/2
Avionics 5	Pure Quadratic Polynomial	Matern 3/2
Avionics 6	Pure Quadratic Polynomial	ARD Matern 3/2
Avionics 7	Linear Polynomial	ARD Matern 3/2
Avionics 8	Linear Polynomial	ARD Matern 3/2
Avionics 9	Pure Quadratic Polynomial	Squared Exponential
Avionics 10	Pure Quadratic Polynomial	ARD Squared Exponential
Avionics 11	Pure Quadratic Polynomial	ARD Matern 3/2

Three additional test points are created and CFD analyses are run for these points. Results are obtained with Gaussian Process Regression for these three test points as well. Then, the results are compared and the selected mean value and variance-covariance functions are changed to determine the ones giving the closest results to the CFD results.

For the mean values, a multi-variate polynomial is fit to the avionics surface temperature data obtained by the CFD analyses of the DPs. This polynomial is evaluated at the input parameter sets of one hundred and seventy seven (177) DPs and at the input parameter set of the additional random variable. The values obtained are the mean values of the Gaussian Process. The linear polynomial is defined by Eq.(50) and the pure quadratic polynomial is defined by Eq.(51).

$$m(\boldsymbol{x}) = \sum_{i=1}^{5} b_i x_i + D \tag{50}$$

$$m(\boldsymbol{x}) = \sum_{i=1}^{5} b_i x_i + \sum_{i=1}^{5} c_i {x_i}^2 + D \tag{51}$$

where b's and c's are the coefficients of the polynomial, $\boldsymbol{x}$'s are the five input parameters (i.e fan mass flow rate, fan x coordinate, fan y coordinate, exhaust x coordinate and exhaust y coordinate) and D is a constant.

Regarding the Variance-Covariance matrix, the diagonal elements are determined by Matlab during the Gaussian Process Regression and the function given in Table 4.1 are used to determine the off-diagonal elements. Squared Exponential, Matern 3/2 and Matern 5/2 function are given in Eq.(52), Eq.(53) and Eq.(54), respectively. [45]

$$(x_i, x_j) = {\sigma_f}^2 exp\left[-\frac{1}{2}\frac{r^2}{{\sigma_l}^2}\right] \tag{52}$$

$$k(x_i, x_j) = {\sigma_f}^2 \left[1 + \frac{\sqrt{3}r}{\sigma_l}\right] exp\left[-\frac{\sqrt{3}r}{\sigma_l}\right] \tag{53}$$

$$k(x_i, x_j) = \sigma_f{}^2 \left[1 + \frac{\sqrt{5}r}{\sigma_l} + \frac{5r^2}{3\sigma_l{}^2}\right] exp\left[-\frac{\sqrt{5}r}{\sigma_l}\right] \tag{54}$$

Here σ_f is the signal standard deviation and σ_l is the characteristic length scale. σ_f and σ_l are the parameters of the functions and are determined by Matlab during the Gaussian Process Regression. r is the distance between the input variable sets of two random variables in the input parameter domain and is calculated as in Eq.(55).

$$r = \sqrt{\sum_{i=1}^{5} (x_{mi} - x_{ni})^2} \tag{55}$$

x_m and x_n are the input parameter sets of the two random variables and the subscript i is used to represent the five input parameters. The functions for ARD Squared Exponential and ARD Matern 3/2 are given in Eq.(56) and Eq.(57). [45]

$$k(x_i, x_j) = \sigma_f{}^2 exp\left[-\frac{1}{2}\sum_{i=1}^{5} \frac{(x_{mi} - x_{ni})^2}{\sigma_m{}^2}\right] \tag{56}$$

$$k(x_i, x_j) = \sigma_f{}^2 \left[1 + \sqrt{3}\sqrt{\sum_{i=1}^{5} \frac{(x_{mi} - x_{ni})^2}{\sigma_m{}^2}}\right] exp\left[-\sqrt{3}\sqrt{\sum_{i=1}^{5} \frac{(x_{mi} - x_{ni})^2}{\sigma_m{}^2}}\right] \tag{57}$$

Here σ_m is also a length scale. However, a separate length scale is used for each of the five parameters in the ARD functions. As it can be seen above, the Variance-Covariance functions uses the distance between the input parameter sets of the random variables in the parameter domain. As the two random variables gets closer, they become more correlated.

After the Gaussian Process is built, the next step is the training. While generating the Gaussian Process, the random variables are assigned to the DPs as mentioned above. The avionics surface temperatures for these random variables are treated as if those were unknown and the mean values and the probability density distributions are calculated for random variables corresponding to the DPs as well. However, the avionics surface temperature values for the random variables corresponding to the DPs are actually known. This data is used for training. The training process in the Gaussian Process Regression is basically a conditional probability calculation. Conditional probability may be described as the probability of an event to occur based on the knowledge that another event, which is dependent on the first event, has already occurred in a certain way. For the average avionics surface temperature prediction case, this could be interpreted as the conditional probability calculation for the additional random variable given that the values of the other random variables (corresponding to DPs) are actually known. After the training, a new mean and a new probability density distribution are obtained for the additional random variable. The value of this new mean is the Gaussian Process Regression prediction for the new desired input parameter set.

The training process may be explained better through an example. Imagine that there is a training set that consists of one DP only and Gaussian Process Regression is used with this training data. Therefore, A Gaussian Process consisting of two random variables is built. Now assume that the random variables are y1 and y2 from Figure 4.4 and that the Gaussian Process has a probability density distribution function that is the same as the one shown in Figure 4.4. As mentioned above, the training set has one DP and assume that this DP corresponds to y1. Since y1 is included in the training data, its actual values are known by some means such as the measurements or analyses, and the aim is to predict the value of y2 by the Gaussian Process Regression. Assume that the actual value of y1 is 1. The training of the Gaussian Process Regression is simply a conditional probability calculation. i.e. after the training a new probability density distribution for y2 is calculated given that the value of y1 is known and is equal to 1.

The initial probability density function is formed as if the actual values of both y1 and y2 were not known as given in Figure 4.4. This distribution is called the prior. After the training a new distribution for y2 is obtained and the new distribution is called the post. How the prior is used to determine the post could be graphically interpreted as getting a cut section from the prior probability density distribution function shown in

Figure 4.4 at a plane y1=1, since this is the actual value of y1. After this process, a curve is obtained for y2 similar to the one shown in Figure 4.5. This curve is the post probability density distribution. The mean of the post is equal to the value of y2 that is predicted by the Gaussian Process Regression. As it can be seen, the Gaussian Process Regression predicts y2 as -1.5 given that the value of y1 is known and equal to 1.

For the avionics cooling case, the probability density distribution function is 178 dimensional, since this is the total number of random variables. During the training, 177 cut sections are obtained at the planes determined based on the CFD results of the DPs. Then a one dimensional post probability density distribution curve is obtained for the final random variable and the mean of this curve is the predicted average avionics surface temperature values.

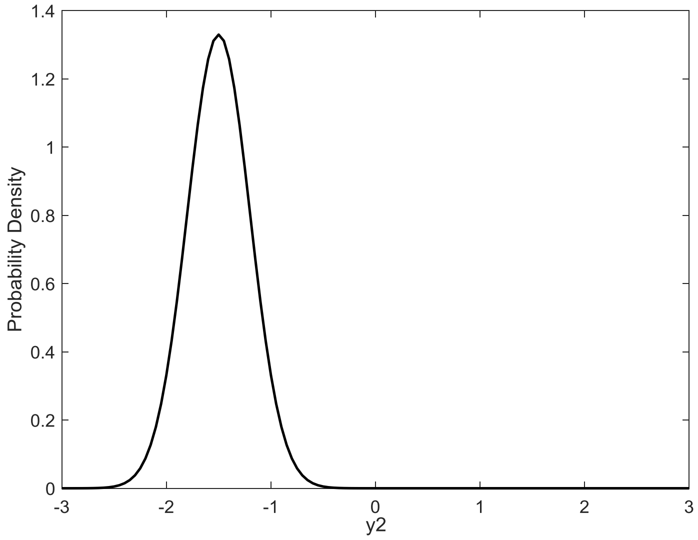

Figure 4.5. Example for Conditional Probability Calculation

4.2. Artificial Neural Network

The artificial neural networks (ANNs) are inspired by the neurons in human brain. A neuron is connected to several other neurons via dendrites. The signals coming from the dendrites act as an input for a neuron. Then, depending on the inputs, the neuron either fires through its axon or not.

An artificial neuron is schematically shown in Figure 4.6 where *x* represents the inputs received by the artificial neuron, *w* represents the weights of inputs, and *b* represents the bias. As explained by Marsland [44], the x's are first multiplied by their assigned weights and then summed. This sum is fed into an activation function (*f*) determining the output of the neuron: if the input sum is above some threshold, the neuron fires. The mathematical representation of an artificial neuron is given by Eq.(58).

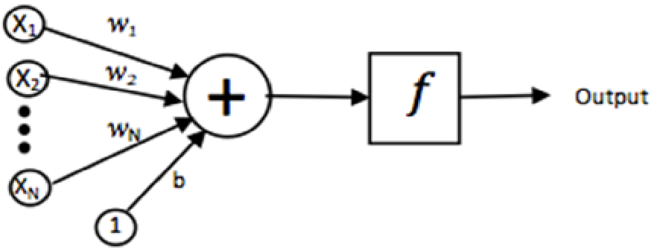

Figure 4.6. Representation of a Neuron

$$Output = f\left(\sum_{i=1}^{N} w_i\ x_i + b\right) \tag{58}$$

A neural network is formed by combining several of such neurons. A Feedforward Multi-Layer Perceptron type network is used in this study. This type of network consists of layers of neurons. These layers are the input layer, hidden layers, and the output layer. Each neuron in a layer is connected to every neuron in the previous layer and the output of each neuron in the previous layer becomes an input for this neuron [46]. In addition, the direction of the neuron connection is always from the input layer towards the output layer, i.e. the network has no recursive connections, where the input to a neuron also depends on the output of the same neuron. An example for a Feedforward Multi-Layer Perceptron network used in this study can be seen in Figure 4.7, where the circles represent the neurons and the arrows represent the input-output relations.

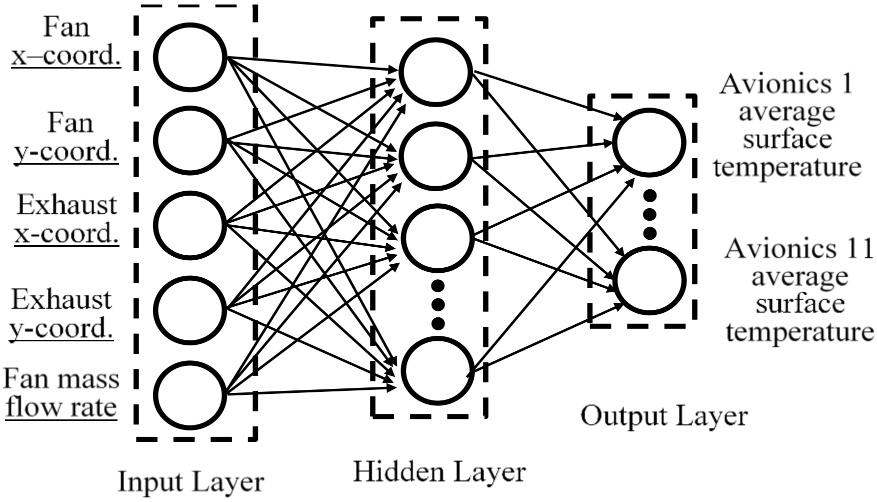

Figure 4.7. Feedforward Multi-Layer Perceptron Network

In this study, the Neural Network Fitting Application of MATLAB Release 2016a is used to create and train the ANNs. For the case of avionics-bay cooling, the input layer has five neurons each of which is an input to the problem; namely the fan location (x and y coordinates), the exhaust location (x and y coordinates) and the fan mass flow rate. On the other hand, the output layer has eleven neurons, which are the desired outputs of the average surface temperatures of eleven avionics equipment located in the bay.

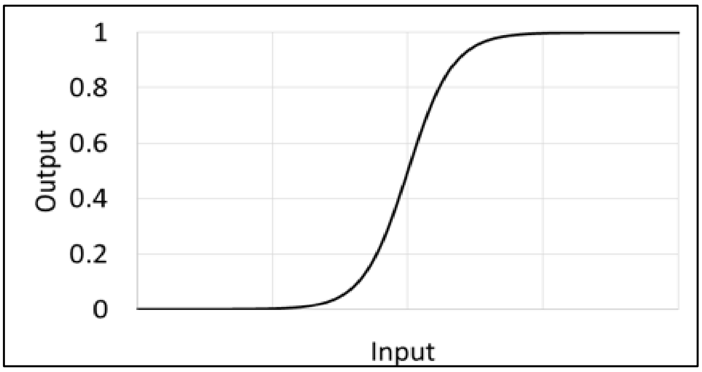

Figure 4.8. Sigmoid Activation Function

The sigmoid function shown in Figure 4.8 is used as the activation function of the neurons in the hidden layer. Depending on the value of the input, the output becomes a number between zero and one. On the other hand, a linear activation function is used for the neurons located in the output layer.

The network described above must be trained before it can be used for predicting the average surface temperatures. For this purpose, the results from the CFD analyses are used as training data. In the process of training, Eq.(58) is solved for the weights and biases for each neuron based on the input-output relations of the neurons shown in Figure 4.7. The weights and biases are varied through the training iterations in such a way that the error between the ANN outputs and the CFD results decreases. The Bayesian Regularization Back-propagation method is used for training, as this method can provide good results with small training data sets [45]. The Bayesian Regularization can also reduce the effects of overfitting, as explained below, without the need of using a validation data set [47].

As the agreement between the ANN and CFD results improves with the number of training iterations, the ANN process starts including the noise existing in the CFD data as well. Due to this, the relationship between the ANN inputs (the fan and exhaust locations, and the mass flow rate) and the ANN outputs (the avionics average surface temperatures) cannot be captured successfully. In other words; during the early stages of the training, the ANN tries to capture the physical relationship between the inputs and outputs. An ANN which could capture this physical relationship is said to have a high generalization capability. That is, the results obtained with this ANN shows similar accuracy values through the entire input parameter space. However; as the training process continues, the ANN starts to also capture the noise available in the CFD data in addition to the physical relationship. This is called overfitting. At this point, the ANN starts to memorize the CFD results of the training data rather than capturing the physical relationship and generalizing the results. Such an ANN yields accurate results for the cases included in the training data set. However, the accuracy of the results at the remaining parts of the input parameter space decreases due to the overfitting issue. To reduce the effects of overfitting, some training methods dedicate a portion of the available data set to be used for validation, leaving a reduced size of the data available for the training purposes. The validation data set is not used in the training, but the results obtained by the ANN and the CFD results for this validation data set is compared in each training iteration. Since the validation data set does not contribute to the training, the ANN results of this data set can be used to detect when the ANN starts to memorize the training data and overfitting. This is determined when the accuracy of the validation data set results starts to decrease. Then the training iterations can be stopped. On the other hand, since the Bayesian Regularization does not require a separate validation data set, a larger amount of available data can be used for training, as is done in the current study. As the larger portions of the available CFD data set are used for training, the ANNs with higher accuracy could be generated.

Then comes the determination of the ANN architecture. The architecture consists of a number of hidden layers and a number of neurons in each layer. As stated in [48], one hidden layer is enough to predict continuous functions. Therefore, an ANN with one hidden layer is used in the current study. Since the number of neurons that must be used in the hidden layer is problem-dependent, there are no specific rules to select the number of neurons. A trial-and-error process is carried out to determine this number. In order to compare the prediction capabilities of the ANN with different neuron numbers, 15% of the available CFD data is randomly selected and this data set is only used to compare the accuracy of the ANNs with different architectures. This data set is called the Testing Data. Similar to the validation data sets, testing data is not included in the training process.

In Table 4.2, the change of the mean-squared error (MSE) between the ANN and CFD results with the number of neurons in the hidden layer is shown for the training data, testing data, and the overall data set that includes the training and testing data. MSE is the mean of squared errors for the data that is used for both training and testing, and is calculated according to Eq.(59):

$$MSE = \frac{1}{r\,n}\sum_{i=1}^{r}\sum_{j=1}^{n}(T_{av-ANN} - T_{av-CFD})^2 \tag{59}$$

where r is the size of the training, testing or the overall CFD data set. n is taken as eleven, which is the total number of avionics equipment. Tav-ANN is the average avionics surface temperature predicted by the ANN and $T_{av\text{-}CFD}$ is the averaged avionics surface temperature obtained by the CFD analyses. During the training, initial values of weights and biases are determined randomly. Then an optimization study is performed to determine the weights and biases, which minimize the error between the ANN results and the CFD results. A gradient-based optimization is used. This means that there is a risk of getting caught within a local minima depending on the initial values of the weights and biases. In order to avoid this issue, the ANNs shown in Table 4.2 are trained several times and the table is formed by the best results for each ANN architecture. As it can be observed, increasing the number of neurons in the hidden layer by multiple times decreases the overall MSE significantly. However, although the MSE value decreases, the prediction accuracy for the testing data may deteriorate due to the inherent over fitting problem of the ANNs with high number of neurons, as the noise in the training data downgrades the generalization capability of the ANN.

Table 4.2. *Change of Mean-Squared Error With Number of Neurons*

# Neurons in Hidden Layer	Mean Squared Error (MSE)		
	Training Data	Testing Data	Overall Data
5	30.8	36.5	31.7
6	28.1	35.8	29.3
7	26.8	31.4	27.5
8	25.9	27.5	26.2
9	24.4	26.9	24.8
10	22.8	27.6	23.6
11	23.1	26.2	23.6
12	22.7	25.3	23.1
13	20.8	25.8	21.5
14	19.4	27.2	20.6
15	17.8	30.9	19.8
16	17.2	31.0	19.3
17	17.3	32.0	19.5
18	16.4	33.7	19
19	15.6	35.2	18.6
20	15.0	35.4	18.1
21	14.8	37.2	18.2
22	15.0	37.4	18.4
23	13.0	39.3	17.0
24	13.0	39.2	17.0
25	13.0	42.7	17.5

The blue curve in Figure 4.9 shows the variation in the MSE value of the training data with the number of neurons. As the number of neurons increases, the MSE value for the training data decreases, as expected. This is due to the fact that the ANN becomes more capable of predicting more complex functions including large gradients as the number of neurons increases. The red curve shows the variation in the MSE value of the testing data with the number of neurons. The MSE value reaches its minimum value for the first twelve neurons, but it has an increasing trend as the number of neurons is increased further. It can be concluded that after the application of the first twelve neurons, the ANN model starts to encounter the problem of over fitting and its generalization capability for the points out of the given data set decreases. Hence, the decrease of MSE of the overall data for the neuron numbers greater than twelve, as shown in Table 4.2 and with the green curve in Figure 4.9, is due to the fact that the ANN starts to predict the training data closer to the CFD results.

In other words, as the number of neurons in the hidden layer increases, the ANN gets more capable of predicting more complex functions with high gradients. On the other hand, the noise in the CFD results would contribute to such high gradients. This causes the ANNs modeled with high number of neurons in the hidden layers to become inherently more prone to overfitting despite the use of the Bayesian Regularization. That is, the improved prediction capability of the ANN can further predict the noise in the training data, whereas a model with a lower number of neurons in the hidden layer will have more tendency to ignore the noise. Therefore, the architecture of an ANN model must be chosen carefully so that there is enough number of neurons in the hidden layer to capture the relationship between the ANN inputs and outputs successfully while excluding the noise in the training data. Considering this, an ANN architecture with twelve neurons is selected in this study to avoid this issue.

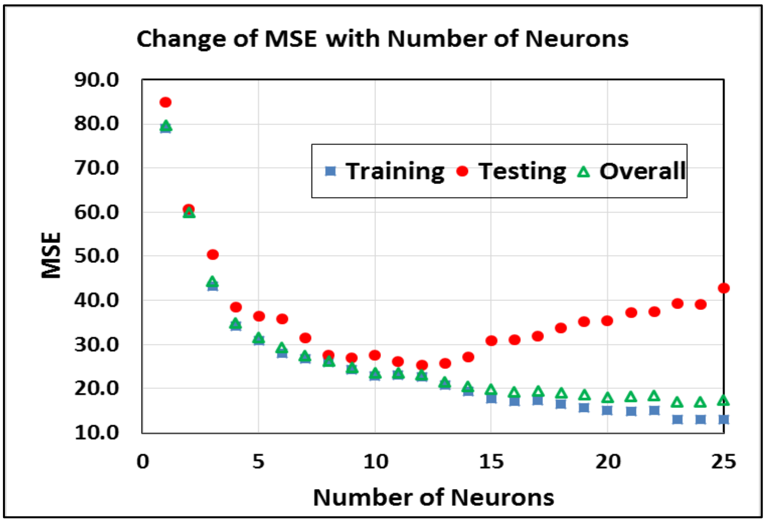

Figure 4.9. Change of MSE Values for Training, Testing, and Overall Data With Number of Neurons

Biases and weights of the selected ANN are shown in Table 4.3 - Table 4.5.

Table 4.3. *Biases of Neurons in Hidden Layer and Output Layer*

# Neuron	Hidden Layer Neuron	Output Layer Neuron
1	-1.75530	1.16307
2	-0.26037	-0.29430
3	-1.17650	1.11351
4	-1.33694	1.34729
5	0.40713	0.09610
6	0.97869	0.04484
7	-0.11827	-0.05184
8	-0.54715	-0.32064
9	-1.09921	0.69604
10	1.84159	1.18494
11	0.57455	0.49669
12	1.15417	-

Table 4.4. *Weights of Neurons in Hidden Layer and Input Layer*

		# Input Layer Neurons				
		1	*2*	*3*	*4*	*5*
# Hidden Layer Neurons	*1*	0.13982	-1.87837	-2.06020	0.01891	-0.02837
	2	0.03632	-1.76641	-0.81919	-0.09494	-0.11205
	3	0.10964	0.17808	-3.10240	0.01366	-0.12566
	4	0.05043	-1.66859	0.56768	-0.08774	0.05454
	5	0.07217	-0.01396	3.99639	0.00597	-0.02554
	6	-1.11626	-0.06062	1.51402	0.08668	-0.68936
	7	0.15510	1.05991	0.17454	0.39750	-1.18150
	8	-0.06369	0.67978	-1.25539	-0.00075	-0.00976
	9	-0.78669	-0.94935	-0.31639	0.10356	-0.82062
	10	0.04561	-2.06721	1.25810	-0.02814	0.00750
	11	0.62868	-0.19079	-0.53882	0.02774	-0.01016
	12	-1.04116	-1.14369	0.47464	0.07197	-1.02019

Table 4.5. *Weights of Neurons in Hidden Layer and Output Layer*

		# Output Layer Neurons										
		1	2	3	4	5	6	7	8	9	10	11
# Hidden Layer Neurons	1	0.63960	-0.16793	0.39750	0.47578	-0.32502	0.12551	-0.62893	-0.79226	-0.01501	0.75231	0.58880
	2	-0.32115	0.31884	0.54700	-0.72994	0.62801	-0.31025	0.74451	-0.52986	-0.80594	0.05242	-0.23224
	3	0.50174	0.08597	0.72827	-0.16132	0.19645	0.16272	1.11704	0.69140	-0.53651	-0.15938	-0.52007
	4	0.21536	-0.63269	-0.74282	0.09329	-0.22821	0.40024	-0.23010	0.62729	-0.11505	-0.94596	-0.75782
	5	0.53874	-0.01723	0.69399	0.97603	-0.66843	-0.79311	-0.56779	-0.15565	0.47402	0.87455	0.26345
	6	0.39697	0.34040	0.35670	-0.50115	0.37022	0.55822	0.67027	0.08351	-0.85119	-0.20846	-0.26904
	7	-0.11593	-0.08389	-0.06922	-0.36927	0.05001	0.10423	0.18528	-0.12281	-0.46143	-0.32010	-0.24984
	8	0.15762	-0.09225	-0.56007	0.90926	-0.38991	0.00342	-1.52534	0.10784	0.42587	-0.10549	-0.17071
	9	-0.02833	-0.04246	-0.01992	0.81673	-0.29820	-0.32890	-0.59966	0.17466	1.07384	0.50533	0.53906
	10	-0.32330	0.33358	-0.92116	-0.39479	-0.21317	0.59981	-0.01037	1.02426	-0.47709	-1.20198	-0.65844
	11	-0.41424	-0.73851	-0.77266	0.09267	-0.72329	-0.54498	-1.35254	-0.51292	0.35800	-0.25276	-0.27456
	12	-0.14347	-0.17908	-0.28253	0.56547	-0.19062	-0.27625	-0.56272	0.14986	0.83177	0.24370	0.24387

The biases of neurons in hidden layer and output layer are provided in Table 4.3. In Table 4.4, the weights of the neuron inputs between the hidden layer and the input layer are shown. In Table 4.5, the weights of the neuron inputs between the hidden layer and the output layer are shown.

Learning curves of the ANN with twelve neuron are shown in Figure 4.10. The change in MSE is shown for both training and testing data on a logarithmic scale. MATLAB uses different criteria to stop the training process [45]. The first criterion is the maximum numbers of iterations. 1000 iterations are set as the maximum value. The second criterion is the maximum value of the Marquardt Adjustment Parameter. This criterion is set to 10^{10}. As stated above, Bayesian Regularization uses a gradient-based optimization method to determine the weights and biases. The Marquardt Adjustment Parameter is used to adjust the amount of changes in the values of the weight and biases during the iterations. This parameter is increased until the performance of the network improves. Once the value of the Marquardt Adjustment Parameter exceeds the criterion, the training is stopped. The next stopping criterion is the minimum performance gradient. The training is stopped, when the rate of ANN performance improvement becomes less than 10^{-7} during the iterations. Based on these stopping criteria, the training stops after 150 iterations, since the maximum value of the Marquardt Adjustment Parameter is reached.

In addition to the MSE values given in Table 4.2, the correlation between the ANN and CFD results for the training data and the testing data is also demonstrated in Figure 4.11 and Figure 4.12. Figure 4.11 and Figure 4.12 shows the 85% of the DPs used for training and the remaining 15% used for testing. As the location of a point gets closer to the line with the 45° slope, the correlation of the data improves. The examination of these distributions reveals that the error in average surface temperatures between the ANN and CFD results of up to 20.5 K is observable. This value corresponds to an error of %5.83.

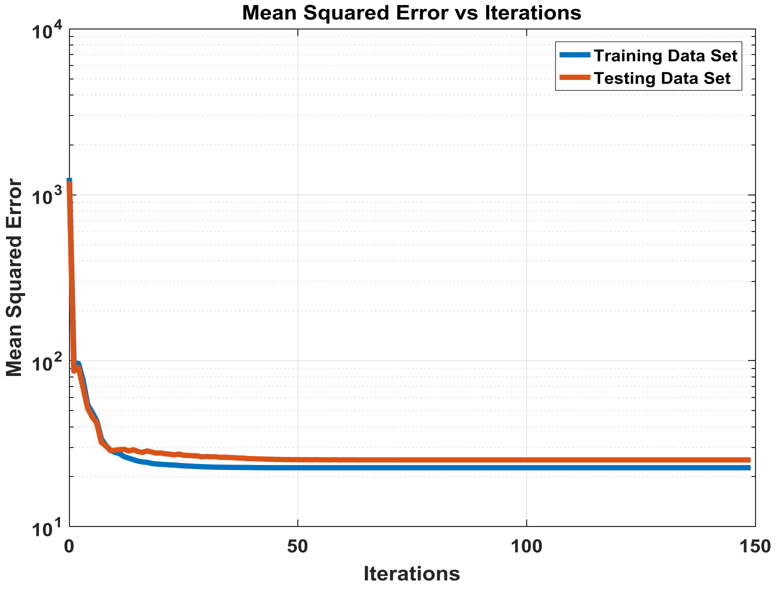

Figure 4.10. Learning Curves of ANN With Twelve Neurons

In addition, the correlation coefficients of the twelve neuron ANN for the training and testing data with the CFD results are 0.943 and 0.931, respectively. The correlation coefficient is calculated using Eq.(60).

$$r = \frac{\sum_{i=1}^{n}(T_{av-CFD} - \overline{T_{av-CFD}})(T_{av-ANN} - \overline{T_{av-ANN}})}{\sqrt{\sum_{i=1}^{n}(T_{av-CFD} - \overline{T_{av-CFD}})^2 \sum_{i=1}^{n}(T_{av-ANN} - \overline{T_{av-ANN}})^2}} \qquad (60)$$

Here n is the data size, $T_{av\text{-}CFD}$ is the avionics average surface temperatures obtained by CFD and $T_{av\text{-}ANN}$ is the avionics average surface temperatures predicted by the ANN. The bar notation shows the averaged values of CFD and ANN results over the one hundred and seventy seven data points. As the r values get closer to 1, the match between the ANN and CFD results improves.

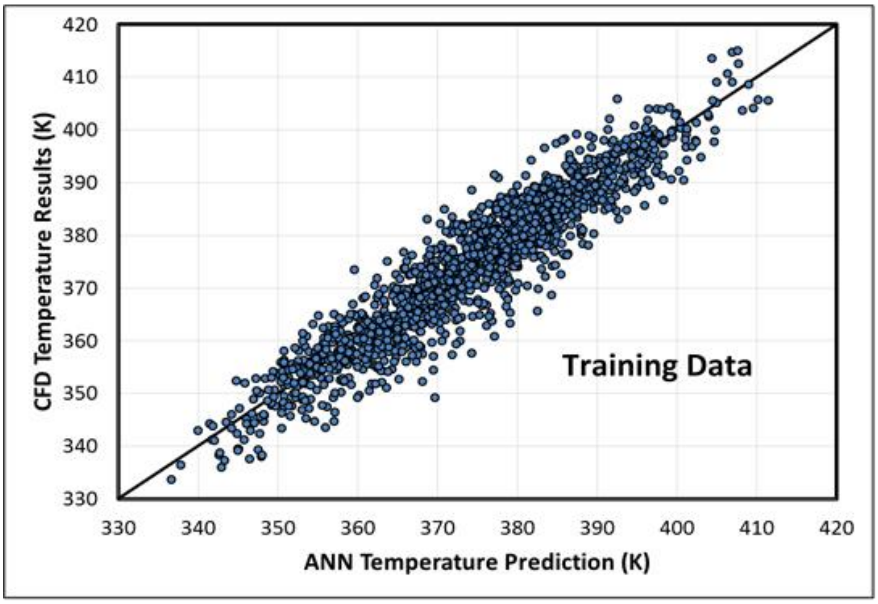

Figure 4.11. Correlation Between ANN Predictions and CFD Results for Training Data

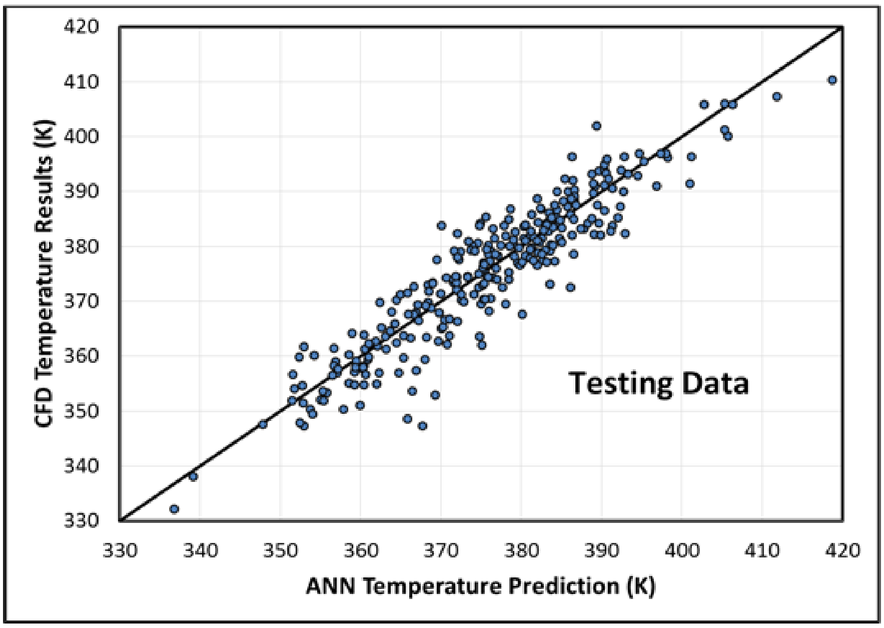

Figure 4.12. Correlation Between ANN Predictions and CFD Results for Testing Data

4.3. Prediction Function Comparison

In order to compare the Gaussian Process Regression and the Artificial Neural Network results, three additional test points are used. These additional test points were also previously used in the determination of the mean value and variance-covariance functions of the Gaussian Process Regression. Details about these test points are given in Table 4.6.

Table 4.6. *Test Points*

Test Points	*Mass Flow Rate (kg/s)*	*Fan x-Coord (mm)*	*Fan y-Coord (mm)*	*Exhaust x-Coord (mm)*	*Exhaust y-Coord (mm)*
1	0.041	350	380	750	650
2	0.051	800	600	600	150
3	0.0265	775	150	300	350

Results obtained for the test points are show in Table 4.7. The average surface temperatures for each avionics is shown for Gaussian Process Regression, Artificial Neural Network and CFD.

Table 4.*7 Comparison of Predictions From CFD and Gaussian Process Regression and Artificial Neural Network*

Avionics #	GPR Results			ANN Results			CFD Results		
	TP 1	TP 2	TP 3	TP 1	TP 2	TP 3	TP 1	TP 2	TP 3
Avionics 1	340.4	350.1	361.2	342.8	352.8	359.5	336.8	350.7	358.3
Avionics 2	372.1	370.2	377.4	373.2	370.1	376.9	377.1	372.7	378.5
Avionics 3	371	365.6	385.2	367.8	370.5	384.6	365.8	370.5	388.1
Avionics 4	359.4	371.7	372.5	356.2	381.3	373.2	354.0	373.2	364.1
Avionics 5	382.6	355.6	393.9	384.2	355.1	393.7	382.9	350.9	391.6
Avionics 6	388.1	371	402.1	382.4	370.0	398.1	389.4	370.7	401.2
Avionics 7	392.8	361	402.7	388.4	365.6	400.8	392.2	356.6	399.8
Avionics 8	363	371.1	390.7	369.3	372.5	390.0	364.8	370.5	391.0
Avionics 9	380.7	389.1	385.2	376.7	397.1	381.5	376.0	392.7	388.2
Avionics 10	368.7	375.2	359.3	364.7	375.5	365.2	371.9	372.2	359.2
Avionics 11	361	360.5	345.9	355.9	360.1	350.2	363.6	358.2	346.3

In Figure 4.13 and Figure 4.14, the errors plots for the Artificial Neural Network and the Gaussian Process Regression are shown. Errors are the absolute values of the differences between the results of the prediction functions and the CFD results. In addition, the differences between the Gaussian Process Regression and Artificial Neural Network are shown in Figure 4.15.

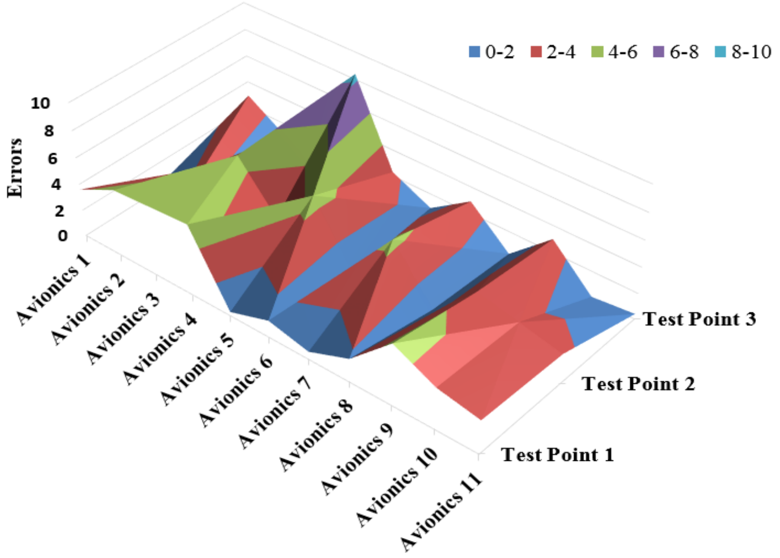

Figure 4.13. Average Avionics Surface Temperature Errors Between Gaussian Process Regression and CFD Results

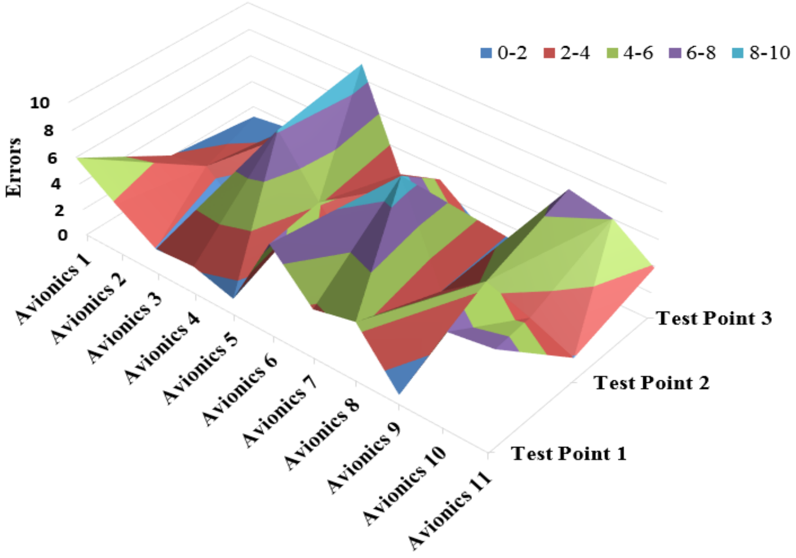

Figure 4.14. Average Avionics Surface Temperature Errors Between Artificial Neural Network and CFD Results

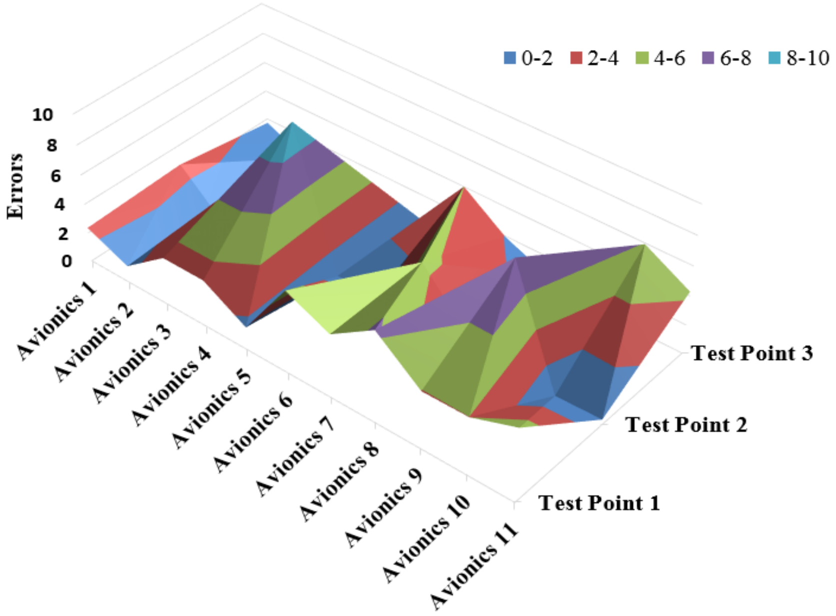

Figure 4.15. Average Avionics Surface Temperature Differences Between Gaussian Process Regression and Artificial Neural Network

It is observed that the average differences between the Gaussian Process Regression and the CFD results is 2.6 K. This value corresponds to a 0.72% error in average. On the other hand, the difference between the Artificial Neural Network and CFD results is 3.8 K, which corresponds to a 1.01% error on average. Since the average error values for the Gaussian Process Regression are lower compared to those for the Artificial Neural Network, the Gaussian Process Regression is selected to build the prediction function. In addition, the maximum deviation between the Gaussian Process Regression and Artificial Neural Network results is further examined for Avionics 4 at Test Point 2 in Figure 4.15. The value of the deviation is 9.6 K.

On the other hand, the maximum difference between the Gaussian Process Regression and the CFD results is 8.4 K. This value is observed for Avionics 4 at Test Point 3. A closer look at the error plot in Figure 4.13 reveals that the error for Avionics 4 at Test Point 3 is significantly higher than the other error values. In addition, the maximum difference between the Artificial Neural Network and CFD results is 9.1 K and it is also observed for Avionics 4 at same test point. In Figure 4.16, the fan and exhaust locations for Test Point 3 are shown. The fan location is shown with the blue-colored surface and the exhaust location is shown with the red-colored surface. In addition, the streamlines inside the bay could be observed. The streamlines are colored by the velocity magnitude. A stream of air supplied by the fan flows towards the Avionics 4 after impingement. High air velocity magnitudes occur around Avionics 4. However, there is other equipment close to Avionics 4 where the air velocity is also high, but such high errors are not observed in the region around them. The reason for the higher error might be due to the fact that the training data set does not include the case in which an air stream flows towards Avionics 4 after impingement.

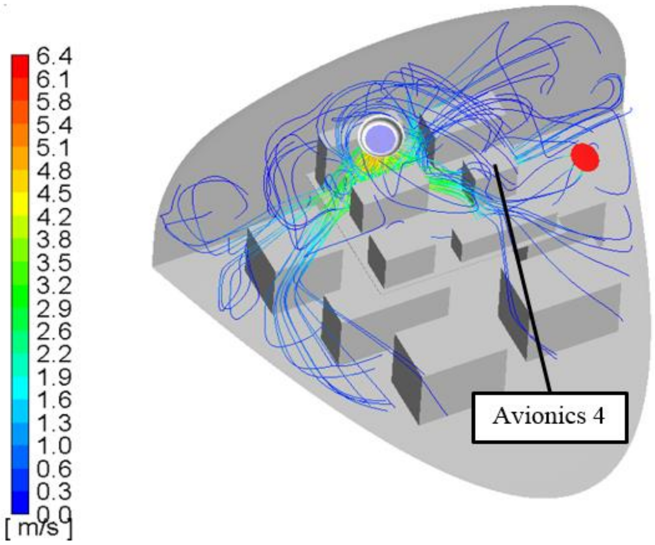

Figure 4.16. Test Point 3 Stream Lines in the Avionics Bay

In order to observe the effect of the number of CFD data points used in the analysis on the error, the change in the Gaussian Process Regression and Artificial Neural Network errors with the available data size is examined next. The size of the available data is increased up to one hundred and seventy seven cases progressively in increments of twenty CFD data points to observe the trend line of the variation in the error.

The error variation in the average surface temperature with the size of available data is shown in Figure 4.17. These error values are also calculated by the utilization of three additional test points mentioned above. The differences between the temperature values obtained with prediction functions and the CFD results are averaged over the avionics equipment and the test points to generate Figure 4.17. The temperature differences between the Gaussian Process Regression, Artificial Neural Network and CFD results are averaged using Eq.(61).

$$Avg\ Error = \frac{1}{mn}\sum_{i=1}^{m}\sum_{j=1}^{n}|T_{av-PRE} - T_{av-CFD}| \tag{61}$$

where m is the number of test points, n is the number of avionics equipment, $T_{av\text{-}PRE}$ is the average avionics surface temperature predicted by Gaussian Process Regression or Artificial Neural Network and $T_{av\text{-}CFD}$ is the average avionics surface temperature obtained by the CFD analyses.

What are also shown in Figure 4.17 are the results from a classical response surface (RS) that is typically used in such analyses. For a comparison, an RS was also built by using different sizes of the available CFD data. A full quadratic linear model given in Eq.(62) was used for the generation of the RS.

$$T_{av-RS} = \sum_{i=1}^{5} {x_i}^2 + \sum_{i\neq j} x_i\, x_j + \sum_{i=1}^{5} x_i + C \tag{62}$$

Here, $T_{av\text{-}RS}$ is the avionics average surface temperature predicted by the Response Surface, *x* is the input to the problem (i.e the fan and exhaust locations and the mass flow rate) and C is a constant.

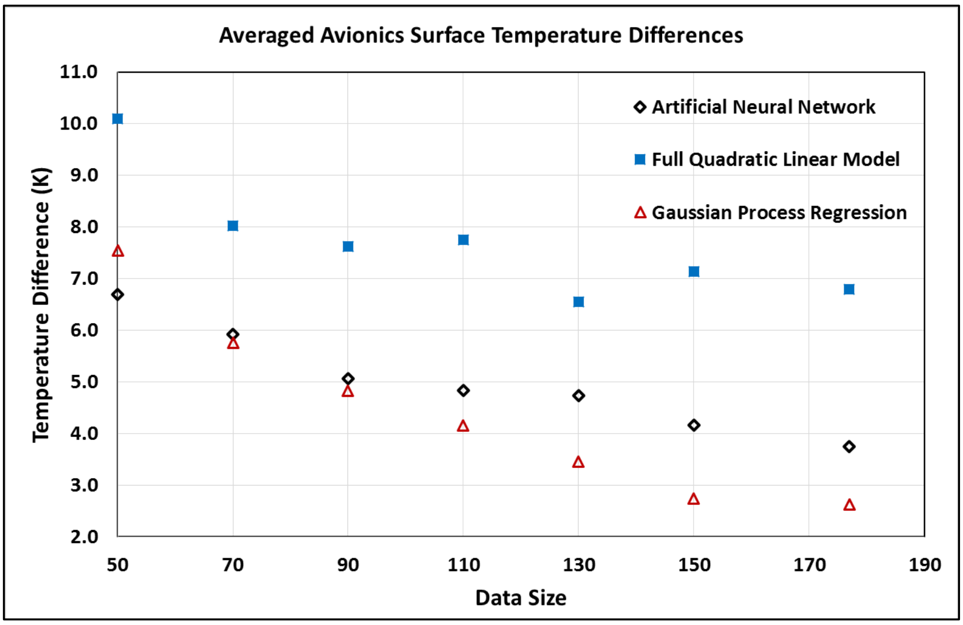

Figure 4.17. Error Variation in ANN and RS With Data Size

The decreasing trend of the error seen in Figure 4.17 suggests that the correlation between the Gaussian Process Regression and Artificial Neural Network results and the CFD results could be further improved by increasing the available data points if desired. Although this is true, it should be kept in mind that there will still be differences between the CFD results and the real life results depending on the modeling capability of the CFD. Besides, such a correlation would require performing more CFD analyses, which would be time consuming. Hence, there is a tradeoff between the accuracy of the methodology and the process time. Considering this, an error of 2.6 K obtained by the Gaussian Process Regression is considered to be accurate enough for the design exploration and optimization study pursued here. It is observed that up to ninety data points the accuracy of Gaussian Process Regression and Artificial Neural Network is similar. Beyond this data size, the Gaussian Process Regression starts to predict average avionics surface temperatures more accurately.

On the other hand, the error variation for the RS with the quadratic linear model shows that the RS is saturated beyond a data size of one hundred and ten, and increasing the available data size further beyond this point does not improve the prediction capability of the RS. The comparison to the Gaussian Process Regression and Artificial Neural Network also reveals that the RS performs worse for every data size considered compared to others

At the end of this comparison, since the average error value for the Gaussian Process Regression is lower compared to that of the Artificial Neural Network, the Gaussian Process Regression is selected to build the prediction function that will be used in the remaining of this study.

CHAPTER 5

OPTIMIZATION

In this chapter, the optimization algorithm used to determine the fan and exhaust locations yielding the smallest fan mass flow rate is described. In the end of the chapter, the resulting cooling system with the optimum fan and exhaust locations is presented.

5.1. Optimization Algorithm

The genetic algorithm is used for the optimization. The Matlab optimization toolbox [45] is used for the analysis. The algorithm imitates the evolution of a species over several generations in order to find the global maxima or minima of a function. The generations consisting of several individuals are formed. These individuals have chromosomes where the numerical values of the variables are stored at. In the current study, each individual has four chromosomes, and the fan and exhaust locations are stored at the individual's chromosomes. An example for an individual is shown in Figure 5.1.

Fan x-Coord.	**Fan y-Coord.**	**Exhaust x-Coord.**	**Exhaust y-Coord.**
200	400	600	100

Figure 5.1. Example for an Individual (in mm)

During the optimization, the first generation of individuals is formed randomly. Then, the fitness of each individual in a generation is determined. During the biological evolution, the fittest members of a species survive. This concept is also utilized in the genetic algorithm. Therefore, a measure to evaluate the fitness of the individuals is required. The required mass flow rate is used as this fitness measure. For the fan and exhaust locations stored in the chromosomes of the individuals, the smallest value of the mass flow rate required to keep the average surface temperature of all avionics equipment below their temperature limits is determined. The smaller the required mass flow rate is, the more fit the individual becomes. After the evaluation of the fitness of all individuals, the next generation is formed. Three different mechanisms are used to form the individuals of the next generation [44]. The first mechanism is including the elite individuals directly in the next generation. The elite individuals are the ones with the best fitness values among the individuals of the current generation. The second mechanism is performing a crossover where two parent individuals are selected from the current generation and their chromosomes are combined to form a new individual. An example for a crossover is given in Figure 5.2. Matlab forms a binary random vector, which is at the same size of an individual [45]. If the value of binary vector, corresponding to a chromosome is 1, the first parent's chromosome is used; if the values is 0, the chromosome of the second parent is used.

	Fan x-Coord.	**Fan y-Coord.**	**Exhaust x-Coord.**	**Exhaust y-Coord.**
Parent 1	150	300	800	800
Parent 2	500	50	900	100
Binary Random Vector	1	1	0	0
New Individual	150	300	900	100

Figure 5.2. Example for Crossover (in mm)

The third mechanism is the mutation where some of the chromosomes of the individuals are altered randomly. An example for mutation can be seen in Figure 5.3. A random number is added to each chromosome of an individual [45] to mutate. The random number is generated from a random variable that has a Gaussian distribution and a zero mean value.

	Fan x-Coord.	**Fan y-Coord.**	**Exhaust x-Coord.**	**Exhaust y-Coord.**
Individual	1000	10	300	700
Mutated Individual	1015	**25**	265	724

Figure 5.3. Example for Mutation (in mm)

Following these steps, the fitness values of the individuals of the new generation are evaluated, and the process is repeated to form the new generation. New generations are formed until the smallest mass flow rate required to keep all avionics equipment surface temperatures below their temperature limits stops altering significantly. Each generation used during the optimization has two hundred individuals. It is stated in the Matlab User Guide that fifty individuals are enough for problems with five parameters or less, and two hundred individuals are suggested for a higher number of parameters [45]. Since the evaluation of the fitness of the individuals does not take too much time, generations with two hundred individuals are used in this study to be conservative. During the reproduction of the next generation, ten elite individuals are directly included in the next generation. One hundred and fifty two individuals of the next generation are formed by crossover and the remaining thirty eight individuals are formed by mutation.

5.2. Fitness Evaluation of Individuals

As mentioned above, the required minimum mass flow rate is used to determine the fitness of an individual. The minimum required mass flow rate is obtained, when the average avionics surface temperatures of some equipment are equal to their limits and the average surface temperatures of remaining equipment are below the limits. However, the prediction function built in the previous chapters uses mass flow rate as an input parameter and gives the average avionics surface temperatures as outputs. The prediction function must be used in such a way that the output is the mass flow rate.

In order to do that, the temperature limits of the avionics are used. The fan and exhaust location inputs of the prediction function come from the chromosomes of an individual. Then a mass flow is selected initially and the average avionics surface temperatures results are obtained by the utilization of the prediction function. Following this, the results are compared with the temperature limits. If the temperature values exceed the limits, the mass flow rate is increased. If all temperature values are below the limits, the mass flow rate is decreased. The mass flow rate is altered until some of the avionics surface temperatures become equal to the limiting values, while the others are below the limits.

The mass flow rate is altered by the bi-sectioning method. The process steps of the bi-sectioning method are presented below:

1. Set the higher and lower mass flow rate values to 0.055kg/s (upper limit) and 0.024 kg/s (lower limit), respectively
2. Calculate the new mass flow rate value by taking the arithmetic average of higher and lower mass flow rate values
3. Determine the average avionics surface temperatures with the new mass flow rate
4. Calculate the temperature difference for all eleven avionics by subtracting the predicted temperature values from the limiting values

5. If the minimum of the eleven temperature difference values is higher than 0.001K, set the calculated mass flow rate as the new higher mass flow rate value and move to step 2
6. If the minimum of the eleven temperature difference values is lower than -0.001K, set the calculated mass flow rate as the lower mass flow rate value and move to step 2
7. If the minimum of the eleven temperature difference values is between 0.001 and -0.001, then the calculated mass flow rate is the required minimum mass flow rate.

The Matlab code used to evaluate the fitness of individuals is included in APPENDIX C.

The procedure mentioned above yields mass flow rate values only between the lower and upper limits of the mass flow rate range. There could be cases with the fan and exhaust locations returning even a higher mass flow rate than the range upper limit. With the procedure listed above, the required mass flow rate values for these cases are also determined as 0.055kg/s on purpose. The training data of the prediction function is generated for a mass flow rate range between 0.055kg/s and 0.024kg/s. Therefore, the accuracy of the prediction function decreases significantly for the mass flow rates higher than 0.055 kg/s. As an example, the change of avionics 2 average surface temperature with the fan mass flow rate is shown in Figure 5.4. The plot corresponds to x=100 mm and y=300 mm for the fan coordinates, and x=500 mm and y=600 mm for the exhaust coordinates. As it is seen, the average surface temperature starts to increase as the mass flow rate increases above 0.08 kg/s. Such a behavior is physically incorrect and it could mislead the optimization algorithm. Therefore, the maximum required mass flow rate value is limited at 0.055 kg/s.

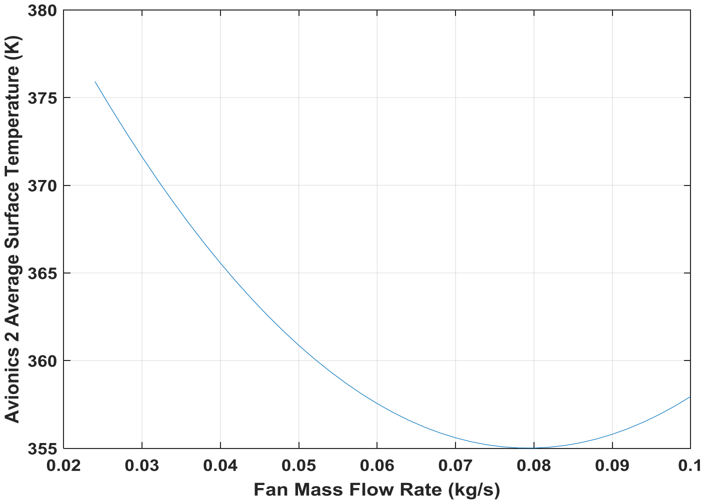

Figure 5.4. Change of Avionics 2 Average Surface Temperature With Mass Flow Rate

The Genetic Algorithm may produce individuals with fan and exhaust located out of their location envelopes. The required mass flow rate values for them are also set at 0.055 kg/s, so that these individual are penalized with bad fitness values and are eliminated during the optimization process.

5.3. Result of Optimization

The Genetic Algorithm continues for one hundred and three generations. The change of the best fitness and mean fitness values are shown in Figure 5.5. As the figure suggests, significant improvements are achieved in the mass flow rate up to the twelfth generation. After this point, the improvement rate decreases.

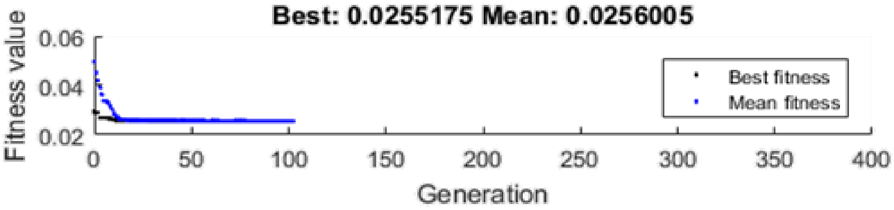

Figure 5.5. Change of Best and Mean Fitness Values

Finally, the optimum fan and exhaust locations determined by the Genetic Algorithm are shown in Figure 5.6.

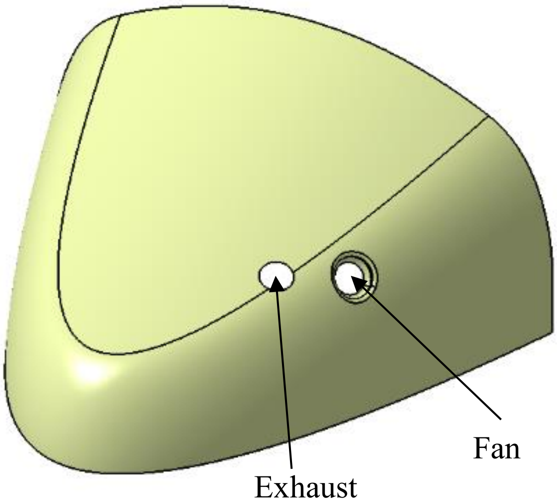

Figure 5.6. Optimum Fan and Exhaust Locations

The numerical values of the fan and exhaust location are also presented in Table 5.1. The mass flow rate corresponding to these fan and exhaust locations is 0.0255 kg/s and is within the mass flow rate range determined previously. This indicates that it is not required to generate additional DPs and run additional CFD analyses to extend the mass flow rate range.

Table 5.1. *Optimum Fan and Exhaust Locations (in mm)*

Fan Location		*Exhaust Location*	
x-coord.	*y-coord.*	*x-coord.*	*y-coord.*
220.8	435.4	363.8	579.2

.

CHAPTER 6

RESULTS AND DISCUSSION

6.1. Comparison of Optimum Case Results With CFD

Following the determination of the optimum cooling geometry and the optimum mass flow rate, a CFD analysis is performed to investigate the resulting thermal environment inside the bay under those conditions. An upfront-check of the equipment surface temperature predictions obtained by CFD with those predicted by the Gaussian Process Regression showed that the average difference is only 2.4 K, which agrees with the accuracy level that was confirmed earlier by the test points. If desired, the results could be improved further by adding more DPs around the optimum point found via the genetic algorithm. These new design points could then be used to enhance the prediction function. However, this effort would only locally increase the accuracy around the regions of interest, and it would not have an effect over the whole input parameter domain. The average avionics surface temperatures obtained with the Gaussian Process Regression and CFD analyses are presented in Table 6.1.

Table 6.1. *Comparison of CFD Results and Gaussian Process Regression Predictions for Optimum Fan and Exhaust Locations*

Avionics #	*CFD Result (K)*	*Gaussian Process Regression Prediction (K)*	*Differences (K)*
Avionics 1	353.4	355.4	1.9
Avionics 2	373.3	380.8	7.5
Avionics 3	389.4	385.5	3.9
Avionics 4	369.5	369.1	0.4
Avionics 5	384.8	384.1	0.7
Avionics 6	392.0	391.4	0.6
Avionics 7	391.9	391.5	0.3
Avionics 8	374.3	373.7	0.6
Avionics 9	389.6	390.0	0.4
Avionics 10	382.7	375.8	6.9
Avionics 11	368.4	364.7	3.7

6.2. Effect of Optimization on Power Consumption

The upper limit value of the mass flow rate was determined as 0.055kg/s based on the fan and exhaust locations mentioned in CHAPTER 3. After applying the optimization process, this value is reduced to 0.0255 kg/s. Therefore, the mass flow rate that is necessary for proper cooling of the avionics equipment is reduced by half.

On the other hand, power savings achieved with the optimization process is even more significant. The power consumed by a fan can be calculated by Eq.(63):

$$\dot{W} = \frac{\dot{m}}{\eta\rho}\Delta P \tag{63}$$

where, η is the efficiency of the fan, ṁ is the mass flow rate, ρ is the density of the air, and ΔP is the static pressure rise across the fan. From the CFD results, the static pressure rise across the fan is calculated as 99.5 Pa for the case with 0.055 kg/s mass flow rate, and 19.9 pa for the optimized case with 0.0255 kg/s. The density is the same for both fans since they both draw the outside air at 323.15 K. Since the efficiency strongly depends on the technology level, it is assumed to be equal for both fans. As a result, it can be concluded that the fan with 0.055 kg/s mass flow rate consumes around ten times more of the power consumed by the fan with 0.0255 kg/s. This shows that the locations of the fan and exhaust might drastically change the amount of power required for a proper system cooling.

6.3. Effect of Fan and Exhaust Location on Mass Flow Rate

In Figure 6.1 and Figure 6.2 the variation of the required mass flow rate with the fan and exhaust locations is shown.

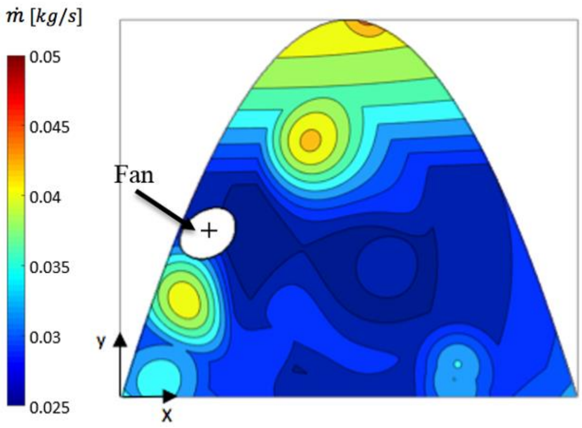

Figure 6.1. Variation of Mass Flow Rate with Exhaust Location

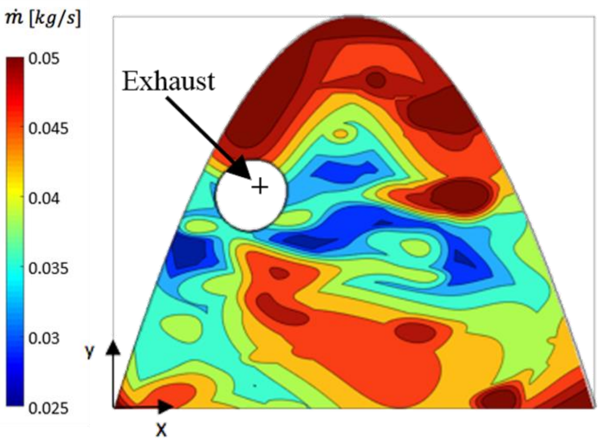

Figure 6.2. Variation of Mass Flow Rate with Fan Location

In Figure 6.1, the fan location is kept fixed at the point obtained by the genetic algorithm and the exhaust location is varied across the skin. The prediction function is used to determine the required mass flow rate to cool the avionics equipment at each exhaust location. In Figure 6.2, the exhaust location is kept fixed at the optimum point and the location of the fan is altered. The white zones represent where the exhaust and the fan locations coincide, hence there is no data available there. As it can be seen, the mass flow rate strongly depends on the fan location. Considering the large gradients in the contour plot, a small change in the fan location may cause a significant increase in the mass flow rate. On the other hand, the required mass flow rate is much less sensitive to the changes in the exhaust location.

Vectors and colored contours show the velocity distribution at different planes inside the bay in Figure 6.3. The length of vectors are also proportional to the magnitude of the velocity. Planes on the left and right views are aligned with the axes of the fan and the exhaust, respectively, whereas the plane at the bottom cuts through the avionics bay horizontally at a location 450 mm above the floor. These planes can also be observed in Figure 6.3. In addition, flow around the fan and exhaust are displayed with zoomed in figures, as the velocity magnitudes at these regions are higher.

In order to understand the reasons of strong dependency on the fan location and weaker dependency on the exhaust location, the velocity field inside the bay is investigated. Vectors and colored contours show the velocity distribution at different planes inside the bay for optimum fan and exhaust locations in Figure 6.3. The length of vectors is proportional to the magnitude of the velocity. Planes on the left and right views are aligned with the axes of the fan and the exhaust, respectively, whereas the plane at the bottom cuts through the avionics bay horizontally at a location 450 mm above the floor. These planes can also be observed in Figure 6.3. In addition, the flow around the fan exhaust is displayed with a blow-up figure due to the higher velocity magnitudes observed in these regions.

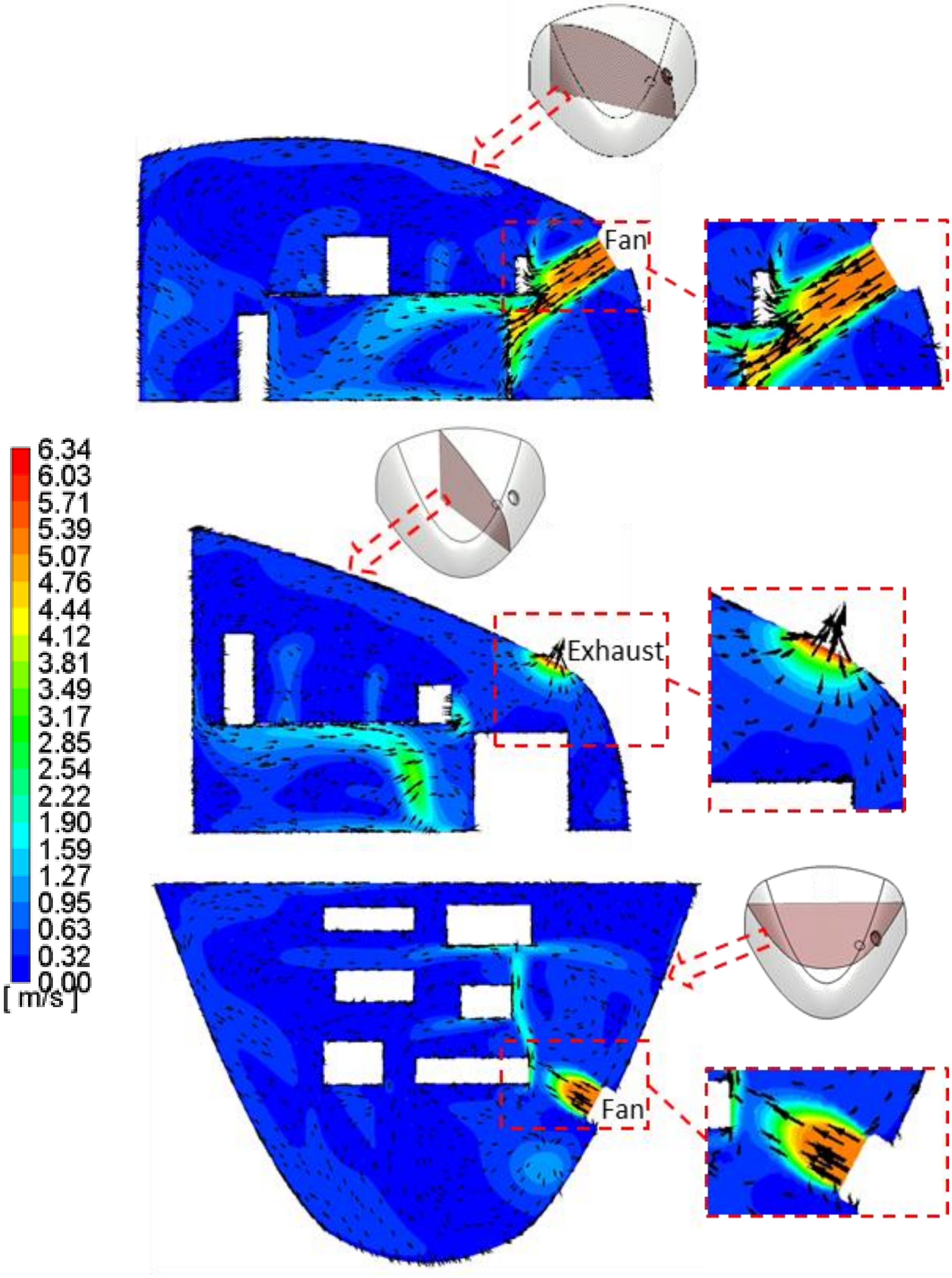

Figure 6.3. Velocity Contours and Vector Plots for Optimum Fan and Exhaust Locations

The air jet impinges on the solid equipment surfaces, resulting in a strong flow recirculation and a velocity gradient in the flow domain. Apparently, this air jet occurs at the exit of the fan in the direction normal to the skin surface, whereas the exhaust draws air from all directions. This can be interpreted as the reason to the strong dependency of the mass flow rate on the fan location. Since even a small change in the fan location has a significant effect on the flow field inside the bay, it also has a significant effect on the average avionics surface temperatures. On the other hand, since the exhaust draws air from all direction, the flow field inside the bay is less sensitive to the exhaust location.

In Figure 6.1, it can also be seen that as the exhaust location is moved towards the forward of the bay, the required mass flow rate increases. The equipment could not be installed in the forward part of the nose avionics bay, since the cross-section of the bay narrows down. Locating the exhaust at the forward section of the bay would increase the air speed values here and reduces the air speed values at the aft part of the bay, where the equipment is located. Additionally, a high mass flow rate region is observed for the exhaust location at the rear left side of the skin. This is a location close to the region where the fan air jet impinges on the avionics equipment walls. This causes the air supplied by the fan to be drawn by the exhaust directly. Therefore, an effective air distribution inside the bay could not be achieved, requiring a higher mass flow rate. According to Figure 6.2, the required mass flow rate increases as the fan is moved towards the forward of the avionics bay, as well. The exhaust location in optimum case is already close to the forward section of the bay. Therefore, moving the fan to this section nearby the exhaust would cause poor air distribution inside the bay.

The details of the fan air jet are provided in Figure 6.4. The streamlined originating from the fan are colored according to the velocity magnitude. The jet is directed towards the edge of avionics 1. As a result, the jet is divided into streams in different directions. Some part of the jet is directed toward the zone below the rack, whereas the rest is distributed along the side of the rack. Therefore, a more effective air distribution can be achieved inside the bay by dividing the jet into separate streams.

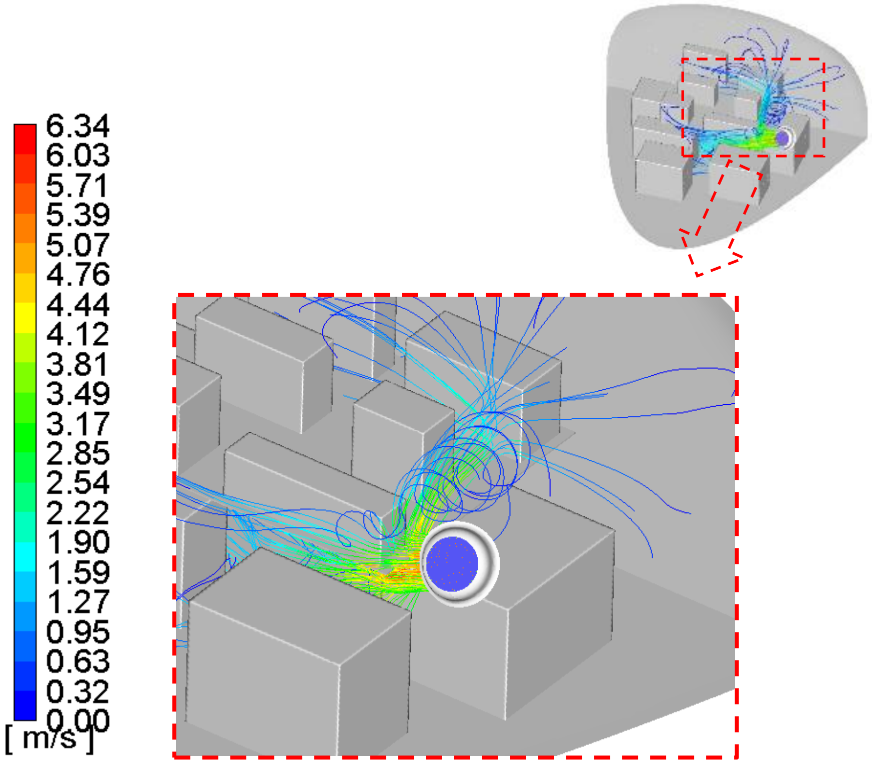

Figure 6.4. Details of Fan Air Jet

The effect of this split of the jet streams can also be seen in the temperature contours of Figure 6.5. In the top figure, the temperature distribution on a vertical plane across the bay is shown. The bottom figure shows the temperature distribution on a horizontal cut that is parallel to the rack. The upper limit of the color legend is set to 353.0 K to capture temperature gradients in more detail. Air temperature will be higher inside the thermal boundary layer around avionics, since the avionics average surface temperatures are higher than this value as given in Table 6.1. The air jet can be tracked by the low air temperature values. As the air jet impinges on the walls of the avionics equipment, the temperature values increase due to the stagnation of the flow.

Additionally, it is observed that the required mass flow rate increases as the fan is moved towards the aft of the skin in Figure 6.2. Since there is no room left here for the fan air jet to split into streams, it only impinges on the upper surface of the rack. This results in a poor air distribution around the equipment installed on the floor of the nose avionics bay. On the other hand, as the fan is moved towards the sides of the aft section, the required mass flow rate decreases, since the jet impinging on the sides is distributed more effectively across the bay, including the zone underneath of the rack.

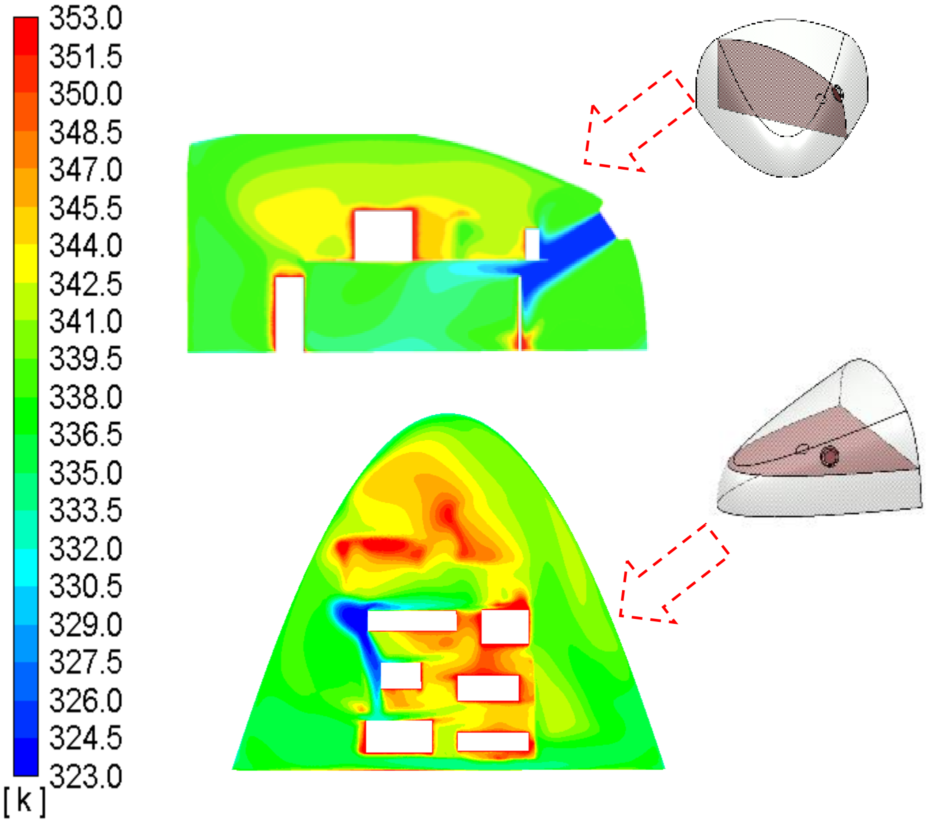

Figure 6.5. Fan Jet Temperature Contours

The mass flow rate distributions shown in Figure 6.1 and Figure 6.2 are arithmetically-averaged in the y direction and are plotted as a function of x location in Figure 6.6. The averaging is performed at four hundred x locations to form the curves in Figure 6.6. The blue curve is the average of the contour in Figure 6.1 where the fan is kept fixed at the optimum location, and the red curve is the average of the contour in Figure 6.2 where the exhaust is kept fixed at the optimum location. It is also obvious from Figure 6.6 that the changes in the exhaust location cause a lessened effect on the required mass flow rate. According to the red curve, the mass flow rate is reduced as the fan moves towards the sides of the skin, but it starts increasing as the fan is moved further near the sides. In addition, the middle part of the skin also seems to be a location to be able to keep the required mass flow rate at a relatively low level. This is consistent with what is observed in Figure 6.2.

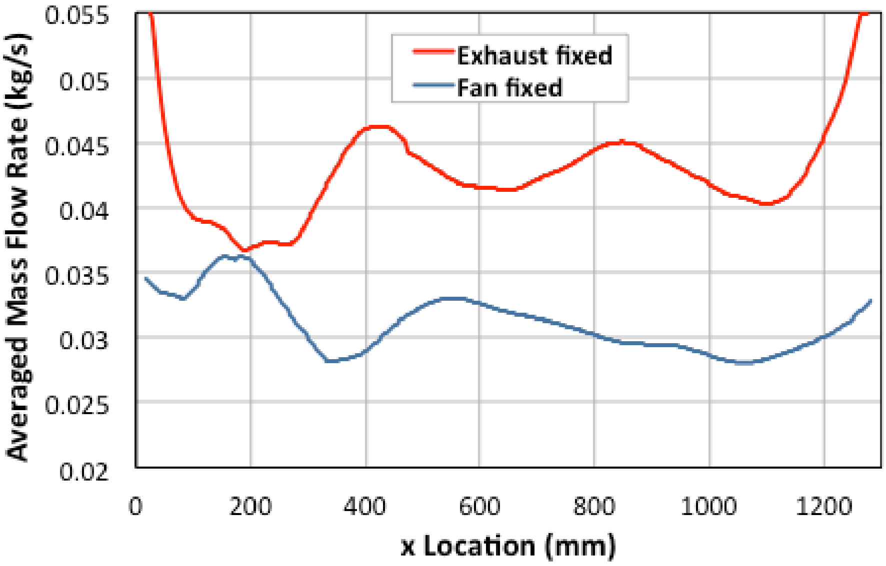

Figure 6.6. Variation of Averaged Mass Flow Rate

In order to investigate further the optimum case flow with thermal fields inside the bay, several contours are generated and shown in Figure 6.7. The contours are created on planes that are parallel and offset to the floor of the bay. The amount of the offset is also shown above each contour. The temperature distribution at each plane is shown by including in-plane velocity vectors that are also shown with black arrows. The lengths of the arrows are proportional to the velocity magnitudes.

As mentioned above; a portion of the fan jet gets under the rack after its impingement. The behavior of this branch can be especially seen in plane offset 200 mm. It is observed that this branch flows towards the frame of the bay after it gets under the rack. The effects of this branch can also be traced in planes with offset 50 mm, offset 100 mm and offset 150 mm, with local high velocity and low temperature regions. As the planes get closer to the floor, the effects of this branch weaken. The planes offset between 250 mm and 400 mm show the avionics located on the rack. In 250 mm and 300 mm offset planes, the impingement of the jet could be also clearly observed. The fan jet branches seem to have no impact in 350 mm and 400 mm offset planes. Aside from the fan jet branches, the velocity magnitudes are small inside the bay. The plane offset 350 mm from the floor is located just above some of the avionics equipment. Therefore, hot plume created by the upper surface of these equipment could be seen in this plane. In general, the forward section of the bay is hotter. This is due to the fact that the exhaust is located closer to the forward section of the bay.

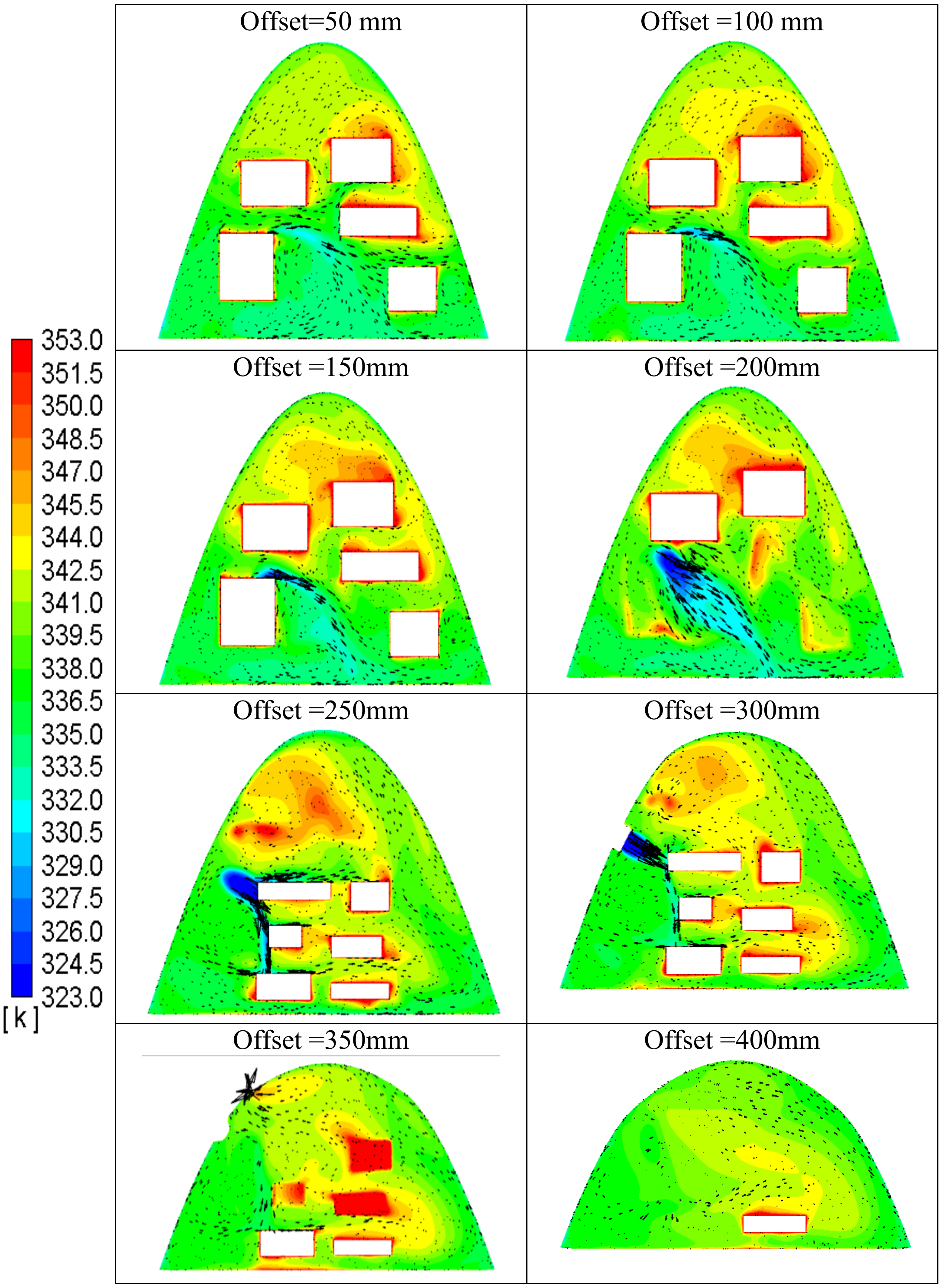
Offset=50 mm

Offset =100 mm

Offset =150mm

Offset =200mm

Offset =250mm

Offset =300mm

Offset =350mm

Offset =400mm

Figure 6.7. Optimum Case Flow and Thermal Field Contours

6.4. Effect of Fan and Exhaust Locations on Avionics Surface Nusselt Numbers

In order to evaluate the effect of the fan and exhaust locations on the avionics surface Nusselt numbers, the design points are investigated. The design points with the fan mass flow rate values closest to the one for the optimum case are determined and the avionics surface Nusselt numbers are compared for these cases. Four fan and exhaust location configurations are shown in Figure 6.8.

The Nusselt numbers for avionics equipment are calculated using Eq.(64).

$$Nu = \frac{Q_{convection}\, d_{fan}}{A_{avionics}(T_{avionics} - T_{inlet})k} \tag{64}$$

where, $Q_{convection}$ is the convective heat transfer from the avionics equipment, d_{fan} is the diameter of the fan, $A_{avionics}$ is the surface area of the avionics equipment, $T_{avionics}$ is the average surface temperature of the avionics, T_{inlet} is the temperature of air at the exit of the fan, and k is the thermal conductivity of air.

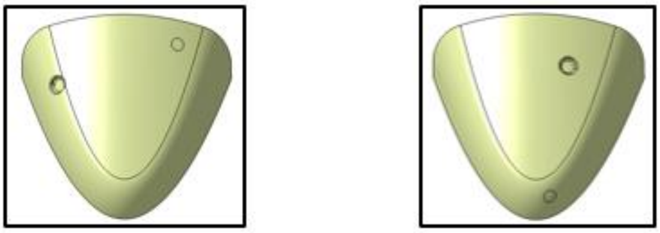

Case A (0.0256 kg/s) **Case B (0.0258 kg/s)**

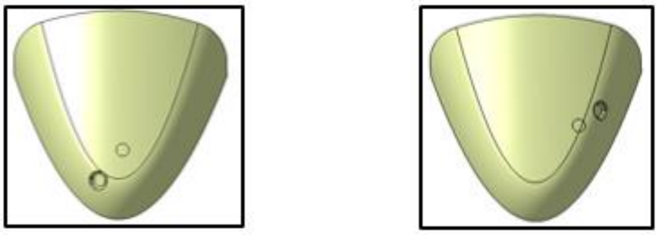

Case C (0.0255 kg/s) **Case O (Optimum-0.0255 kg/s)**

Figure 6.8. Cases With Mass Flow Rate Closest To Optimum Value

In Figure 6.9, avionics average surface Nusselt numbers are shown for each case in Figure 6.8. By comparing the equipment locations and the Nusselt numbers in Figure 6.9, it can be concluded that when the fan is located close to the avionics equipment, the Nusselt number of those equipment increase significantly. However, locating the exhaust close to the equipment does not cause a significant increase in the Nusselt numbers. Excluding those equipment close to the fan locations, the average Nusselt number is found around 15.

In Figure 6.10, the average surface temperatures of the avionics equipment are shown with their corresponding temperature limits. For case A, case B and case C, some equipment is observed to exceed their temperature limits. The reason why there is not sufficient cooling for those cases is that the rack does not allow proper flow circulation around the equipment and/or the exhaust is located close to a region where the fan air jet impinges, hence causing the air supplied by the fan to directly be exhausted without effectively flowing around the bay. Therefore the equipment located far from the region of jet impingement may not be cooled effectively.

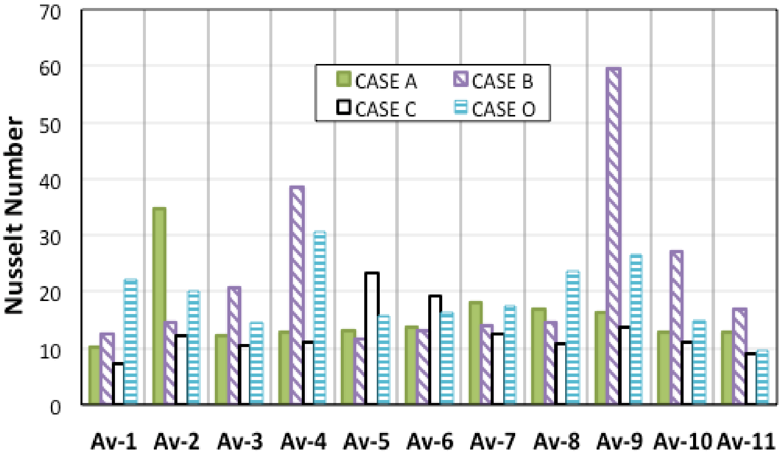

Figure 6.9. Avionics Nusselt Numbers for Mass Flow Rates Closest to Optimum Value

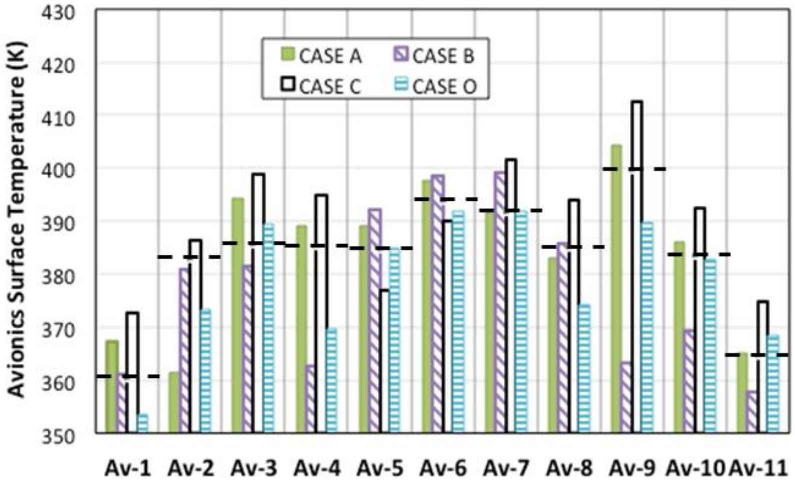

Figure 6.10. Avionics Average Surface Temperatures With Mass Flow Rates Closest to Optimum Value

It is observed that even for the optimum case, the temperature limits are slightly exceeded (by 2K on average) for some of the equipment. This is because the optimization is performed with the prediction function, and the CFD for the corresponding parameters gives slightly different results as was earlier shown with the comparisons given in Table 6.1. Overall, Case O (optimum) provides the best cooling for all equipment in the avionics bay.

6.5. Effect of Turbulence Model

The effect of the turbulence model selection on the CFD results is evaluated in this section. The analysis results obtained with four different turbulence models are used for comparison. Variation of the power consumption, the turbulence intensity, the non-dimensionalized velocity and temperature fields, and the avionics surface Nusselt numbers are investigated. In addition, extra attention is paid to the fan jet to assess the effect of the turbulence model.

6.5.1. Power Consumption

The power consumed by the fan is calculated by (63). The selected turbulence model has an effect on the pressure rise parameter in (63). Other parameters are the same for all four solutions. The pressure rise magnitudes obtained with four different turbulence models are given in Table 6.2.

Table 6.2. *Pressure Rise Magnitudes for Turbulence Models*

Turbulence Model	*Standard k-ε*	*RNG k-ε*	*Realizable RNG k-ε*	*SST k- ω*
Pressure Rise (Pa)	19.3	19.8	19.9	19.9

It is known that the power consumption is linearly proportional to the pressure rise. According to the selected turbulence model, up to 3% variation can be observed in power consumption.

6.5.2. Turbulence Intensity

In Figure 6.11, turbulence intensity (T.I.) contours obtained with four turbulence models are shown. The effect of the turbulence model is evaluated at three different cross sections. The first and second cross sections are normal to the fan and exhaust respectively. The third cross-section is parallel to the floor of the nose avionics bay with a 450 mm offset towards upper direction. The locations of the cross sections are also show in Figure 6.11 on top of the contours.

The results of all models show similar patterns. High turbulence intensity is observed at the boundary of the fan jet, under the rack and around the exhaust. Also, high velocity gradients are observed in the fan jet region and around the exhaust due to higher velocity magnitudes. As a result, higher turbulence intensity values are observed in these regions. The region under the rack is another location with high turbulence intensities. A branch of the fan jet gets under the rack after the initial impingement of the fan jet on the avionics. This branch causes a recirculating flow and high turbulence intensities in this region. Additionally, when the turbulence intensity contours at the third cross section is observed, it is seen that another branch of the fan jet flows towards the rear part of the bay after impingement. High turbulence intensity values could be observed along this branch as well. In terms of magnitudes, higher values are obtained for the Standard k-ε model compared to the other models, especially in the region around the exhaust. Apart from the exhaust, the Standard k-ε model and Realizable k-ε model yield closer turbulence intensity values, whereas smaller values are obtained with the other two models.

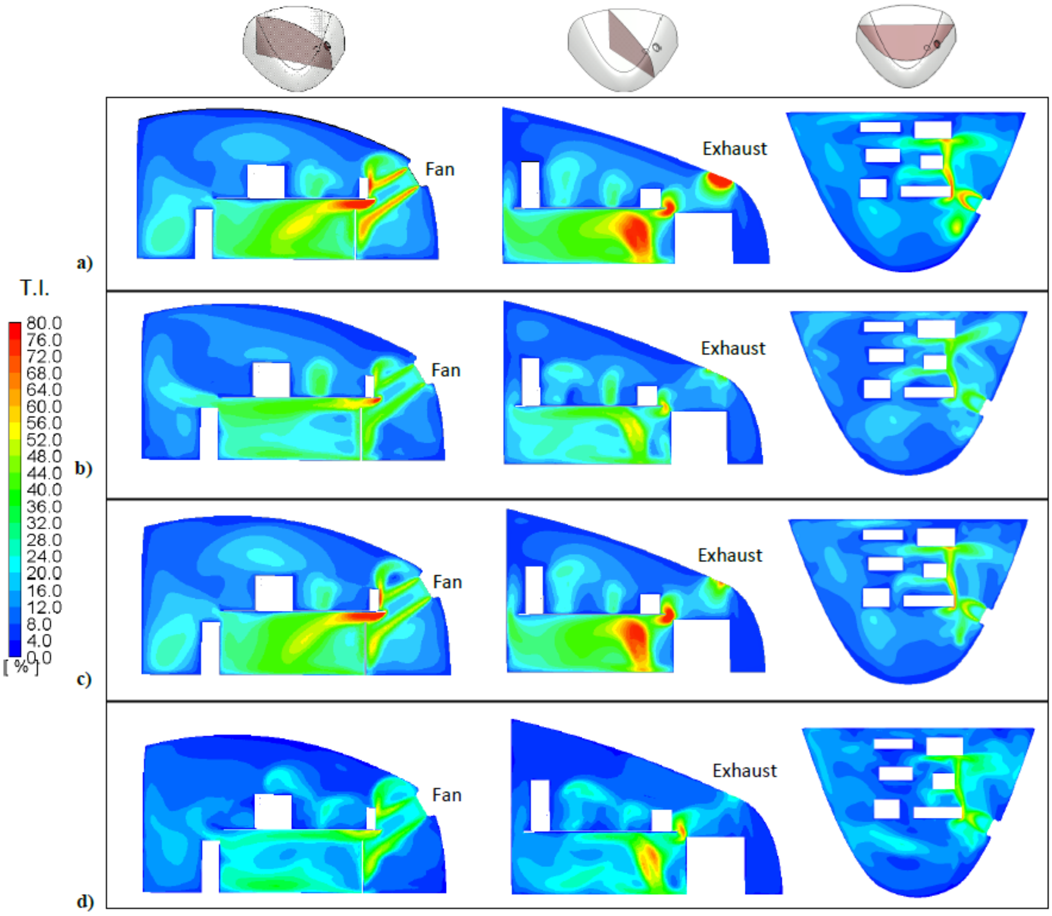

Figure 6.11. Turbulence Intensity Distributions With Turbulence Models a) Standard k-ε, b) RNG k-ε, c) Realizable k-ε, d) SST k-ω

6.5.3. Velocity Field

The velocity field is non-dimensionalized (V*) with the area-averaged velocity magnitude at the fan inlet, which is 5.16 m/s. The three cross sections mentioned above are also used to generate the non-dimensionalized velocity contours shown in Figure 6.12.

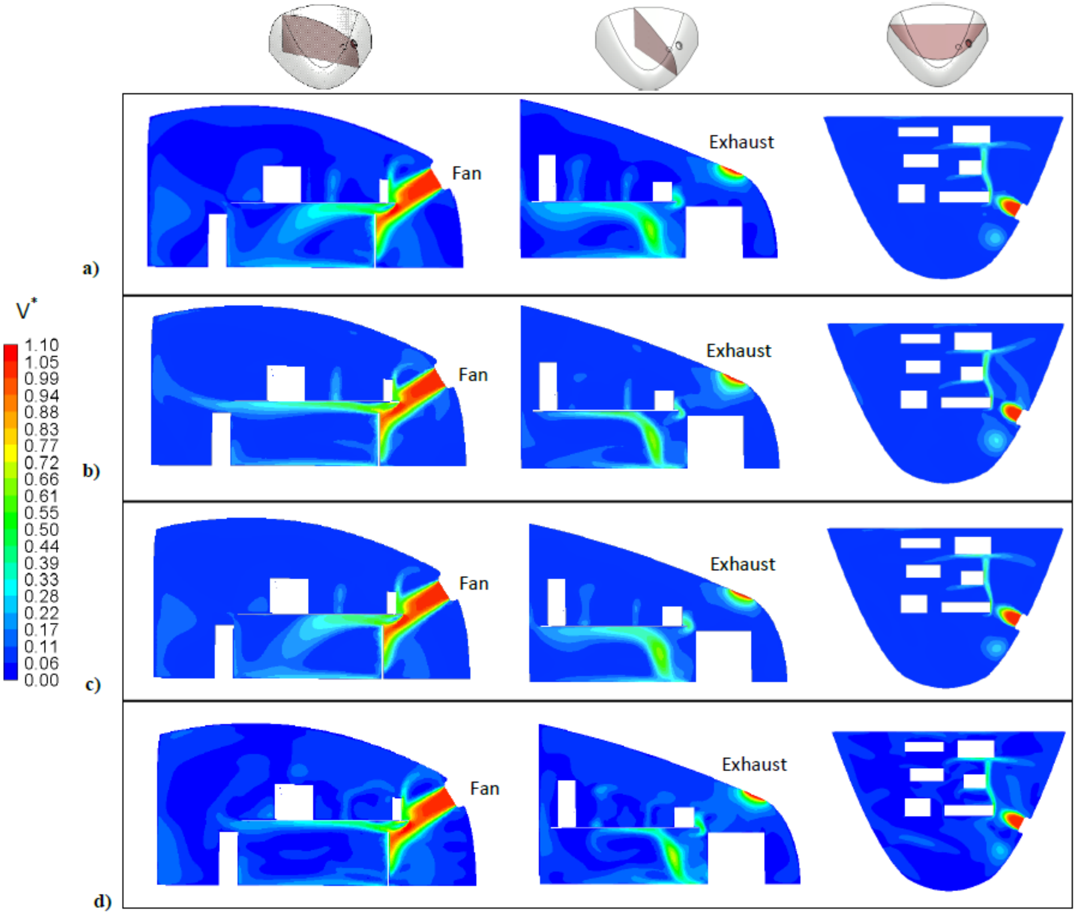

Figure 6.12. Non-dimensional Velocity Distributions With Turbulence Models a) Standard k-ε, b) RNG k-ε, c) Realizable k-ε, d) SST k-ω

It is observed that the contours are much similar to each other in terms of both patterns and magnitudes compared to the turbulent intensity. High velocity values are observed in the fan jet region and around the exhaust. Additionally, the separation of the fan jet into different branches is observed through the investigation of the contours that are normal to the fan and parallel to the floor. As mentioned above, a branch of the fan jet gets under the rack after the impingement. The flow pattern of this branch could also be observed in contours for the first cross section. The difference is that the branch diffuses faster for the results obtained by the Standard and Realizable k-ε turbulence models compared to the other two models.

6.5.4. Thermal Field

Next, the temperature distributions and heat transfer in the avionics bay are compared. The contours are given in terms of non-dimensional temperatures, θ, where the local values are normalized with the air temperature at the fan inlet, which is 323.15 K. The contours are shown in Figure 6.13. Similar to the results above, the contours of the Standard and Realizable k-ε turbulence models resemble each other.

A hot zone is observed between the two avionics located on the rack in the contours for the second cross section. This zone occurs due to the effect of another avionics located on the rack, as is observable in the contours for the first cross section. The temperature values around this equipment are higher for the RNG k-ε turbulence model and especially for the SST k-ω turbulence model. It is also observed that the temperature values at the front section of the nose avionics bay is higher for the RNG k-ε and SST k-ω turbulence models. Similarly, the SST k-ω turbulence model yields the highest temperature magnitudes around this region. On the other hand, the region under the rack is predicted to be cooler by the RNG k-ε and SST k-ω turbulence models. It could be concluded that these two models yield higher temperature values for the region above the rack, whereas the Standard and Realizable k-ε turbulence models yield higher temperature values below the rack. This is most likely due to the differences observed in Figure 6.12 as the branch of the fan jet gets under the rack after impingement.

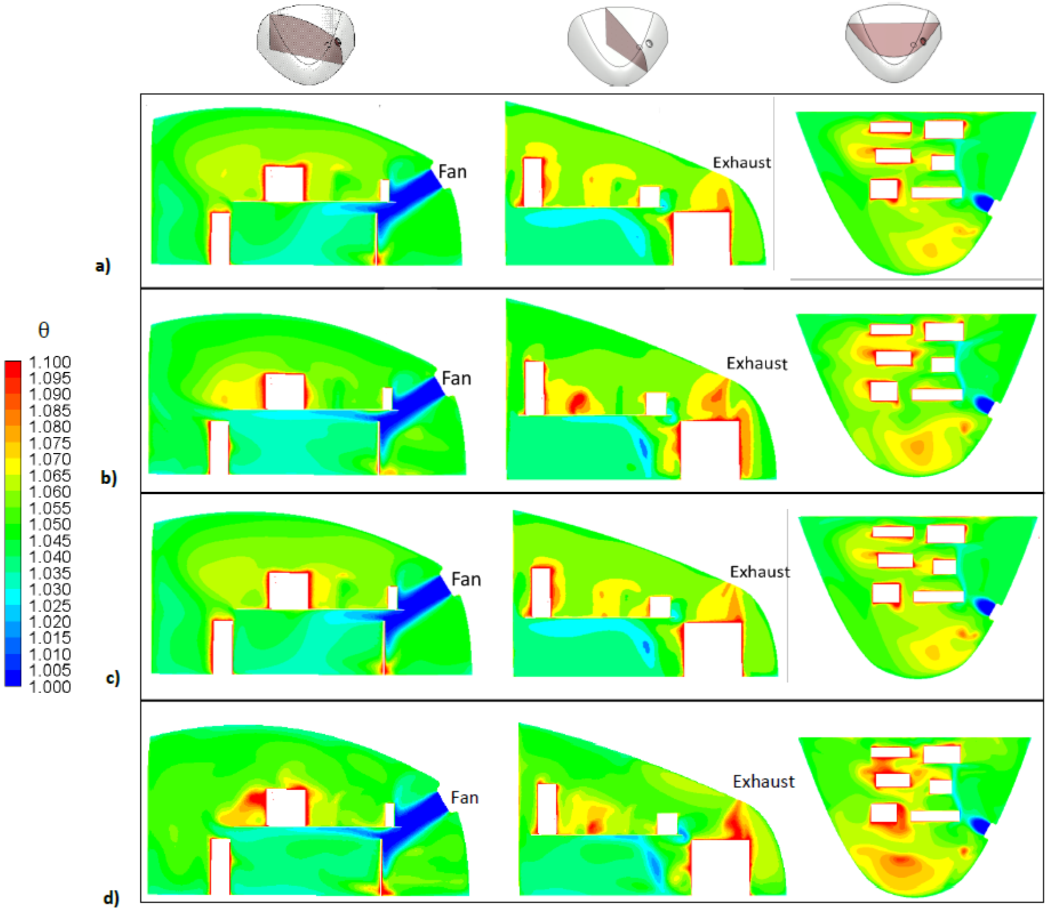

Figure 6.13. Non-Dimensional Temperature Distributions With Turbulence Models a) Standard k-ε, b) RNG k-ε, c) Realizable k-ε, d) SST k-ω

In addition to the temperature field inside the bay, the effect of the turbulence model on the average avionics surface temperatures is investigated. In Figure 6.14, the average avionics surface temperatures are shown for four turbulence models. Results for the Standard and Realizable k-ε turbulence models are very close to each other. The RNG k-ε turbulence model yields lower average surface temperatures for most of the equipment. The temperature value is lower by up to an amount of 3.2 K. Although the oscillations were observed in the time history of its predictions, still the overall trend for the SST k-ω turbulence model is that the average surface temperature values are generally predicted lower compared to the other models. As a result, the Standard or Realizable k-ε Turbulence models produces slightly more conservative results.

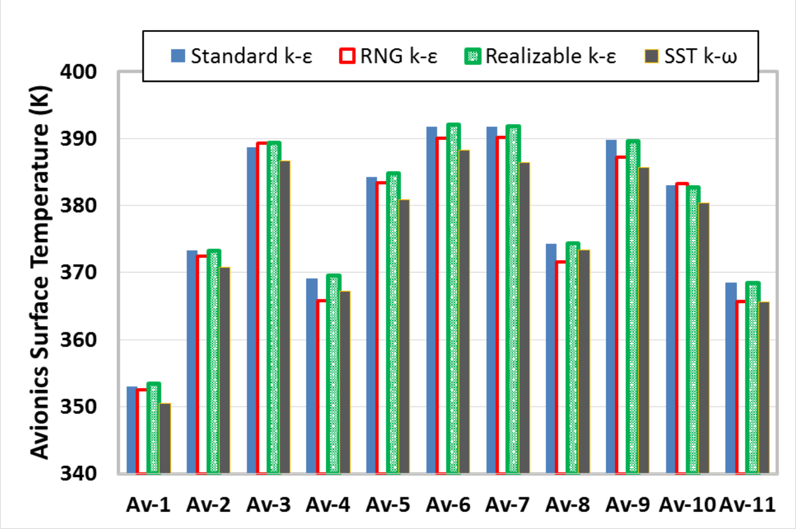

Figure 6.14. Avionics Equipment Average Surface Temperatures for All Turbulence Models

The local Nusselt number contours on the avionics surfaces are shown in Figure 6.15. The local Nusselt number is calculated by equation Eq.(65).

$$Nu = \frac{d_{fan}\, q_{convection}}{(T - T_{fan})k_{air}} \tag{65}$$

Here, $q_{convection}$ is the convective heat flux, $d_{fan}$is the diameter of the fan, T is the local temperature calculated by CFD, T_{fan} is air temperature at the fan inlet, and k_{air} is the thermal conductivity of air.

Higher Nusselt numbers are observed at locations where the fan jet impinges. There are not significant differences between the results.

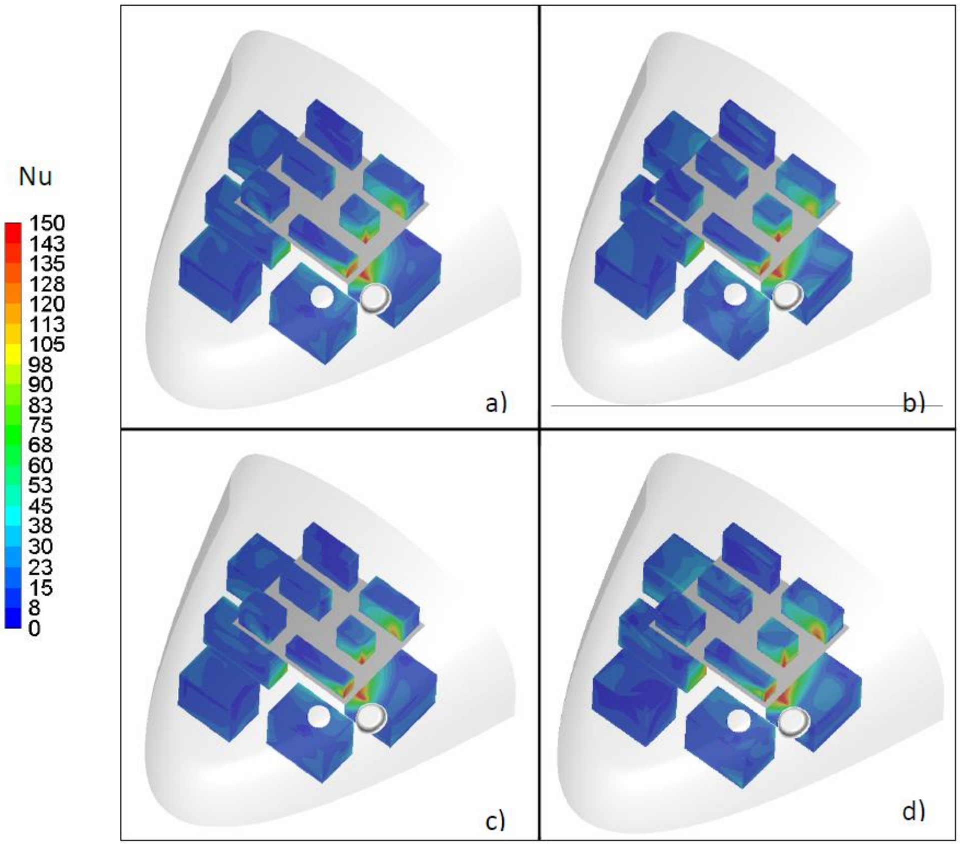

Figure 6.15. Nusselt Number Distributions With Turbulence Models a) Standard k-ε, b) RNG k-ε, c) Realizable k-ε, d) SST k-ω

The average Nusselt numbers along the surfaces of the avionic are also compared. The average Nusselt number is calculated by Eq.(66).

$$Nu = \frac{d_{fan}\, Q_{convection}}{\left(T_{avionics} - T_{fan}\right) k_{air}} \tag{66}$$

where, $Q_{convection}$ is the convective heat transfer from the surface of the avionics, and $T_{avionics}$ is the avionics average surface temperature calculated by CFD.

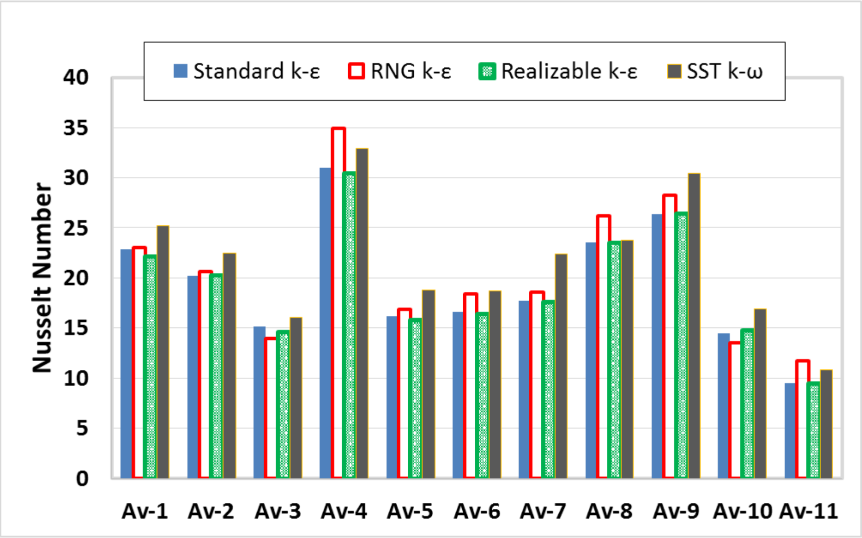

Figure 6.16. Avionics Equipment Average Nusselt Numbers for All Turbulence Models

As expected, the Standard and Realizable k-ε turbulence models results are similar. The average Nusselt numbers for the RNG k-ε turbulence model are higher. This behavior is also observed in Figure 6.14. The biggest differences in the Nusselt number are observed for Avionics 4, 6, 8 and 9 with the RNG k-ε turbulence model. These equipment are all located around the fan impingement region. Although the predictions for these avionics with the SST k-ω turbulence model resemble those of the RNG k-ε turbulence model, even higher heat transfer is predicted for Avionics 1, 2, 7 and 10 with the SST k-ω turbulence model.

6.5.5. Fan Jet Flow Dynamics

In this section, an extra attention is paid to the fan jet region. A representative shape of the fan jet is created for each turbulence model by generating streamlines that originate from ten different points located at the edge of the fan inlet surface. The jet shape obtained with the Realizable k-ε turbulence model is shown as an example in red color in Figure 6.17. The turbulence intensity, non-dimensional velocity and temperature contours are obtained at different cross sections along the jet in the following figures.

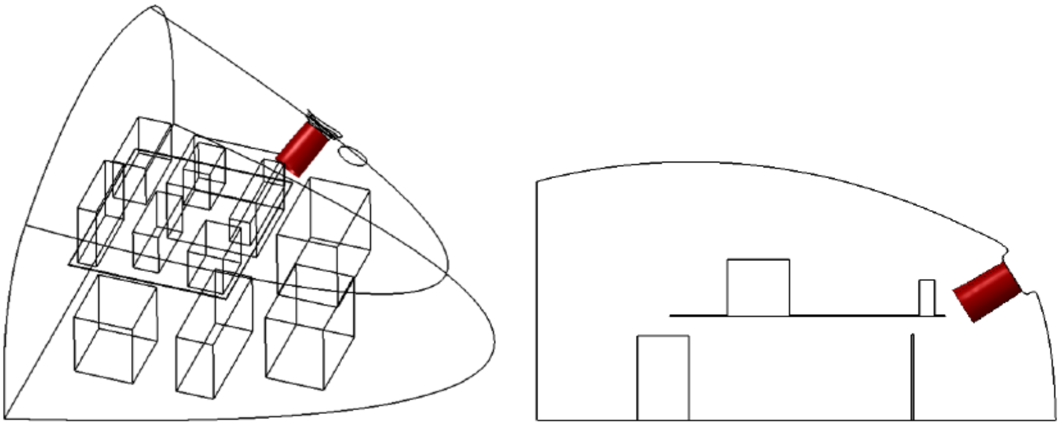

Figure 6.17. Fan Jet Domain Under Investigation

The turbulence intensity contours are given in Figure 6.18. Contours are generated at three locations along the jet. Turbulence intensity is found to be lower at the center of the jet. Although the velocity magnitudes are higher at the center, the gradients are smaller compared to the outer region of the jet. This is due to fact that the high-momentum air at the outer section of the jet encounters with the low-momentum air inside the bay. This causes higher velocity gradients and higher temperature intensity at this section. The turbulence intensity values do not change significantly along the jet. However, the low turbulence intensity zone at the center of the jet gradually shrinks as the effect of viscous forces on the jet increases in the flow direction. In terms of magnitudes, higher turbulence intensity values are obtained with the Standard k-ε turbulence model compared to the other turbulence models.

The non-dimensional velocity contours and non-dimensional temperature contours are shown in Figure 6.19 and Figure 6.20. The velocity magnitudes are similar for all solutions. The velocity magnitudes decreases in the flow direction due to the effect of the viscous forces. On the other hand, the temperature does not change significantly in the flow direction until the impingement.

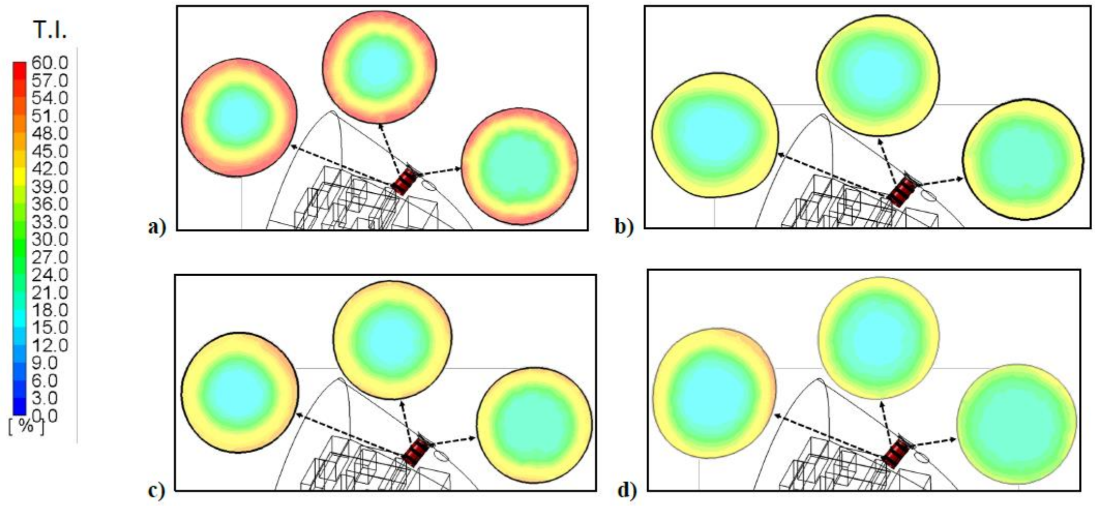

Figure 6.18. Turbulence Intensity Contours a) Standard k-ε, b) RNG k-ε, c) Realizable k-ε, d) SST k-ω

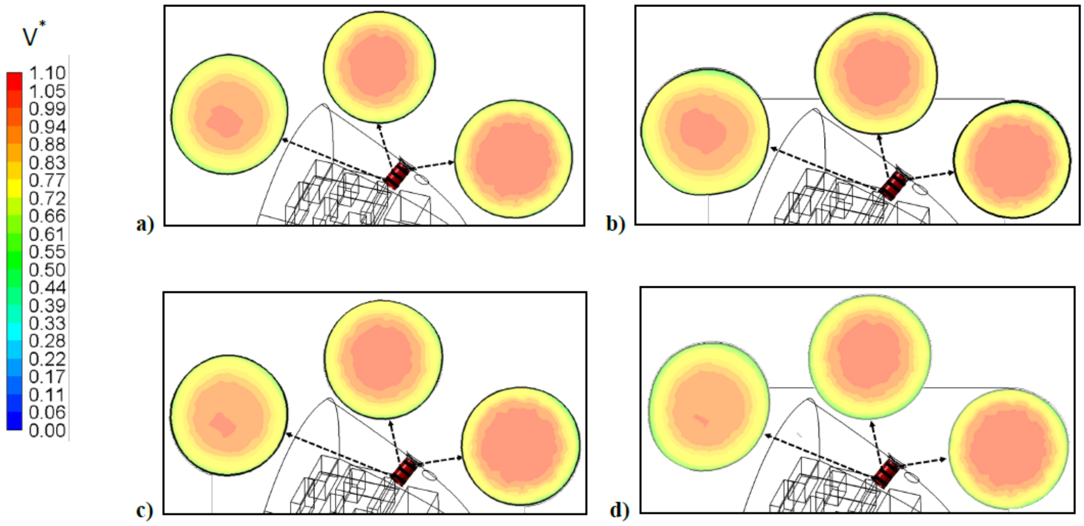

Figure 6.19. Non-dimensional Velocity Contours a) Standard k-ε, b) RNG k-ε, c) Realizable k-ε, d) SST k-ω

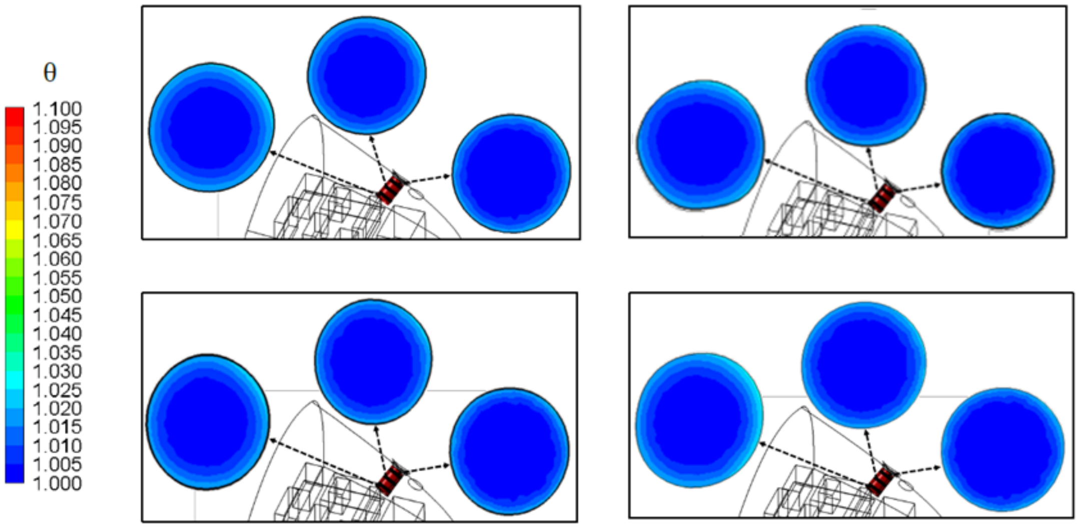

Figure 6.20. Non-dimensional Temperature Contours a) Standard k-ε, b) RNG k-ε, c) Realizable k-ε, d) SST k-ω

In addition, the turbulence intensity, velocity and temperature values are averaged along the jet flow direction and the plots shown in Figure 6.21 are created. The location along the jet is non-dimensionalized by the fan inlet diameter. It is observed that the averaged velocity and temperature values do not change significantly among the four turbulence models. On the other hand, clear differences exist in the turbulence intensity levels. Similar to Figure 6.18, the Standard k-ε turbulence model yields the highest intensity values.

As stated previously, the results of the SST k-ω turbulence model were oscillatory. The average velocity and temperature values predicted by the SST k-ω turbulence model are similar to those predicted by the other turbulence models. However, it yields the smallest turbulence intensity values for the first half of the jet, while for the second half, the RNG k-ε and the SST k-ω turbulence intensity values become similar. In order to investigate the effect of oscillations, the results from two randomly selected iterations are compared. It is observed that a maximum temperature difference of 0.25 K and a maximum velocity difference of 0.05 m/s occur along the jet. For these two iterations, the difference in the average avionics surface temperature values was found as approximately 0.6 K on average.

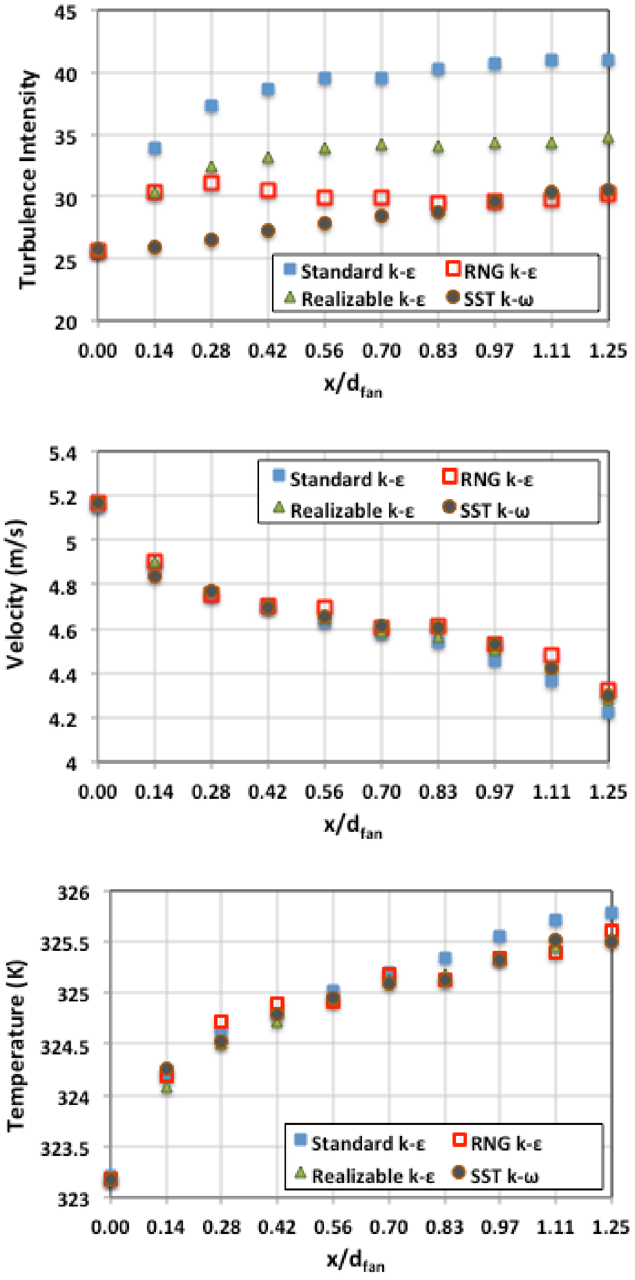

Figure 6.21. Variation in Flow Features Along Fan Jet

In addition, the change in the turbulence intensity, velocity and temperature in the radial direction is investigated inside the jet at a plane located at 1.25 x/dfan. The plots are shown in Figure 6.22 and the orientation of the radial direction is shown in Figure 6.23.

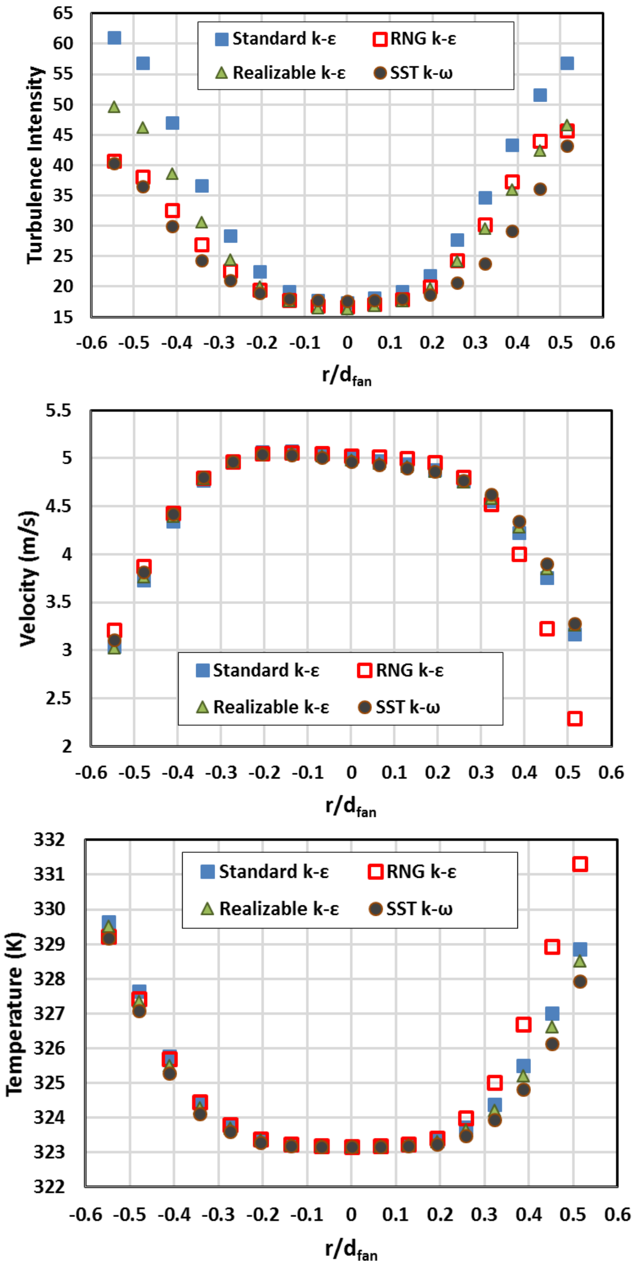

Figure 6.22. Variation in Flow Features Along Radial Direction Inside Jet

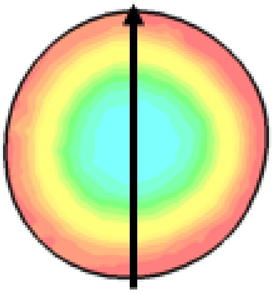

Figure 6.23. Orientation of Radial Direction

The standard k-ε turbulence model yields higher turbulence intensity values compared to the other models. The differences increase as the radial distance increases. On the other hand, the RNG k-ε turbulence model yields more distinct results compared to the other turbulence models, especially at the positive r/dfan values, when the velocity and temperature plots are investigated. The velocity magnitudes obtained by the RNG k-ε turbulence model decreases more rapidly as the radial distance increases, whereas the air temperatures predicted by the RNG k-ε turbulence model increase more rapidly with the radial distance.

CHAPTER 7

CONCLUSION

In this study, an avionics bay cooling system that consists of a fan and an exhaust is investigated. The system is installed at the nose avionics bay of a rotorcraft. The dimensions of the bay are determined based on a research on the commercial rotorcraft designs. In the scope of this study, the fan and exhaust are limited to be located on the skin of the bay. A series of CFD analyses are performed and the results of these analyses are used to build a prediction function to determine the average avionics surface temperatures. In order to determine the input parameters of these CFD analyses, a design-of-experiment study is performed. The Gaussian Process Regression and Artificial Neural Network methods are used to build two alternative prediction functions. It is found out that one hundred and seventy seven design points are required to obtain a prediction function that is accurate enough. Three additional CFD analyses are used to determine the prediction function that yields more accurate results. It is found out that the Gaussian Process Regression yields an average absolute error of 2.6 K, while the Artificial Neural Network yields an average absolute error of 3.8 K. Therefore, the Gaussian Process Regression is selected for use in the optimization study. In order to investigate how the accuracy of the prediction functions changes with the number of the design points, the average absolute errors are plotted as a function of the number of design points. It is observed that the accuracy of both the Gaussian Process Regression and Artificial Neural Network could be improved further by the addition of design points. On the other hand, a commonly used polynomial regression is also investigated and it is found out that the accuracy of this polynomial regression saturates at a lower number of design points. Therefore, both Gaussian Process Regression and Artificial Neural Network are found to be superior over the conventional polynomial regression in terms of accuracy.

The Gaussian Process Regression is used in conjunction with the Genetic Algorithm to determine the fan and exhaust locations that minimize the required mass flow rate. The minimum required mass flow rate is obtained when the fan is placed such that the fan jet impinges on the edges of avionics 1 such that the jet is divided into different branches. On the other hand, it is observed that the optimum exhaust location is close to the optimum fan location. However, the exhaust is located such that the air supplied by the fan does not directly flow towards the exhaust after impingement without effectively cooling the avionics. As a result of the optimization study, it is found out that the required mass flow rate could be reduced to approximately half of the value required by the fan and exhaust placement that was used to determine the upper limit of mass flow rate range. In addition, the reduction in the power consumption is calculated to be approximately ten times. A kind of a sensitivity analysis is performed to determine how strongly the required mass flow rate depends on the fan and exhaust locations separately. It is found out that the fan placement has a significant effect on the required mass flow rate, whereas the exhaust location has a limited effect. Based on the investigation of the CFD results, an air jet is observed to stand out at the fan exit that is oriented in a normal direction to the fan. As the fan location changes, the impingement characteristics of this jet on the avionics and the walls of the bay change. However, a similar jet-like flow structure oriented in a particular direction does not occur at the inlet of the exhaust. Instead, the exhaust draws air from all directions around. Due to this difference in the flow structures at the fan exit and exhaust inlet, the required mass flow rate depends strongly on the fan location and weakly on the exhaust location.

Additional CFD analyses for the optimum fan and exhaust locations are carried out with different turbulence models to evaluate the effect of the selected model. Results obtained with the Standard k-ε turbulence model, RNG k-ε turbulence model, Realizable k-ε turbulence model and SST k-ω turbulence model are compared. It should be noted that oscillatory results are obtained with the SST k-ω turbulence model and the residuals do not decrease to the desired levels. It is observed that the results of the Standard k-ε turbulence model and Realizable k-ε turbulence model are similar to each other in general. The most significant differences between the results are observed in the turbulence intensity values. It is seen that the selection of the Standard k-ε turbulence model results in higher turbulence intensity values, especially in the outer region of the fan jet. In contrast, the velocity and temperature fields inside the bay are similar. It is observed that the selected turbulence model has an effect on the branch of the jet that flows towards under the rack. This branch diffuses faster as predicted by the Standard k-ε and Realizable k-ε turbulence models. It can be inferred that this also causes higher air temperature values to be observed in the region under the rack with these two models. On the other hand, higher temperature values are observed in the region above the rack with the RNG k-ε and SST k-ω turbulence models. This might be because a larger portion of the fan jet is predicted to flow towards under the rack by the RNG k-ε and SST k-ω turbulence models compared to the other turbulence models. When the effect of turbulence models on the average avionics surface is investigated, the Standard k-ε turbulence model and Realizable k-ε turbulence model are found to yield higher average surface temperature values for most of the equipment, whereas the RNG k-ε turbulence model yields lower values among the four turbulence models.

REFERENCES

[1] "SAE International, Electrical and electronic equipment cooling in commercial transports", *SAE Aerospace Information Report*, vol. 64, Revision B, 1956, revised 1992.

[2] J. A. Rosero, J. A. Ortega, E. Aldabas and L. Romeral, "Moving towards a more electrical aircraft", *IEEE A&E Systems Magazine*, pp. 3-9, 2007.

[3] C. Butler and D. Newport, "Experimental and numerical analysis of thermally dissipating equipment in an aircraft confined compartment", *Applied Thermal Engineering*, vol.73, pp. 869-878, 2014.

[4] C. Butler, D. Newport and M. Geron, "Optimising the locations of thermally sensitive equipment in an aircraft crown compartment", *Aerospace Science and Technology*, vol. 28, pp. 391-400, 2013.

[5] J. Stafford, R. Grimes and D. Newport, "A compact modeling approach to enhance collaborative design of thermal-fluid systems", *Journal of Electronic Packaging*, vol. 136, 2014.

[6] E. H. Baalbergen, W. F. Lammen, A. J. de Wit, R. Maas, S. M. Moghadasi, J. Kos and F. Chiacchio, "Collaborative engineering technologies enabling multi-partner thermal analysis in early design stages of aircraft", *VII European Congress on Computational Methods in Applied Sciences and Engineering*, 2016.

[7] B. Jackson and J. Norgard, "A stochastic optimization tool for determining spacecraft avionics box placement", *Aerospace Conference Proceedings, IEEE*, Vol. 5, 2002.

[8] D. W. Hengeveld, J. E. Braun, E. A. Groll and A. D. Williams, "Optimal placement of electronic components to minimize heat flux nonuniformities", *Journal of Spacecraft And Rockets*, vol. 48, pp. 556-563, 2011.

[9] D. Dancer and M. Pecht, "Component-placement optimization for convectively cooled electronics", *IEEE Transactions on Reliability*, vol. 38, pp. 199-205, 1989.

[10] R. Grimes, M. Davies, J. Punch, T. Dalton and R. Cole, "Modeling electronic cooling axial fan flows", *Journal of Electronic Packaging*, vol. 123, no. 2, pp. 112-119, 2000.

[11] R. Grimes and M. Davies, "Air flow and heat transfer in fan cooled electronic systems", *Journal of Electronic Packaging*, vol. 126, no. 1, pp. 124-134, 2004.

[12] B. Muralidharan, F. A. I. Mariam, S. Karajgikar, D. Agonafer and M. Hendrix, "Energy minimization based fan configuration for double walled telecommunication cabinet with solar load", *26th IEEE SEMI-THERM Symposium*, 2010.

[13] R. Romadhon, M. Ali, A. M. Mahdzir and Y. A. Abakr, "Optimization of cooling systems in data centre by computational fluid dynamics model and simulation", *Innovative Technologies in Intelligent Systems and Industrial Applications*, *IEEE*, pp. 322-327, 2009.

[14] T. Zhang and X. You, "A simulation-based inverse design of preset aircraft cabin environment", *Building and Environment*, vol. 82, pp. 20-26, 2014.

[15] Y. Zhang, J. Liu, J. Pei, J. Li and C. Wang, "Performance evaluation of different air distribution systems in an aircraft cabin mockup", *Aerospace Science and Technology*, vol. 70, pp. 359-366, 2017.

[16] U. K. Mallela and A. Upadhyay, "Buckling load prediction of laminated composite stiffened panels subjected to in-plane shear using artificial neural networks," *Thin-Walled Structures,* Vol. 102, pp. 158-164, 2016.

[17] K. Ye, Y. Zhang, L. Yang, Y. Zhao, N. Li and C. Xie, "Modeling convective heat transfer of supercritical carbon dioxide using an artificial neural network," *Applied Thermal Engineering,* Vol. 150, pp. 686-695, 2019.

[18] A. Mitra, A. Majumdar, P. K. Majumdar and D. Bannerjee, "Predicting thermal resistance of cotton fabrics by artificial neural network model," *Experimental Thermal and Fluid Science,* Vol. 50, pp. 172-177, 2013.

[19] G. D. Nicola, M. Pierantozzi, G. Petrucci and R. Stryjek, "Equation for the thermal conductivity of liquids and an artificial neural network," *Journal of Thermophysics and Heat Transfer,* Vol. 30, pp. 651- 660, 2016.

[20] M. H. Esfe, M. R. H. Ahangar, D. Toghraie, M. H. Hajmohammad, H. Rostamian and H. Tourang, "Designing artificial neural network on thermal conductivity of Al2O3-Water-EG (60-40%) nano-fluid using experimental data," *Journal of Thermal Analysis and Calorimetry,* Vol. 126, pp. 837-843, 2016.

[21] "Bell525 Specification" [Online] Available: https://www.bellflight.com/commercial/bell-525 [Accessed 06 2017]

[22] "AS365 N3+ Description" [Online] Available: http://www.airbushelicopters.com/website/en/ref/AS365-N3+_34.html [Accessed 06 2017].

[23] "AS365 N3+ Specification" [Online] Available: http://airbushelicoptersinc.com/products/AS365-specifications.asp [Accessed 06 2017].

[24] "H155 Description" [Online] Available: http://www.airbushelicopters.com/website/en/ref/H155_35.html [Accessed 06 2017].

[25] "H155 Specification" [Online] Available: http://airbushelicoptersinc.com/products/H155-specifications.asp [Accessed 06 2017].

[26] "S76D Specification" [Online] Available: http://www.lockheedmartin.com/us/products/s-76-helicopter.html [Accessed 06 2017].

[27] "AW109 Power Specification" [Online] Available: http://www.leonardocompany.com/en/-/aw109-power-2 [Accessed 06 2017].

[28] "AW109 Operational Board Review Report", European Aviation Safety Agency [Online] Available: https://www.easa.europa.eu/system/files/dfu/A%20109E%20A109S%20AW%20109SP.pdf [Accessed 06 2017].

[29] "AW139 Specification" [Online] Available: http://www.leonardocompany.com/en/-/aw139 [Accessed 06 2017].

[30] "AW139 Operational Board Review Report", European Aviation Safety Agency [Online] Available: https://www.easa.europa.eu/system/files/dfu/AB%20139%20JOEB%20FINAL%20REPORT%20Rev%204-%2015_10_2012%20AWTAx.pdf [Accessed 06 2017].

[31] "Bell429WLG Specification" [Online] Available: http://www.bellhelicopter.com/commercial/bell-429wlg [Accessed 06 2017].

[32] "Grand New Specification" [Online] Available: http://www.leonardocompany.com/en/-/grandnew-1 [Accessed 06 2017].

[33] A. Jamnia, Practical guide to the packaging of electronics thermal and mechanical design and analysis, *Taylor & Francis Group*

[34] SAE International, SAE AIR 1168/3: Aerospace information report - aerothermodynamic systems engineering and design, 2011.

[35] MATLAB Model-based calibration toolbox guide, Release 2016a, Version 5.1, MA, *The MathWorks, Inc.*, 2016.

[36] D. C. Montgomery, Design and analysis of experiments, *John Wiley & Sons*, 2009.

[37] L. Kocis and W. J. Whiten, "Computational investigations of low-discrepancy sequences", *ACM Transactions on Mathematical Software*, vol. 23, pp. 266-294, 1997.

[38] Ansys Fluent 18.1 User's Guide, Ansys Inc, 2017.

[39] F. R. Menter, M. Kuntz, R. Langtry, "Ten years of industrial experience with the SST turbulence model," *In Proceedings of the 4th International Symposium on Turbulence, Heat and Mass Transfer*, Turkey, pp.625–632, 2003.

[40] D. Singh, B. Premachandran and S. Kohli, "Circular air jet impingement cooling of a circular cylinder with flow confinement", *International Journal of Heat and Mass Transfer*, vol. 91, pp. 969-989, 2015.

[41] F. P. Incropera, D. P. Dewitt, T. L. Bergman and A. S. Lavine, Fundamentals of heat and mass transfer, *John Wiley & Sons*, 2007.

[42] P. J. Roache, Verification and validation in computational science and engineering, *Hermosa Publishers,* 1998.

[43] P. J. Roache, "Quantification of uncertainty in computational fluid dynamics", *Annu. Rev. Fluid. Mech.*, vol. 29, pp. 123-160, 1997.

[44] S. Marsland, Machine learning: an algorithmic perspective, CRC Press, Taylor & Francis Group, 2015.

[45] MATLAB user guide, Release 2016a, Natick, MA: *The MathWorks Inc.*, 2016.

[46] D. Svozil, V. Kvasnicka, and J. Pospichal, "Introduction to multi-layer feed-forward neural networks," *Chemometrics and Intelligent Laboratory Systems*, vol. 39, pp. 43-62, 1997.

[47] D. J. C. Mackay, “A practical bayesian framework for backpropagation networks”, *Neural Computation*, vol. 4, pp. 448-472, 1992.

[48] A. T. Goh, “Some civil engineering applications of neural networks”, *Proceedings of the Institution of Civil Engineers - Structures and Buildings*, vol. 104, pp. 463–469, 1994.

APPENDICES

A. Halton Sequence Procedure

In order to explain the Halton Sequence procedure, an example is given below. For instance, it is desired to apply this procedure to the one hundred and twenty third design point (DP). Therefore, the index of the design point is 123. There are five parameters, namely the fan mass flow rate, fan x coordinate, fan y coordinate, exhaust x coordinate and exhaust y coordinate. As a result, the index number has to be expanded in five different prime bases. The expansion bases are shown in Table A.1.

Table A.1. *Expansion Basis for Parameters*

Parameter	*Fan Mass Flow Rate*	*Fan x Coord.*	*Fan y Coord.*	*Exhaust x Coord.*	*Exhaust y Coord.*
Expansion Basis	2	3	5	7	11

Then the index number is expanded at these bases to obtain the expansion coefficients. The expansion process for the Exhaust x Coordinate parameter is given in detail as: $123 = 4\ 7^0 + 3\ 7^1 + 2\ 7^2$ As it is seen, the expansion coefficients are 4, 3 and 2.

The expansion coefficients for all parameters are shown in Table A.2.

Table A.2. *Expansion Coefficients*

Parameter	*Fan Mass Flow Rate*	*Fan x Coord.*	*Fan y Coord.*	*Exhaust x Coord.*	*Exhaust y Coord.*
Expansion Coefficients	$a_0 = 1$ $a_1 = 1$ $a_2 = 0$ $a_3 = 1$ $a_4 = 1$ $a_5 = 1$ $a_6 = 1$	$a_0 = 0$ $a_1 = 2$ $a_2 = 1$ $a_3 = 1$ $a_4 = 1$	$a_0 = 3$ $a_1 = 4$ $a_2 = 4$	$a_0 = 4$ $a_1 = 3$ $a_2 = 2$	$a_0 = 2$ $a_1 = 0$ $a_2 = 1$

Then, the radical inverse function is applied to these expansions. This process for the Exhaust x Coordinate parameter is given in detail as: $4\,7^{-1} + 3\,7^{-2} + 2\,7^{-3} = 0.6385.$

The radical inverse function values are shown for all parameters in Table A.3.

Table A.3. *Radical Inverse Function Values*

Parameter	*Fan Mass Flow Rate*	*Fan x Coord.*	*Fan y Coord.*	*Exhaust x Coord.*	*Exhaust y Coord.*
Radical Inverse Function Values	0.8672	0.2757	0.7920	0.6385	0.1826

Then these numbers are scaled so that the actual numerical values of the five parameters are obtained.

B. Design Points

The design points used in the computational analyses are provided in Table B.1.

Table B.1. *Design Points*

Design Point Index	*Fan Mass Flow Rate (kg/s)*	*Fan x Coord. (mm)*	*Fan y Coord. (mm)*	*Exhaust x Coord. (mm)*	*Exhaust y Coord. (mm)*
1	0.0395	440.6	273.2	196.9	145.1
2	0.0318	859.4	478.3	378.2	240.3
3	0.0279	580.2	888.6	740.6	430.6
4	0.0434	999.1	109.1	921.9	525.7
5	0.0337	487.1	150.1	585.3	1001.4
6	0.0492	906.0	355.3	766.5	58.6
7	0.0298	207.9	560.4	947.8	153.8
8	0.0453	626.7	765.5	1129.0	248.9
9	0.0531	347.5	191.2	248.7	439.2
10	0.025	766.4	396.3	429.9	534.3
11	0.0482	533.7	1011.6	973.6	819.7
12	0.0366	673.3	642.4	274.6	67.3
13	0.0424	812.9	76.3	818.3	352.7
14	0.0463	875.0	896.8	300.5	733.3
15	0.0385	176.8	117.3	481.7	828.4
16	0.054	595.7	322.4	663.0	923.5
17	0.04	316.5	732.7	1025.4	75.9
18	0.0322	735.3	937.8	1206.7	171.1
19	0.0477	1154.2	158.4	145.2	266.2
20	0.0439	502.6	568.6	507.6	456.5
21	0.0361	921.5	773.7	688.9	551.6
22	0.0458	130.3	240.4	714.7	179.7
23	0.038	549.2	445.5	896.0	274.9
24	0.0535	968.0	650.6	1077.2	370.0
25	0.0487	409.5	289.6	381.9	750.6
26	0.0293	828.4	494.7	563.1	845.7

27	0.0526	471.6	125.5	1106.8	93.2
28	0.0429	192.4	535.8	226.5	283.5
29	0.0351	611.2	740.9	407.8	378.7
30	0.0313	332.0	166.6	770.2	568.9
31	0.0468	750.9	371.7	951.5	664.1
32	0.032	238.9	412.7	614.9	101.9
33	0.0475	657.8	617.8	796.1	197.0
34	0.0417	564.7	864.0	640.8	767.9
35	0.0456	1123.2	503.0	123.0	110.5
36	0.0378	425.1	708.1	304.2	205.7
37	0.0533	843.9	913.2	485.4	300.8
38	0.033	445.7	544.0	1029.1	586.2
39	0.0368	1004.2	379.9	511.3	966.8
40	0.0523	306.1	585.0	692.5	1061.9
41	0.0271	725.0	790.1	873.8	119.2
42	0.0504	492.3	420.9	174.7	404.6
43	0.031	911.2	626.0	356.0	499.7
44	0.0388	631.9	1036.3	718.4	690.0
45	0.0543	1050.8	256.8	899.7	785.2
46	0.0286	538.8	100.9	385.6	223.0
47	0.0441	957.7	306.0	566.8	318.1
48	0.0364	259.6	511.2	748.0	413.3
49	0.0519	678.5	716.3	929.3	508.4
50	0.0383	880.1	183.0	955.2	136.5
51	0.0538	182.0	388.1	1136.4	231.6
52	0.0489	740.5	224.0	618.6	612.2
53	0.0431	647.4	470.1	463.2	50.8
54	0.0509	368.2	880.4	825.7	241.1
55	0.0548	554.3	480.0	307.9	621.6
56	0.0241	973.2	685.1	489.1	716.7
57	0.0319	694.0	110.8	851.6	907.0
58	0.028	414.7	521.0	1214.1	59.4
59	0.0435	833.6	726.1	152.5	154.6
60	0.0512	57.9	151.8	515.0	344.8
61	0.0261	476.8	356.9	696.2	440.0
62	0.0416	895.6	562.0	877.5	535.1
63	0.0377	756.0	603.0	540.9	1010.8
64	0.0406	523.3	233.8	1084.6	258.4

65	0.029	662.9	849.2	208.0	543.8
66	0.0367	383.7	77.9	570.5	734.0
67	0.0522	802.6	283.1	751.7	829.2
68	0.0348	569.9	898.4	52.7	76.7
69	0.0503	988.7	119.0	233.9	171.9
70	0.0309	290.6	324.1	415.2	267.0
71	0.0464	709.5	529.2	596.4	362.1
72	0.0542	430.2	939.4	958.8	552.4
73	0.0479	450.9	775.3	441.0	933.0
74	0.044	171.7	201.0	803.5	85.4
75	0.0362	590.5	406.1	984.7	180.5
76	0.0517	1009.4	611.3	1166.0	275.7
77	0.042	730.2	1021.5	285.7	465.9
78	0.0343	1149.0	242.0	466.9	561.1
79	0.0304	497.5	652.3	829.4	751.3
80	0.0256	1056.0	291.3	311.6	94.0
81	0.0411	357.8	496.4	492.8	189.2
82	0.0333	776.7	701.5	674.1	284.3
83	0.0294	125.1	127.2	1036.5	474.6
84	0.0275	683.6	947.6	518.7	855.1
85	0.043	1102.5	168.2	699.9	950.3
86	0.0508	823.3	578.4	1062.4	102.7
87	0.0391	466.4	209.2	363.4	388.1
88	0.0546	885.3	414.3	544.6	483.2
89	0.0399	606.1	824.6	907.1	673.5
90	0.0263	931.8	94.4	755.4	301.6
91	0.0418	233.7	299.5	936.7	396.7
92	0.0341	652.6	504.6	1117.9	491.9
93	0.0457	792.2	135.4	418.9	777.3
94	0.0331	280.3	176.4	82.3	215.1
95	0.0486	699.1	381.5	263.5	310.3
96	0.0447	419.9	791.8	626.0	500.5
97	0.037	838.8	996.9	807.2	595.7
98	0.0311	621.6	258.4	651.9	128.6
99	0.0466	1040.4	463.6	833.1	223.8
100	0.0389	342.3	668.7	1014.3	318.9
101	0.0403	109.6	102.6	315.3	604.3
102	0.0326	528.5	307.7	496.5	699.5

103	0.0481	947.4	512.8	677.8	794.6
104	0.052	388.9	348.7	159.9	137.3
105	0.0268	807.7	553.8	341.2	232.4
106	0.05	575.0	184.6	884.9	517.8
107	0.0307	993.9	389.7	1066.1	613.0
108	0.0258	435.4	225.6	548.3	993.5
109	0.0374	163.0	471.8	215.4	432.1
110	0.0529	581.9	676.9	396.7	527.3
111	0.0355	721.5	71.4	940.4	812.7
112	0.0471	488.8	686.7	241.3	60.2
113	0.0394	907.7	891.9	422.5	155.4
114	0.0549	209.6	112.4	603.8	250.5
115	0.0241	628.5	317.5	785.0	345.6
116	0.0396	1047.3	522.6	966.2	440.8
117	0.0357	535.4	563.7	629.7	916.5
118	0.0512	954.3	768.8	810.9	1011.6
119	0.0415	675.0	194.5	1173.4	164.0
120	0.0337	1093.9	399.6	111.9	259.1
121	0.0492	395.8	604.7	293.1	354.3
122	0.0299	814.6	809.8	474.3	449.4
123	0.0531	457.8	440.6	1018.0	734.8
124	0.0483	1016.3	79.6	500.2	77.5
125	0.0289	318.2	284.7	681.5	172.7
126	0.0444	737.1	489.8	862.7	267.8
127	0.0425	923.2	325.7	344.9	648.3
128	0.0347	225.1	530.8	526.1	743.5
129	0.0502	644.0	736.0	707.3	838.6
130	0.0386	783.6	366.8	1251.0	86.2
131	0.04	550.9	982.1	552.0	371.6
132	0.0323	969.8	202.7	733.2	466.7
133	0.0478	271.6	407.8	914.5	561.9
134	0.0342	473.3	859.0	762.8	190.0
135	0.0304	194.1	87.8	1125.3	380.2
136	0.0381	1031.8	498.0	245.0	570.5
137	0.0536	333.7	703.1	426.2	665.6
138	0.0255	752.6	908.3	607.5	760.8
139	0.041	1171.5	128.8	788.7	855.9
140	0.0294	938.7	744.2	89.7	103.5

141	0.0371	659.5	169.8	452.1	293.7
142	0.0526	1078.4	375.0	633.4	388.9
143	0.0275	380.2	580.1	814.6	484.0
144	0.043	799.1	785.2	995.8	579.2
145	0.0468	985.3	621.1	478.0	959.7
146	0.0546	706.0	1031.3	840.5	112.1
147	0.0243	1124.9	251.9	1021.7	207.3
148	0.0321	845.7	662.1	141.5	397.5
149	0.0437	447.5	96.0	685.2	682.9
150	0.0359	866.3	301.1	866.4	778.1
151	0.034	307.8	137.0	348.6	120.8
152	0.0495	726.7	342.1	529.8	215.9
153	0.0379	494.0	957.5	1073.5	501.3
154	0.0408	633.6	588.3	374.5	786.7
155	0.0427	261.3	260.1	378.7	510.0
156	0.035	680.2	465.2	559.9	605.1
157	0.0311	400.9	875.4	922.4	795.4
158	0.0248	463.0	514.4	404.6	138.1
159	0.0403	881.9	719.6	585.8	233.2
160	0.048	602.6	145.2	948.3	423.5
161	0.0267	90.7	186.2	611.7	899.2
162	0.0422	509.5	391.4	792.9	994.3
163	0.0306	649.2	1006.7	93.9	147.5
164	0.0461	1068.0	227.3	275.1	242.6
165	0.0384	369.9	432.4	456.4	337.8
166	0.0539	788.8	637.5	637.6	432.9
167	0.0451	695.7	883.6	482.3	1003.7
168	0.0529	416.4	73.0	844.7	156.1
169	0.0277	835.3	278.1	1026.0	251.3
170	0.0509	478.5	893.5	326.9	536.7
171	0.0316	897.4	114.0	508.1	631.8
172	0.0471	199.2	319.2	689.4	727.0
173	0.0393	618.1	524.3	870.6	822.1
174	0.0397	757.7	155.1	171.6	69.7
175	0.0319	1176.6	360.2	352.8	164.8
176	0.0281	525.0	770.4	715.3	355.1
177	0.0358	245.8	196.1	1077.7	545.3

C. Fitness Evaluation Code

```
% Input x vector stores fan and exhaust locations and the Matlab
% function determines the minimum required mass flow rate as output.

function mdot = fitness(x)

% Define temperature limits for avionics

T1_lim=360.16;
T2_lim=382.69;
T3_lim=385.49;
T4_lim=385.27;
T5_lim=384.74;
T6_lim=393.57;
T7_lim=391.59;
T8_lim=384.96;
T9_lim=399.64;
T10_lim=383.38;
T11_lim=364.64;

% Define constraints

if x(1)<0
    mdot = 0.055;
elseif x(1)>1256.6;
    mdot = 0.055;
elseif x(2)<0
    mdot = 0.055;
elseif x(3)<0
    mdot = 0.055;
elseif x(3)>1268.6;
    mdot = 0.055;
elseif x(4)<0
    mdot = 0.055;
elseif x(2)> -0.00260442494238715*x(1)^2+3.27278468507145*x(1)-
3.09131581952488
    mdot = 0.055;
elseif x(4)> -0.00260781353514871*x(3)^2+3.30834813744603*x(3)-
2.81726332395419
    mdot = 0.055;

else

% Define initial guesses for mass flow rate lower and upper values

mdot_up=0.055;
mdot_low=0.024;

% Calculate the required mass flow rate for the corresponding fan
% and exhaust locations by bi-sectioning method and utilizing
% Gaussian Process Regression functions (GPRs)
```

```
for i=1:1000
    mdot=(mdot_up+mdot_low)/2;

    T_dif =[T1_lim- predict(GPR_T1,[mdot x(1) x(2) x(3) x(4)]);
            T2_lim- predict(GPR_T2,[mdot x(1) x(2) x(3) x(4)]);
            T3_lim- predict(GPR_T3,[mdot x(1) x(2) x(3) x(4)]);
            T4_lim- predict(GPR_T4,[mdot x(1) x(2) x(3) x(4)]);
            T5_lim- predict(GPR_T5,[mdot x(1) x(2) x(3) x(4)]);
            T6_lim- predict(GPR_T6,[mdot x(1) x(2) x(3) x(4)]);
            T7_lim- predict(GPR_T7,[mdot x(1) x(2) x(3) x(4)]);
            T8_lim- predict(GPR_T8,[mdot x(1) x(2) x(3) x(4)]);
            T9_lim- predict(GPR_T9,[mdot x(1) x(2) x(3) x(4)]);
            T10_lim-predict(GPR_T10,[mdot x(1) x(2) x(3) x(4)]);
            T11_lim-predict(GPR_T11,[mdot x(1) x(2) x(3) x(4)])];


    if abs(min(T_dif))<0.001 || (0.055-mdot_low) < 0.0001

        break

    elseif min(T_dif)>= 0.001

            mdot_up=mdot;

    elseif min(T_dif)<= -0.001

            mdot_low=mdot;

    end

end
end
```